2015-08-19

Passive and Active Microwave Remote Sensing and Modeling of Layered Snow

Fuller, Mark Christopher

UNIVERSITY OF CALGARY

Passive and Active Microwave Remote Sensing and Modeling of Layered Snow

by

Mark Christopher Fuller

A THESIS

SUBMITTED TO THE FACULTY OF GRADUATE STUDIES

IN PARTIAL FULFILMENT OF THE REQUIREMENTS FOR THE

DEGREE OF DOCTOR OF PHILOSOPHY

GRADUATE PROGRAM IN GEOGRAPHY

CALGARY, ALBERTA

AUGUST, 2015

Abstract

This thesis investigates the effects of complexly-layered snow on passive and active microwave remote sensing observations and models, employing detailed in-situ geophysical measurements over various landcover types. First, I present observed and simulated C-band backscatter signatures for complexly-layered snow on smooth, landfast first-year sea ice. Detailed in-situ measurements describe snow structure. A multilayer backscatter model is used to assess the impacts of layered components. The backscatter from a complexly-layered snow cover on smooth first-year sea ice is higher than from a simple snow cover. Sensitivity analysis suggests that rough ice layers within the snow cover and superimposed at the snow-ice interface influence brine volume, and are mechanisms that increase surface and volume scattering. This has implications for sea ice mapping, geophysical inversion, and snow thickness retrievals. Second, I present a snow layer excavation experiment to compare observed and modeled brightness temperatures at 19 and 37 GHz, with regard to snow water equivalent (SWE), snow type, grain size, and layered structure. In-situ snow measurements forced a multi-layer snow emission model. Emission scattering from depth hoar was disproportionate to its SWE contribution, and masked observed scattering contributions from upper snow layers. The simulations diverged from observations above 130 mm SWE, as simulations did not capture snowpack emission. This may impact the effective grain size optimization process of the GlobSnow assimilation technique. Third I present the application of meteorological reanalysis data to the SNTHERM snow model for comparison with in-situ snow measurements, and observed and simulated C-band backscatter of snow on first-year sea ice. Application of in-situ salinity profiles to one SNTHERM snow profile resulted in simulated backscatter close to in-situ measurements. In

other cases simulations remained 4 to 6 dB below observations. Although, there is the possibility of achieving comparable simulated backscatter from SNTHERM and in-situ snow geophysical samples, there are several constraints and considerations for improvement. These findings indicate that more complex representations of snow layering and microstructure are necessary for accurate retrievals of snow depth and snow water equivalents in state-of-the-art retrieval schemes.

Acknowledgements

This work was supported in part by the Natural Sciences and Engineering Research Council (NSERC), the Canada Foundation for Innovation (CFI) New Opportunities Fund for a grant to acquire the scatterometer and positioner systems, and by Alberta Innovation and Science for matching funds to CFI, and Environment Canada for provision of radiometer equipment and field logistics I thank all those in the University of Calgary Cryosphere Climate Research Group within the Department of Geography for their support.

Thank you to my supervisors Dr. John Yackel and Dr. Chris Derksen, whose guidance and patience have enabled me to conduct quality research in a top-class environment. I have learned much from the opportunities advice and guidance they have provided. I thank Dr. Torsten Geldsetzer for his unending patience, advice, and comradery.

I thank JPS Gill, Peter Bezeau, Melissa Peters, Randy Scharien, Adrienne Cunnings, Jean-Benoit Madora, Alex Beaudoin, John Rogerson, Jonathan Conway, and Chris Marsh. Alain Royer, Alex Langlois, Benoit Montpetit, and Alexandre Roy of Université de Sherbrooke. Kevin Kang, Grant Gunn, and Josh King of the University of Waterloo. Peter Toose and Arvids Silis of Environment Canada. LeeAnn Fishback, Carley Basler, Clifford Paddock and all of the staff of the CNSC and PSCP. Thank you to the Graduate Programs Administrator, Paulina Medori who has always been helpful and has worked tirelessly to keep me organized. The support and hard work of these and others have enabled this effort.

I thank my best friend Billy for getting me outside and keeping me active, and for his never-ending loyalty, happiness, and companionship. And lastly, I thank my partner in life Victoria Lukasik. Without her support and understanding this work would simply not have been possible.

Dedication

This work is dedicated to my Grandfather (Vladimir “Walter” Schewchuck), Father (Jeremy David Berrington Fuller), and Aunt (Edie Schewchuk), who passed during my academic pursuits, and couldn’t be with us to celebrate their part in making this possible.

I also dedicate this work to my Grandmother (Helen “Olena” Schewchuck) for her never-ending love, support, and enthusiasm for me and my studies.

Finally this work is dedicated to my Mother, Helen Fuller. This would not have been possible without her support, council, and love.

Table of Contents

List of Tables

List of Figures

List of Symbols, Abbreviations and Nomenclature

Symbol	Definition
α	Albedo
AOI	Area of interest
α_λ	Reflectivity
A_R	Receiver-antenna aperture
c	Speed of light
C_e	Bulk transfer coefficient for latent heat
c_p	Specific heat capacity
C_s	Bulk transfer coefficient for sensible heat
dB	Decibels
DMRT-QCA	Dense Media Radiative Transfer theory based on Quasicrystalline Approximation
D_{eff}	Effective grain size
δ_p	Penetration depth
d_0	Grain size
d_0	Snow thickness
D_{obs}	Observed grain size
D_{ref}	Snow depth
ε*	Complex dielectric constant, complex dielectric permittivity
ε'	Dielectric constant, dielectric permittivity
ε''	Dielectric loss
ε_0	Permittivity of free space
ε_a	Atmospheric emissivity
ε_S	Static dielectric constant
ε_s	Surface emissivity
ESA	European Space Agency
f	Frequency
FQ	Fine quad-polarized
$f_{rt}(\varepsilon^*, \theta)$	Dielectric constant dependence
$f_s(\rho(\xi), \theta)$	Surface autocorrelation, roughness
FYI	First-year ice
Υ	Transmission
Gt	Transmitter-receiver gain
h	Planck's constant
H, HH	Horizontal polarization, send receive
HUT	Helsinki University of Technology
IR	Infrared spectrum
K	Thermal conductivity
k	Stefan-Boltzman Constant
ka	Absorption
ke	Extinction
k_{eff}	Conductivity of snow
ks	Scattering

L	Attenuation length
l	Loss
λ	Wavelength
MEMLS	Microwave Emission Model for Layered Snow
MSIB	Multilayer snow and ice backscatter
n	Refraction
NARR	North American Regional Reanalysis
NCEP	Nation Centers for Environmental Prediction
η	Viscosity
p	Polarization
$P/P_0\cos(z)$	Atmospheric attenuation due to path length
Pr	Backscattered power received
ψ_λ	Transmissivity
Pt	Power transmitted
q_a	Specific humidity at surface
Q_E	Sensible heat flux
Q_G	Radiative conduction and transfer
Q_H	Latent heat flux
$Q_L^{\downarrow}$	Incoming longwave radiation
$Q_L^{\uparrow}$	Outgoing longwave radiation
q_o	Specific humidity at reference height
Q_P	Sensible heat advected by precipitation
Q_R	Sensible heat advected by runoff
$Q_S^{\downarrow}$	Incoming shortwave radiation
$Q_S^{\uparrow}$	Outgoing shortwave radiation
Q_{S0}	Top of atmosphere irradiance
r	Reflection
R(0)	Fresnel reflection coefficient
ρ	Density
ρ	Reflection
S	Salinity
SD	Snow depth
σ	Standard deviation of surface height
σ	Radar cross-section (RCS)
σ^0	Normalized Radar Cross Section (NCRS)
σ_{HH}^0	NCRS co-polarized
σ_{HV}^0	NCRS cross-polarized
σ_m	Surface roughness
σ_v	Volume scattering coefficient
σ_{VV}^0	NCRS co-polarized
SWE	Snow water equivalent
t	Transmission
T	Temperature
T_a	Air temperature
T_B	Brightness temperature
$T_B(v)$	Raleigh-Jeans equivalent brightness temperature

$\frac{\partial T}{\partial z}$	Temperature gradient
θ	Incidence angle
T_s	Surface temperature
u	Wind speed at reference height
ν	Frequency
V, VV	Vertical polarization, send receive
VIS	Visible spectrum
Wv	Water volume
ξ_λ	Absorbtivity
Z	Zenith angle

Chapter One: **Introduction**

1.1 Rationale

Within the context of a warming Arctic, an increase in melt and rain events through the winter is expected to create relatively more complexly-layered snow covers on both land and sea ice. The effect of this increased complexity on observed and simulated microwave emission and backscatter requires investigation, as snow has typically been represented as a relatively homogeneous media in models. The rationale for this work is to contribute new understanding of the role of a more complex representation of snow properties and processes in the Arctic and sub-Arctic over land and sea ice, to passive and active microwave remote sensing observations and microwave and thermodynamic snow modeling, for hydrologic and climate applications.

The cryosphere comprises all of the parts of the Earth in which water is found in a solid state. This includes sea, lake, and river ice; snow; permafrost; glaciers, ice caps, and ice sheets. The cryosphere is a vital component of the global climate system due to the amounts of energy involved in the heating and cooling (sensible heat) and the formation and ablation of ice (latent heat) (Serreze and Barry 2005). Snow plays an important role in radiative interactions with the Earth's surface due to its unique thermodynamic properties and high albedo (Robok 1983). In a review of literature by Arons and Colbeck (1995), snow cover is recognized by many studies as having a distinct and important role with regard to radiative and chemical transfer processes, to moderation of the thaw and freeze of soils, as an important freshwater input, and as a control of sea ice formation, ablation, extent, and thickness (Maykut 1982; Curry et al. 1995). As the most seasonally variable component of the cryosphere, the impacts of variations in climate on snow cover must be better understood (Marsh 1999).

Snow cover exhibits great spatio-temporal variability (Brown and Braaten 1998), and is dynamically coupled with global processes of hydrology and climate. Seasonal snow covers about 40 million square kilometers in the Northern Hemisphere (Chang et al. 1987a), and over 30% of land, with sea ice covering 7% of oceans (Parkinson and Washington 1979). Snow cover extent is both driven-by and drives climate through energy-albedo feedback processes (Budyko 1969; Robok 1983) and is a sensitive indicator of climate change (Chang et al. 1990); the effects of which will be expressed most strongly at higher latitudes (Holloway and Sou 2002). An increase in Arctic and Sub-Arctic temperature are expected to result in an intensification of the hydrologic cycle (Holland et al. 2007, Kohn et al. 2007; Rawlins et al. 2010) caused by a loss of sea ice resulting in increased evaporation from the Arctic Ocean to the atmosphere (Serreze and Francis 2006). The reduction of temperature gradients between the pole and equator affect pressure gradients, which transport energy via global atmospheric circulation phenomena (e.g. Arctic Oscillation, Aleutian Low, Jetstream, North Atlantic Oscillation). This has resulted in increased and extended meridonal circulation, causing higher amplitude but slower moving waves characterized as "blocking" (Francis and Vavrus 2012), resulting in a loss of sea ice (Overland 2010), and more extreme levels of drought, flood, and precipitative weather events (Berner et al. 2005; Rawlings et al. 2010). However, Barnes (2013) found that this may be a result of methodology used in (Francis and Vavrus 2012), and found no decrease in wave speeds over North America and the North Atlantic, with the exception of October through December, the period of snowpack and sea ice formation and accumulation. Further work by Barnes et al (2014) employing several blocking indices also found that any blocking was limited to isolated and specific regions or time periods, and was difficult to separate from internal and decadal variability. Therefore, this remains a source of some contention; however, the isolation of

blocking to specific areas and time periods likely adds further complexity to snow evolution over land and sea ice, and associated energy fluxes. These phenomena and their associated variability may result in increased heterogeneity in snow accumulation in polar and sub-polar regions, given an expected increase in the frequency and spatiotemporal complexity of rain on snow and melt events throughout the season (Holland et al. 2006, Kattsov et al. 2007, Trenberth et al. 2007).

Snow plays an important role in radiative interactions due to its albedo, thermal capacity, conductivity, and diffusivity (Robok 1983). Snow cover governs heat and energy across the Earth surface-atmosphere interface, and therefore formation, ablation, extent, and thickness of underlying surface such as permafrost (Park et al. 2015), glaciers and ice sheets (Shea et al. 2005; Box et al. 2012), and sea ice (Maykut 1982; Curry et al. 1995). The high seasonal and inter-annual variability of snow and sea ice extent and thickness (Parkinson and Washington 1979; Colbeck 1991) impacts biological, cultural, economic, and global climate systems; therefore, understanding the response of snow and sea ice to atmospheric and surface forcing is important (Maykut and Untersteiner 1971; Ledley 1991; Marsh 1999; Langlois, Mundy, et al. 2007). The covariance of physical, thermodynamic, and electrical properties of snow and sea ice; the sensitivity of these complex interactions to feedback processes; and the utility of quantifying these conditions with the all-weather and day or night capabilities of passive and active microwave remote sensing can allow for the parameterization of snow and sea ice cover as they apply to climate and hydrologic needs.

Snow cover evolution and stratigraphy varies seasonally in both the type and the sequence of layers, as the snowpack evolves and matures over the course of a season (Barber et al. 1995; Colbeck and Jamieson 2001). Snow cover is naturally be layered simply due to accumulation

processes throughout the winter. However, warming and cooling periods, melt metamorphosis and refreezing, wind redistribution, snow loading and scouring, and changes in snow density through compaction add complexity to this layering (Wakahama 1968; Colbeck 1991). The layers, crusts, and ice lenses occurring in snowpacks can be discontinuous, with high spatial variation in both vertical and horizontal distribution and properties (Rutter et al. 2014). The presence, position, and order of snow layers or crusts affects the evolution of snow properties both above and below the layer due to modification of the temperature gradient, airflow through the snowpack, subsequent melt-water drainage, and seasonal melt processes, which in turn affect snow grain size and shape, snow density, and snow liquid water content (Colbeck 1991). These, in turn, affect thermodynamic properties, such as albedo and other radiative fluxes, which further affects the evolution of snow properties. An expected increase in the frequency and magnitude of both early and late and winter season rain and melt events in the Arctic (Trenberth et al. 2007) may cause further complexities in snow physical grain morphology, depth, density, snow water equivalent (SWE), and associated dielectric properties, which are of specific interest in the interpretation of microwave remote sensing data.

Changes in snowpack physical and electrical properties associated with meteorological events and seasonal metamorphosis, are detectable as differences in microwave scattering. The metamorphosis of snowpack layers, grain size, and morphology occur at different rates depending on the thickness and structure of the snow cover, due to differing thermal capacity, conductivity, diffusivity, and albedo. Thick and thin snow covers, subject to equivalent meteorological forcing, will exhibit a relative difference in liquid water content and kinetic crystal growth (Colbeck 1991; Sturm et al. 1997; Barber and Thomas 1998). This causes a

relative change in dielectrics and scattering media, which is evident in microwave emission and backscatter. The frequency dependence of microwave energy on extinction, scattering, and reflection cause integration of the snow pack stratigraphy over a greater depth for lower frequencies and over a shallower depth for higher frequencies. Additional error may stem from models that employ linear relationships between snow water equivalent or snow depth and microwave scattering, when considering complexly-layered snow packs as, layer constituents can affect frequencies in a non-linear fashion. Further complications arise from a variety of snow conditions that may result in similar microwave signatures. An understanding of the modification of microwave energy by specific components of snow allows for an inversion of snow properties. The interactions of microwave energy and snow are complicated by the organization of snow grains of varying sizes at spaces smaller than incident micro-wavelengths (*i.e*. snow grains), and by layering within the snowpack (Tedesco and Kim 2006). Therefore, the overall response of microwave scattering to snow cover lies not in the simple averaging of snow properties, but in the properties of each layer and the sequence of the layers themselves (Colbeck 1991). The differential response to thermal events for thin and thick snow packs due to the low thermal conductivity of snow, and associated changes in electrical properties coupled with microwave remote sensing, allows us to gain information about snow depth and snow water equivalent distributions. These are important to gaining understanding of the response of components of layered snow cover to changing atmospheric and climatic conditions, particularly in expansive regions with sparse local observations.

There are several advantages to passive microwave systems in that they are less expensive, require less power, have a relatively higher temporal resolution of measurement, and have been

in operation for nearly 45 years thereby permitting time series monitoring for climate studies. This has enabled thorough exploration of issues and validations for emission retrievals, such that passive satellite data is employed in an operational SWE retrieval scheme (ESA GlobSnow), which has been used to produce a long term climate record (Takala et al. 2011). Disadvantages of passive satellite systems include a relatively low spatial resolution, which requires pixel decomposition techniques, thereby adding complexity to interpretation of brightness temperature. There are several advantages to active microwave systems in that they have a higher spatial resolution, and generate their own illumination, which is a constant and known quantity. However, these active systems are relatively newer (particularly those capable of multiple polarizations) but are more expensive, and require more power relative to passive systems, which reduces temporal resolution due to recharging limitations. Validation has been conducted for these systems and simple operational schemes are in development; however, there are currently no major operational snow assimilation schemes.

Issues of spatial and temporal scale are pertinent when considering the millimeter scale at which snow properties vary (e.g. Barber et al. 1994, Harper and Bradford 2003; Geldsetzer et al. 2007, Lemmetyinen et al. 2010). The relatively coarse spatial resolution of satellite-based microwave remote sensing necessitates the decomposition of microwave retrievals from large areas consisting of several surface-cover types with varying physical and electrical properties (Kurvonen and Hallikainen 1997). Mixture ratios are used in SWE inversion algorithms to attempt to account for variations in emission and backscatter contributions. However, the vertical structure of the snowpack affect physical, thermodynamic, and dielectric properties of snow, which can cause significant differences in both observed and modeled brightness temperatures

and backscatter, increasing uncertainties through internal reflections and transmissions within and between layered snow components. Therefore, surface-based radiometers and scatterometers have been employed to investigate plot-scale snow properties, in order to reduce issues of scale variability. Surface based platforms allow for sampling of relatively homogeneous (i.e. internally consistent) snow types, and destructive sampling in the footprint of the scanned surface. This can improve confidence that the observed snow properties are being directly and consistently measured by surface based radiometer or scatterometer, improving linkages between snow properties and microwave observations and simulations.

Operationally, snow cover in the Arctic has been parameterized simply as one- or two-layer media, employing weighted averages of the entire snowpack for SWE retrieval in assimilation schemes (e.g. Barber et al. 1995; Pulliainen 2006; Yackel and Barber 2007, Takala et al. 2011;). Current state-of-the art assimilation schemes are exploring the development of two and three layered snow covers, which update snow physical and radiative models with available in situ snow and meteorological observations (Sun et al. 2004; Andreadis and Lettenmaier 2006; Pulliainen 2006; Durand 2007). These are focused toward providing estimates for large areas with few in-situ observations, as exemplified by the Canadian Arctic (Matcalfe and Goodison 1993; Langlois et al. 2009). Current approaches to SWE retrieval that apply stand-alone algorithms employing microwave data are not sufficiently accurate for operational hydrologic needs at the pixel scale (Foster et al. 1997; Pulliainen 2006). Current operational retrieval algorithms show spatial and temporal bias (Chang et al. 1987a; Matzler 1994; Matzler and Wiesmann 1999; Kelly et al. 2003; Andreadis and Lettenmaier 2006; Lemmetyinen et al. 2010; Takala et al. 2011). Within the context of an expected increase in winter melt and rain events,

analysis of the effects of snow grain size and the components of snowpack layering on microwave brightness temperature and backscatter observations and simulations are required to improve inversion and assimilation of snow cover properties (Hallikainen and Jolma 1992; Foster et al. 1997; Pulliainen 2006; Durand and Margulis 2006; Lemmetyinen et al. 2010; Durand et al. 2011).

1.2 Research Objectives

The overarching research questions for this work are:

a) How does a more complexly-layered representation of snow impact active microwave remote sensing retrievals, with regard to snow type, snow layered structure, and snow microstructure over first year sea ice?
b) What are the key snow layer types pertinent to a more complex representation of snow in passive remote sensing over land?
c) How well are these snow layer types represented in microwave emission and backscatter simulations?
d) What are the implications of employing a snow thermodynamic model, with regard to simulation of the layered components of snow physical and electrical properties, key to microwave simulations and observations, in consideration of a simple operational assimilation technique?

These overarching objectives are addressed through a number of research questions posed in a collection of peer-reviewed papers that comprise this thesis.

Chapter 3

1. What are the observed geophysical characteristics and C-band backscatter signatures for a complexly-layered snow cover on first-year sea ice?
2. How do observed and simulated C-band backscatter compare for a complexly-layered snow cover over first-year sea ice?
3. How do the components of a complexly-layered snow contribute to C-band backscatter simulations over first-year sea ice?
4. What are the implications of the results of the previous research questions to microwave backscatter classification of sea ice?

Chapter 4

5. How are scattering contributions for key snow layers and properties represented in the multilayer Helsinki University of Technology (HUT) snow microwave emission simulations, when compared to 19 and 37 GHz dual polarization (V, H) observations?
6. What are the implications for consideration of a multilayer HUT model in the GlobSnow SWE assimilation scheme?

Chapter 5

7. How does NARR compare to in-situ meteorological data with regard to variables pertinent to SNTHERM89.rev4?
8. How does SNTHERM89.rev4 output compare to in-situ snow structure and geophysical properties pertinent to C-band microwave backscatter over first-year sea ice?

9. How do simulated backscatter signatures based on SNTHERM89.rev4 output compare to simulations from observed snow structure and properties, and observed backscatter for complexly-layered snow over first year sea ice?
10. What are the implications for the use of the SNTHERM89.rev4 thermodynamic model in an operational scenario for simulation of C-band backscatter over first-year sea ice?

1.3 Research Structure

The research questions are addressed in chapters of this thesis, which is a collection of papers accepted and submitted for peer-review publication. Little change has been made to the manuscripts, and as such, there is some redundancy in this thesis.

Chapter 2 provides background information pertinent to snow and sea ice physical, thermodynamic, and electrical properties; an introduction to passive and active microwave remote sensing; to multilayered microwave emission and backscatter models (the multilayered modification of the Helsinki University of Technology snow microwave emission model (HUT) and the multilayer snow and ice backscatter model (MSIB)), and briefly discusses the GlobSnow snow assimilation scheme and the SNTHERM89.rev4 snow thermodynamic model. Portions of the active microwave theory in Chapter 2 were published in Fuller (2008) and Fuller et al. (2009).

Chapter 3 presents a case study of observed and modeled C-band microwave backscatter signatures for a complexly-layered snow cover on smooth, landfast, first-year sea ice. This chapter investigates how complexly-layered snow affects the backscatter, by comparing signatures with those for a simple snow cover, and through model sensitivity analysis. Backscatter signatures are obtained using a surface-based scatterometer, on snow covered first-

year sea ice in Hudson Bay, Canada. Coincident in situ snow and ice geophysical measurements, and on-ice meteorological observations, describe the snow cover formation and structure. A multilayer snow and ice backscatter model is used to iteratively add and subtract components of the complex snow cover to assess their impacts on the overall backscatter. For incidence angles between 20° and 70°, the backscatter from a complex snow cover on smooth first-year sea ice is significantly higher than backscatter from a simple snow cover on similar sea ice. Sensitivity analysis suggests that rough ice layers formed within the complex snow cover and those superimposed at the sea ice interface are the physical mechanisms that affect an increase in surface and volume backscattering through suppression of brine wicking processes. This has implications for sea ice mapping, geophysical inversion and snow thickness studies.

Portions of Chapter 3 have been presented and accepted for publication in:

Fuller M, Geldsetzer T, Gill J, Yackel J, Derksen C. 2014. C-band backscatter from a complexly-layered snow cover on first-year sea ice. Hydrological Processes. 28: 4614-1625.

Fuller M, Gill J, Geldsetzer T, Yackel J. 2013. Observations and modeling of complexly-layered snow on first-year sea ice using C-band microwave remote sensing. 2013 Eastern Snow Conference. Huntsville, ON.

Chapter 4 presents the unique excavation of snow layers to compare observed and modeled plot-scale brightness temperature (T_B) values for 19 and 37 GHz, with regard to snow water equivalent (SWE), snow type, grain size, and layered structure, for three land cover types acquired near Churchill, Manitoba, Canada in March of 2010. In-situ snow geophysical

measurements were input to the Helsinki University of Technology (HUT) multi-layer snow emission model and performance was characterized by RMSE and MBE. Emission scattering from depth hoar was disproportionate to its SWE contribution when compared to other snow types, and masked observed scattering contributions from upper snow layers. The simulated and observed T_B diverged above 130 mm SWE, as the model did not capture scattering extinction or snowpack emission. These may impact the initial effective grain size optimization process if applied to the GlobSnow SWE assimilation technique. Grain size is optimized to fit emission simulations to TB from satellite observations; the model's continued sensitivity to SWE above observed signal saturation may be attributed to the existing snowpack. These inaccuracies may then by carried forward in the assimilation process, through variance calculations use to weight the contributions of assimilation modules, leading to less accurate SWE retrievals.

Portions of Chapter 4 have been accepted for publication:

Fuller M, Derksen C, Yackel J. 2015. Plot scale passive microwave measurements and modeling of layered snow. Canadian Journal of Remote Sensing. CJRS-15-0023.R2 (In Press).

Chapter 5 presents a comparison of a coupled snow thermodynamic and radiative transfer model with in-situ active microwave signatures of snow covered, smooth, first-year sea ice. Within the context of developing data inversion and assimilation techniques for C-band backscatter over sea ice, snow physical models may be used to drive backscatter models for comparison and optimization with satellite observations. Such modeling has potential to enhance understanding of snow on sea ice properties required for unambiguous interpretation of active

microwave imagery. An end-to-end modeling suite is introduced, incorporating regional reanalysis data (NARR), a snow model (SNTHERM), and a multi-layer snow and ice active microwave backscatter model (MSIB). This modeling suite is assessed against measured geophysical properties of snow on sea ice, and observed active microwave backscatter. NARR data was input to the SNTHERM snow thermodynamic model, in order to drive the MISB model for comparison to detailed geophysical measurements and surface-based observations of C-band backscatter of snow on first-year sea ice. The NARR data was well correlated to available in-situ measurements, with the exception of long wave incoming radiation and relative humidity, which impacted SNTHERM simulations of snow temperature. SNTHERM reasonably represented snow grain size and density when compared to observations. The application of in-situ salinity profiles to one SNTHERM snow profile resulted in simulated backscatter close to that driven by in-situ snow properties. In other test cases, the simulated backscatter remained 4 to 6 dB below observed for higher incidence angles, and when compared to an average simulated backscatter of in-situ end-member snow covers. Development of C-band inversion and assimilation schemes employing SNTHERM89.rev4 should consider sensitivity of the model to bias in incoming longwave radiation, the effects of brine, and the inability of SNTHERM89.Rev4 to simulate water accumulation and refreezing at the bottom and mid-layers of the snowpack. These are necessary to accurate simulation of thermodynamic response, brine wicking and volume processes, snow dielectrics, and microwave backscatter from snow on first-year sea-ice.

Portions of Chapter 5 have been accepted for online publication in The Cryosphere Discussions and publication in The Cryosphere:

Fuller M, Geldsetzer T, Yackel J, Gill J. 2015. Comparison of a coupled snow thermodynamic and radiative transfer model with in-situ active microwave signatures of snow covered smooth first-year sea ice. The Cryosphere Discussions. 9: 1-37. (Accepted to The Cryosphere with minor revisions).

Chapter 6 presents a summary and conclusions of the results of this thesis, recommendations for future work, and concluding remarks.

Contributions to the collections of papers comprising the chapters of this thesis can be found in Appendix A: Contributions.

Chapter Two: **Background**

Chapter 2 Overview

This chapter provides background information pertinent to snow and sea ice physical, thermodynamic, and electrical properties; an introduction to passive and active microwave sensing; an introduction to multilayered microwave emission and backscatter models and associated challenges; and briefly describes the GlobSnow assimilation scheme and the SNTHERM thermodynamic snow model.

2.1 Snow and Sea Ice Physical, Thermodynamic, and Electrical Properties

2.1.1 Context

Snow plays an important role in radiative interactions due to its thermodynamic properties and high albedo (Robok 1983). In a review of literature by Arons and Colbeck (1995), snow cover is recognized by many studies as having a distinct and important role with regard to radiative and chemical transfer processes, to moderation of the thaw and freeze of soils, as an important freshwater input, and as a control of sea ice formation, ablation, extent, and thickness (Maykut 1982; Curry et al. 1995). This is important to global climate systems due to the significant amounts of energy involved in sensible and latent heat exchanges (Serreze and Barry 2005). As the most seasonally variable component of the cryosphere, the impacts of variations in climate on snow cover must be better understood (Marsh 1999).

2.1.2 Physical Properties of Snow

Snow is water in solid state that is created during precipitation in the atmosphere and the crystallization of ice particles (Sing 1992). Its accumulation on the ground causes almost immediate metamorphosis. From newly formed hexagonal snow crystals with dendritic

appendages, snow crystals break into more rounded shapes and needle snow (dendritic constituents) upon meeting with the ground or existing snow cover. Snow on the ground is comprised of ice, water, air and impurities (Wiscombe and Warren 1980). Once on the ground, snow grain metamorphosis is generally due to either a strong temperature gradient (kinetic growth or rounding of snow crystals) or melt-freeze processes (sintering of snow crystals). Snow acts as an insulator due to its low thermal conductivity, governed by snow texture, density, and temperature (Mellor 1977; Colbeck 1982); and thermal diffusivity determined by air volume and porosity (Oke 1987). Thermal conductivity describes the amount of heat transferred through media (i.e. snow) when a temperature change is applied; the greater the conductivity, the greater the amount of heat transferred. Thermal diffusivity describes the ratio of heat transfer to the heat capacity. This ratio describes how quickly the amount of heat transfer occurs and, therefore, how quickly the snow layer will change temperature; the greater the thermal diffusivity, the faster the temperature change (Mellor 1977). Oke (1987) provides the example that heat may generate a temperature pulse that travels rapidly through a highly conductive media, but this warming may be slowed by a high heat capacity, and therefore the warming may not penetrate the media very deeply. Strong temperature gradients can exist and persist between the top (snow-air interface) and bottom (snow-ground interface) of the snowpack causing grain metamorphosis (Schneebeli and Sokratov 2004).

In dry snow, when the temperature gradient within the snowpack exceeds ~10°C m^{-1}, kinetic grain growth occurs (Armstrong 1980; Colbeck 1982). An upward vapor diffusion gradient, associated with temperature difference, causes warmer grains to act as source of sublimated vaporous water molecules that then deposit onto the colder grains. This causes growth in the size

of the colder grains by the simultaneous sublimation of neighbouring grains and changes the morphology of the grains from rounded (equilibrium form) to elongated and faceted (kinetic form), and vice versa, depending upon the temperature gradient (Colbeck 1983). Over time, through microscale heat and mass transfer, the bottom part of the snowpack forms large hoar grains, as vapor is transported from the warmer-bottom to the colder-top of individual crystals (Colbeck 1983; Langlois et al. 2010).

In wet snow, grain metamorphism occurs under three regimes: pendular, funicular, and saturated. The pendular regime is characterized by water isolated in the snowpack, and continuous air paths through the inter-granular pore space (~7% pore volume); the funicular regime has a higher degree of saturation with continuous liquid paths through the inter-granular pore space (~7% to ~14% pore volume); the saturated regime is characterized by saturation (~14% to a maximum of ~20% pore volume) of the porous inter-granular space with liquid water (Colbeck 1982; Denoth 1999).

During the pendular regime, the snow grains undergo surface tension and capillary action causing rounding of grains and ring shaped configurations of water between grains, which may form large poly-aggregate crystals through melt and refreeze cycles (Denoth 1999). The funicular regime has a variety of grain morphologies ranging from poly-aggregate crystals to spherical cohesionless particles (Colbeck 1982). In saturated snowpacks, the smaller grains are at lower temperature when compared to larger grains, and the smaller grains lose size through mass flow to larger grains; grains are generally individual, spherical, and cohesionless (Colbeck 1982).

2.1.2.1 Snow Stratigraphy

The stratigraphy of snow and the sequence of the layering within a snowpack affect airflow through the snowpack, thermal, chemical, and dielectric properties; subsequent melt-water drainage; and seasonal melt processes (Colbeck 1991). Snow covers would be layered simply due to storm cycles throughout the winter; however, warming and cooling periods, melt metamorphosis and refreezing, wind redistribution, snow loading and scouring, and changes in snow density through sublimation also create a more complex layering arrangement (Wakahama 1968; Colbeck 1991). Melt-water drainage and refreezing can also cause vertical ice columns to form within the snowpack adding further complexity to snow pack structure (Marsh and Woo 1984). Snow grain metamorphosis occurs at relatively varying rates within and between snow layers, and above and beneath ice crusts, due to effects of layering and density on snow thermodynamics (Colbeck and Jamieson 2001). Snow layering and grain morphology cause changes in the combined snow density and depth, or SWE (Kelly et al. 2003). This affects thermodynamic fluxes, and causes further complexities in grain morphology, snow density, and dielectric properties, which are specifically of interest in the interpretation of microwave remote sensing. Additionally, the seasonal variation in stratigraphic sequence and composition further complicate temporal and spatial predictions of snow pack properties (Colbeck 1991). In addition to snow grain morphology, the characteristics and sequencing of snow layering are of importance to thermodynamic processes and feedbacks; however, currently snow is often parameterized as a relatively homogeneous medium for Arctic applications involving passive and active microwave remote sensing (Colbeck 1991; Barber et al. 1995; Pulliainen 2006; Yackel and Barber 2007; Takala et al. 2011).

From winter to early melt, the snow cover in the Arctic is generally characterized as a two layer system consisting of randomly oriented fine-grained lower density fresh or windslab snow overlying coarse-grained depth hoar of variable density (Crocker 1992; Barber et al. 1995). Thickness of snow cover on Arctic sea ice varies from ~0 to ~60 cm, with a mean value shown in late spring about ~20 cm with a density averaging ~0.3 g cm^{-3} (Table 2.1) (Warren et al. 1999; Sturm et al. 2002; Sturm et al. 2006; Langlois and Barber 2007). If the snow is deposited under high wind conditions, layers of very small closely-packed, randomly-oriented grains of windslab may exist between the fresh snow and depth hoar. Windslab has the highest density, and fresh snow the lowest (Sturm et al. 2002). The basal depth hoar consists of large faceted (typically 5 mm – 15 mm diameter) angular snow grains formed as a result of vertical temperature gradient metamorphic processes. Spatiotemporal variability stems from several factors including vegetation height, topography (Essery and Pomeroy 2004), ice roughness, storm length and intensity, precipitation type, and predominant wind direction and speed, among others (Iacozza and Barber 2001).

Table 2.1. Properties of snow and ice. From Marshall (2011).

Property	Freshwater	Ice	Sea Ice	Fresh Snow	Settled/Wet Snow	Firn
Density (kg m^{-3})	1000	917	720-940	20-150	250-550	550-830
Albedo	0.1	0.1-0.6	0.1-0.7	0.8-0.9	0.4-0.6	0.3-0.4
Thermal Conductivity (W m^{-1} C^{-1})	0.56	2.11	1.91	0.03-0.06	0.1-0.7	0.7-1.5
Heat Capacity (J g^{-1} C^{-1})	4.218	2.12	2.12	2.09	2.09	2.09
Thermal Diffusivity (m^2 s^{-1})	0.13	1.09	1.06	0.22	0.3	0.69
Latent Heat of Fusion (J g^{-1})	334					
Latent Heat of Condensation (J g^{-1})	2500					
Latent Heat of Sublimation (J g^{-1})	2834					

2.1.2.2 Components and Properties of First-Year Sea Ice

First-year sea ice forms from sea water as it reaches the freezing point, ~ -1.8°C due to salinity depressing the freezing point. Frazil ice, slush, and columnar crystals form initially, as sea water is subject to cooling from the air and heat lost to melting of snowfall. Stratification of the water due to convection stops at the freezing point and bonding of ice particles occurs forming a thin cover of nilas, which may undergo wave action to form and pancake ice. Snowfall that does not fully melt upon contact with the sea water forms slush. These processes allow for the downward addition of sea ice as heat is lost, through conduction, to the atmosphere. Brine is rejected from the ice, depending on the growth rate, as it forms. During freeze-up, sea ice accumulates brine in pockets within the pore spaces between ice crystals. As pressure inside the brine pockets increases, brine is rejected from the ice depending on the growth rate, which results in exclusion of brine into either the lower lying sea ice- ocean interface or upward to the sea ice surface (Martin 1979; Drinkwater and Crocker 1988); the salt expelled to the air ice interface forms crystalline structures (frost flowers). As the ice surface stabilizes, it provides a platform for snow accumulation, and the frost flowers at the snow-ice interface contact with overlying snow. A vertical temperature gradient in the snow-pack develops, resulting in relatively higher temperatures at the snow ice interface and relatively lower temperatures at the snow air interface creating depth hoar at the snow-ice interface. Brine wicking through capillary action in the basal depth hoar increases the brine volume in the snow basal layers (Nakawo and Sinha 1981; Cox and Weeks 1988) resulting in brine-wetted snow. The presence of brine, forced from sea ice into overlying snow cover during first-year ice formation and subsequent changes in the vapor pressure gradient, affects the dielectric and thermal properties of snow cover and, therefore, affects ice formation and ablation timing and rates (Maykut and Untersteiner 1971; Crocker

1984; Geldsetzer et al. 2009). Seasonal ice reaches thickness limits of ~2 m in March, and is composed of ice with air and brine inclusions, before undergoing complete ablation. Sea ice that remains for more than one season (multi-year ice) undergoes several melt and refreeze processes, resulting in the further expulsion of brine, resulting in ice with little salinity (Weeks and Ackley, 1986).

2.1.2.3 Snow characterization

International snow classification schemes developed by Colbeck et al. (1990) and updated by Fierz et al. (2009) provide the basis of terms for characterizing snow physical properties, such as grain morphology, density, liquid water content, temperature, layer thickness and snow cover thickness. These reports describe the physical characteristics of the snow itself, methods of measurement, and the process by which the snow arrived at its current state and morphology.

2.1.3 Arctic Surface Energy Budget

The uneven distribution of the Sun's incident radiation on the Earth, due to the tilt of the Earth's axis of rotation relative to its orbit around the Sun, results in differential insolation dependent upon latitude *i.e.* a surplus of energy at the equator and a deficit of energy at the poles. The Sun's energy incident upon the top of the atmosphere (1366 W m^{-2} direct, 341 W m^{-2} average), is distributed between the wavelengths of 0.15 μm to 4 μm, with a peak intensity near 0.5 μm (Serreze and Barry 2005). About 30% is reflected back to space by the atmosphere, clouds and the Earth's surface, leaving ~239 W m^{-2} for absorption and re-radiation, which drive climate processes (Figure 2.1)(Marshall 2011). Seasonally, the amount of shortwave energy available to the Arctic is small during the arctic night, and long wave interactions dominate. During the Arctic day short and longwave interactions are complex, and several energy interaction scenarios

are possible. The condition of snow, sea ice, ocean, and atmosphere determine the results of the interaction of available energies within and between the components of the cryosphere.

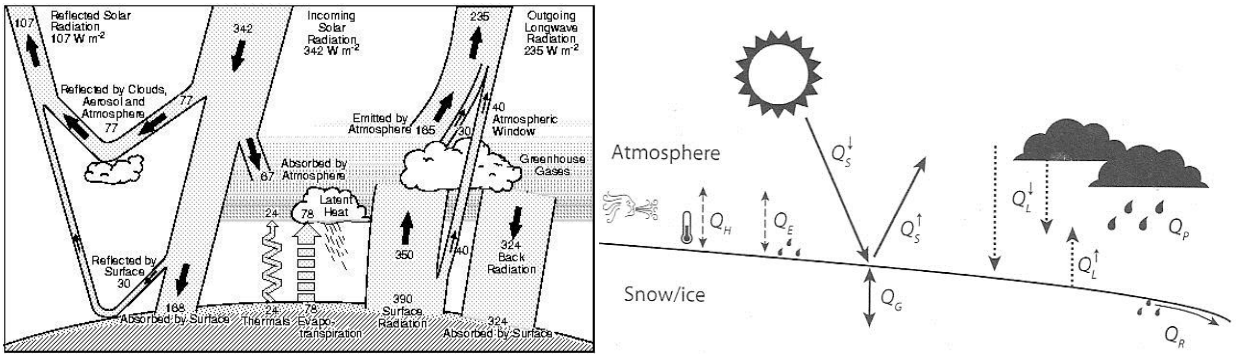

Figure 2.1. Left: The Earth's mean global energy budget (from Kiehl and Trenberth 1997). Right: The components of the surface energy balance (from Marshall 2011).

The surface energy budget (Figure 2.1) can be represented by,

$$Q_N = Q_S^{\downarrow} - Q_S^{\uparrow} + Q_L^{\downarrow} - Q_L^{\uparrow} + Q_G + Q_H + Q_E + Q_P - Q_R \qquad \textit{Eq. 1}$$

where $Q_S^{\downarrow}$ and $Q_S^{\uparrow}$ are incoming and reflected shortwave radiation (VIS), $Q_L^{\downarrow}$ and $Q_L^{\uparrow}$ are incoming and outgoing longwave radiation (IR), Q_G is the conduction and radiative transfer of snow/ice, Q_H and Q_E are latent and sensible heat fluxes, and Q_P and Q_R represent sensible heat in advected by precipitation and runoff, respectively (Marshall 2011). A surplus of energy is either raising the temperature of water, snow/ice or melting the snow/ice; conversely a deficit of energy it is either lowering snow and ice or freezing liquid water. Sublimation of snow is change in phase due to vapor gradient. At the Earth's surface, snow has an upper limit of 0°C temperature and 4.85 g kg^{-1} specific humidity (Hood et al. 1999); therefore, when the specific humidity of the atmosphere is > 4.85 g kg^{-1}, a vapor gradient exists which will evaporate free water or sublimate snow.

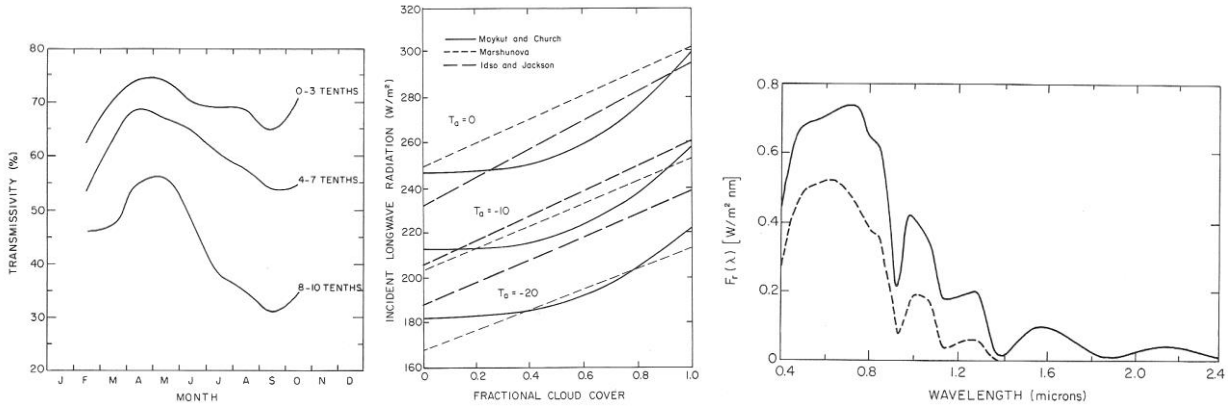

Figure 2.2. The effects of seasonal cloud coverage on total atmospheric transmissivity (left), the effects of temperature and fractional cloud cover on $Q_L^{\downarrow}$ (middle), and the effect of heavy overcast on spectral distribution of $Q_S^{\downarrow}$ during early summer ((right) reduction from clear sky (solid) vs. cloud cover (dashed) is ~45%). From Maykut (1986).

As noted, longwave radiative exchanges dominate in the winter, and depend upon the atmospheric temperature and water vapor (Figure 2.2). As the radiative temperature of the atmosphere is generally less than that of ice, an upward longwave flux moves heat from the ice to the atmosphere. During the spring and summer the presence of low clouds and water vapor near the ice/ocean surface, reduce the long wave losses from the ice,

$$Q_L^{\downarrow} = \varepsilon_a \, \sigma T_a^4 \qquad \textit{Eq. 2}$$

where σ is the Stefan-Boltzman constant (5.67 x 10^{-8} W m^{-2} K^{-4}), T_a is the 2 m air temperature, and ε_a is the emissivity of the atmosphere dependent upon fractional cloud cover and partial vapor pressure near the surface (Figure 2.2) (Maykut 1986). Upwelling longwave radiation is due to the near blackbody emissivity of snow,

$$Q_L^{\uparrow} = \varepsilon_s \, \sigma T_s^4 \qquad \textit{Eq. 3}$$

where ε_s is close to 1, and T_s is the surface temperature (Maykut 1986).

Shortwave radiative exchanges dominate the summer season driving melt, with large cloud cover fraction resulting in primarily diffuse radiation (Figure 2.2),

$$Q_S^{\downarrow} = Q_{S0}\cos(z)\psi^{P/[P_0\cos(z)]} \qquad \textit{Eq. 4}$$

where Q_{S0} is the top of atmosphere irradiance, z is the zenith angle, and $P/P_0\cos(z)$ is site specific air pressure divided by the average air pressure at sea level, which accounts for attenuation due to atmospheric path length. $Q_S^{\uparrow}$ depends upon material albedo, which depends upon snow and ice properties (e.g. snow grain shape, size, density) (Maykut 1986). Albedo is important as it governs how much energy is available for warming and melt, and how much energy is reflected back to the atmosphere. The Earth's surface is heated by absorption of incident shortwave radiation and longwave radiation emitted by the atmosphere near the surface, some of which is then re-reradiated as longwave radiation, thereby heating the atmosphere. The atmosphere then reradiates the longwave both downward toward the Earth and upward to space (Figure 2.1).

Albedo is the diffuse reflectivity of a surface. The ratio of incident to reflected radiation (albedo, α) is frequency dependent. It varies with atmosphere, and the surface and volume physical properties of a media, so that $Q_S^{\uparrow} = Q_S^{\downarrow}\,\alpha$; although albedo can be calculated for the entire spectrum, surface albedo is commonly integrated over wavelengths in the visible spectrum. As such, albedo is the result of diffuse Mie scattering caused by refraction occurring when incident upon snow crystals and ice (Nolen and Liang 2000; Serreze and Barry 2005). As albedo decreases, the amount of energy reflected decreases and the energy absorbed increases;

conversely as albedo increases, the amount of energy reflected increases and the amount absorbed decreases. A relatively higher albedo may cause lags in seasonal melt and formation processes, delaying both ablation and formation of sea ice, which in turn affects albedo. Sensible Q_H and latent Q_E heat flux is associated with temperature and phase change of materials (Table 2.1). Sensible heat is the energy required or released during warming or cooling of a material that does not undergo phase change; and is dependent on the heat capacity of the material. The latent heat flux is used to describe energy exchanges associated with phase change of a material. The sensitivity of the Arctic to changes in temperature is a result of the large energy fluxes associated with melt and freeze processes, and the effects of the phase of water on surface albedo (Barber and LeDrew 1994; Barber et al. 1994).

2.1.3.1 Seasonal Thermodynamic Processes

The relationship of snow depth to sea ice formation and seasonal and multi-year thickness (Figure 2.3) begins with the formation of sea ice in the fall; variation in the timing and type of precipitation (rain/snow) affect ice formation through energy exchange. The energy released from the with the falling of rain onto forming sea ice surface is that of sensible cooling and latent heat associated with phase change as the rain freezes to the ice surface. This process slows ice formation as heat is transferred to the ice, causing warming and melting. The precipitation of snow involves only sensible heat exchanges, involving far less energy, when compared to the latent heat exchanges of rain and sea ice. Snowfall on ocean water or on discontinuous frazil ice will absorb the energy necessary for phase change to water, cooling the ocean surface, resulting in the eventual formation of more ice. For the fall and winter, temperature changes are linked to changes in longwave radiation (Serreze and Barry 2005).

Once ice is established, the snow layer acts to insulate the ice from the atmosphere through a reduced conductive heat flux, buffering the effects of atmospheric temperature variations; ice formation becomes more sensitive to ocean temperature (Figure 2.3). The accumulation for new ice is primarily influenced by the cumulative freezing-degree days (Maykut 1986). Growth occurs from accretion to the bottom of the ice; however, as temperature drops and ocean water undergoes phase change to ice, the release of latent heat slows the process; the thermal conductivity of the ice and snow, limit the accretion to about 2 m for first-year sea ice. The conduction of heat through snow or ice,

$$Q_G = K\left(\frac{\partial T}{\partial z}\right) \qquad \textit{Eq. 5}$$

where K is the thermal conductivity of the material (a function of the material constituents, such as air, ice, water, and brine) and $\frac{\partial T}{\partial z}$ the temperature gradient in the material (Serreze and Barry 2005).

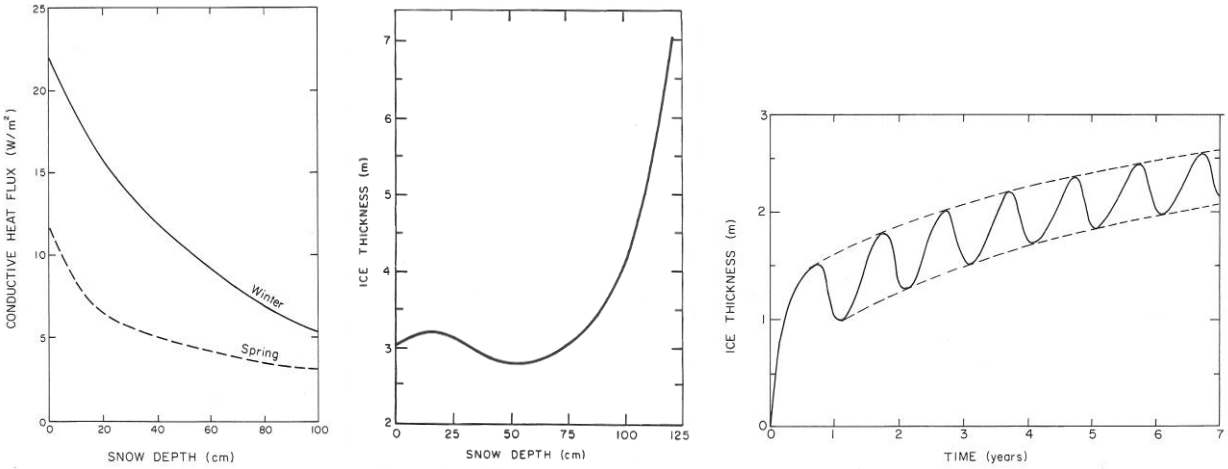

Figure 2.3. The conductive heat flux dependence on snow thickness (left) controls the growth of ice (middle). The growth and equilibrium balance of multi-year ice (right). From Maykut (1986).

Brine supresses the freezing point of water, and thus impacts the thermal conductivity of snow and sea ice, and the volume of brine varies temporally, spatially, and seasonally (Barber et al. 1994). The capillary action governing brine wetting of basal snow layers is thought to resemble that of water wetting (Geldsetzer et al. 2009); therefore, brine wicking to the interstices of snow grains depends upon contact angle, surface tension, snow grain shape, and snow porosity (Colbeck 1974). The thermal conductivity of brine pockets,

$$K_{si} = \rho_{si}/\rho_i \, (K_i + \beta S/T) \qquad Eq.\ 6$$

where *S* and *T* are the salinity (ppt) and temperature of the ice (°C), ρ_i is the density of pure ice, and ρ_{si} is the density of the sea ice (Maykut and Untersteiner 1971). Literature values for β range from 0.09 to 0.12 W m^{-1} ppt^{-1} as density varies with respect to pure ice. Thus, brine in sea ice acts as a buffer for both warming and cooling (Maykut 1986), through latent heat associated with phase changes causing a relative thermodynamic equilibrium between brine and ice (Geldsetzer et al. 2009).

During the spring, the shortwave input increases rapidly, but do not contribute much to surface energy because albedo is high due to snow and ice physical properties. Thus much of the incident shortwave radiation is reflected back into the atmosphere. The small portions of $Q_S^{\downarrow}$ that are absorbed along with longwave radiation increase snow and ice temperature. The brine skim that was expelled by the ice during formation, and subsequently wicked into the snowpack, lowers the melt point allowing for melt to begin at temperatures below 0°C. As snow begins to melt the albedo decreases, such that more absorption and less reflection occurs, creating a positive feedback that ablates the ice (ice-albedo, Figure 2.4). Several mechanisms, including

variation in precipitation type and intensity, low cloud cover and advection, temper this exchange. Additional feedback mechanisms are shown in Figure 2.5.

Precipitation that falls as snow, during melt season, will refresh the surface albedo and slow the ablation process; the energy absorbed by snow will also cool the surface if phase change occurs. Rainfall reduces albedo and raises the temperature of snow as freezing of rain drops occurs. If the rain falls on snow or ice and remains liquid, as the water cools sensible heat will transfer from the water to the ice, contributing to sensible heating or phase change of the surface. As ice melts, ponding occurs and albedo drops further; leads in the ice, sections of open water, and bare land, transfer heat to snow, ice, and atmosphere via advection (turbulent heat flux). These result in absorption and heating, which further melts the snow and ice. These linked positive-feedbacks can ablate first-year ice from bays and fjords in less than a month. Small decreases in albedo provide large increases in the energy available for warming and melt, such that numerical models find a ±5% change in incoming shortwave radiation resulted in 4 m difference in sea ice thickness (Ebert and Curry 1993; Hanesiak 2001). Further, a 20% decrease in albedo would melt all Arctic sea ice in just 3 years (Maykut 1986). Multiyear ice experiences melt at the air-ice interface during the spring and summer; however, this is countered by accretion at the ice-ocean interface; oceanic heat flux to the ice is estimated at ~2 W m^{-2} (Figure 2.4) and is primarily driven by absorption and heating through leads and thin ice (Serreze and Barry 2005). Atmospheric forcing does not completely penetrate through multiyear ice (Figure 2.4); the thermal conductivity (K) is density (ρ) and specific heat capacity (c_p) dependent (Ono, 1968). These determine thermal diffusion, the depth and rate of penetration of atmospheric temperature signatures into snow and ice (Maykut and Untersteiner, 1971),

$$\kappa = K/(\rho c_p) \qquad Eq.\ 7$$

On multiyear ice, melt ponds largely act as a heat storage and transfer mechanism between the ice and the atmosphere, and do not significantly affect ice thickness (Maykut 1986).

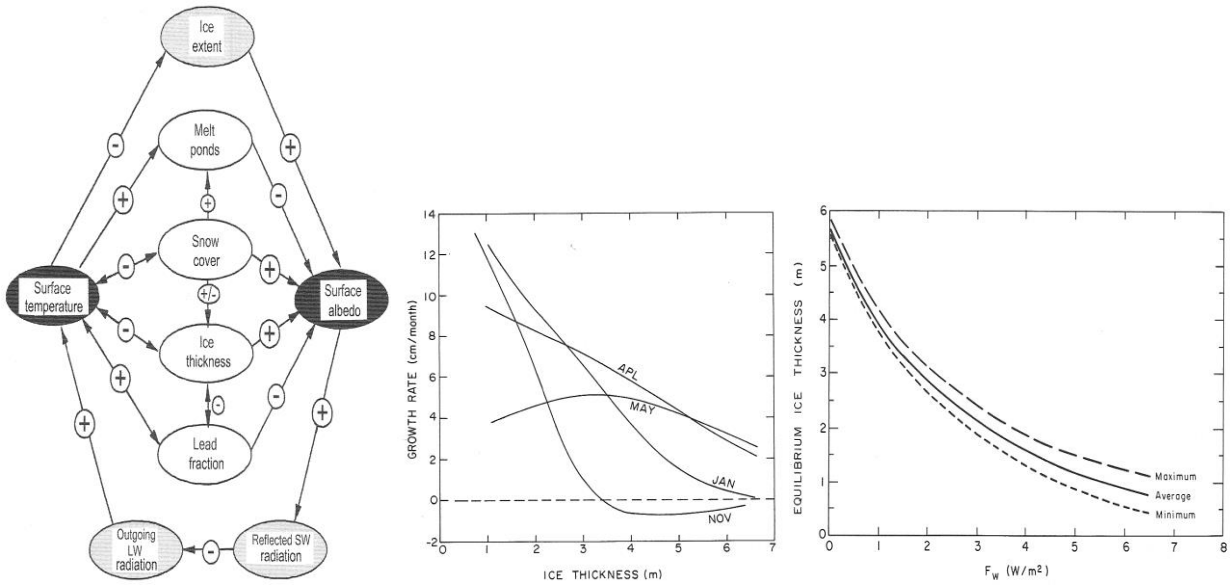

Figure 2.4. Ice-albedo (left, from Serreze and Barry (2005)) and seasonal growth rates for multiyear ice (middle) and equilibrium thickness of sea ice as a function of oceanic heat flux (right), from Maykut (1986)).

Turbulent heating, particularly important in fall accumulation and late winter and spring ablation, is a result of temperature gradients (wind) transferring heat near the surface. Rate of heat transfer depends on surface roughness, wind speed, layer stability, and the temperature and vapor gradients. The absolute values of radiative fluxes are orders of magnitude greater than that of sensible and latent heat exchanges (condensation, evaporation, and sublimation) through turbulent heat fluxes; however, the net result of radiative flux is small, thus turbulent fluxes are

disproportionately important to system heat exchange (Maykut 1986). The ability to transfer turbulent heat is parameterized (Andreas 1987, 2002; Marshall 2011),

Sensible heat (melt ponds, leads, open water, land),

$$Q_H = \rho c_p C_s u(T_a - T_o) \qquad Eq.\ 8$$

Latent heat (condensation/evaporation, and sublimation),

$$Q_E = \rho L C_e u(q_a - q_o) \qquad Eq.\ 9$$

where ρ is air density, c_p is the specific heat of the air, T_a is air temperature at a specific reference height (10 m), T_o is the temperature of the surface, u is wind speed at the reference height, L is the latent heat of vaporization or sublimation, q_a and q_o are specific humidities at the surface and reference level. C_s and C_e are bulk transfer coefficients for sensible and latent heat which are dependent upon the relationship of surface roughness and wind speed increase with height above the surface (Maykut 1986).

The cloud-radiation feedback, typically present during the spring melt and early summer season, is closely tied to the ice-albedo feedback. It has a warming effect for the Arctic through the absorption and re-radiation of longwave radiation and multiple-reflections of shortwave radiation between the surface and low-lying clouds (Serreze and Barry 2005). The strength of this feedback is sensitive to surface albedo and dependent upon cloud fraction, cloud height, cloud depth and microphysical properties, and Sun zenith angle (Curry et al. 1996). Clouds also affect the angle path length and proportion of incoming short wave radiation, increasing the proportion

of diffuse radiation which effectively modifies the zenith angle, increasing the range of incident angles at the surface, which affects albedo (Serreze and Barry 2005). The cloud radiation feedback for the Arctic specifies that a change in surface radiation balance will cause a change in snow, ice, and water quality and distribution, which in turn will modify radiation, sensible, and latent heat fluxes, causing a change in atmospheric temperature and vapor characteristics, thus feeding back to cloud characteristics (Figure 2.5). The predicted warming as a result of these positive feedbacks ignores an increase in radiative cooling predicted by the Stefan-Boltzman law. The cumulative effects of cloud and albedo feedback mechanisms may serve to disproportionately increase temperatures in the Arctic (Ebert and Curry 1992; Ebert and Curry 1993; Hanesiak 2001). Variation in the occurrence of cloud and albedo feedback mechanisms may result in a reduction of atmospheric and oceanic poleward heat transport through a reduction in gradients (Serreze and Barry 2005).

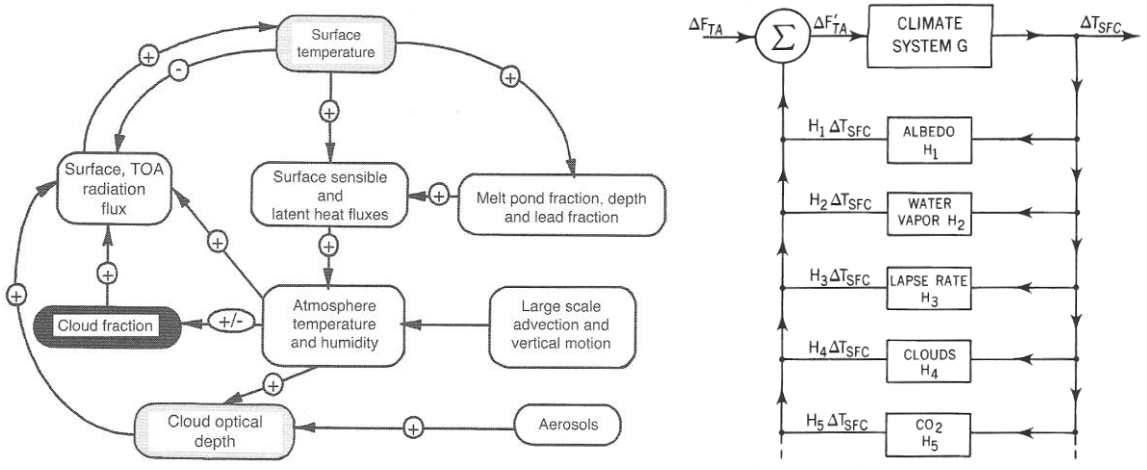

Figure 2.5. Cloud radiation feedback (left, from Curry et al. (1996)), and climate feedback systems (right, from Peixoto and Oort (1992)).

2.1.4 Electrical Properties of Snow and Sea ice

There are two general types of media in nature: conducting and semi-conducting. Conductors (e.g. metal, sea-water) have free electron flow allowing for current; semi-conductors (e.g. ice, pure water, soil) cause a loss in power over distance measured in decibels (dB) (Campbell 2002). Semi- or non-conducting materials are known as dielectric. The velocity of an electromagnetic wave through a dielectric material is less than that in a vacuum by the square root of the complex permittivity (Woodhouse 2006). The permittivity of free space (ε_0) is found to be 8.8542 E^{-12} C^2 N^{-1} m^{-2} (Musil and Zacek 1986); permittivity varies from ~1 to ~80 for most natural materials, though most are at the lower end of the spectrum (Ulaby et al. 1986). The dielectric constant (ε') of a material is a measure of the rotation or polarization of molecules, such as those of water, in response to an incident EM field (Escorihuela et al. 2007); the greater the polarizability of molecules, the higher the dielectric constant (Behari 2005). When the electromagnetic field is removed, it takes time for the molecules to reorient to their original stable arrangement (the relaxation time). Any lag between the direction of the incident EM field and the alignment of water molecules to that field results in energy attenuation in the form of heat (Woodhouse 2006). The attenuation of energy through a dielectric medium is characterized by the dielectric loss (ε''). The components of the dielectric permittivity (also commonly referred to as the dielectric constant) and dielectric loss give the complex permittivity (also commonly referred to as the complex dielectric constant), ε^* (Matzler and Wegmuller, 1987), $\varepsilon^* = \varepsilon' - j\varepsilon''$, where real part of the equation is the dielectric permittivity (dielectric constant) ε' associated with energy storage, and the imaginary part describes the dissipated energy (dielectric loss) ε'', or energy lost to attenuation (Escorihuela et al. 2007).

Although water molecules are electrically neutral, the positive and negative charges are not distributed evenly creating an electric dipole (Levine 2001). Snow as a medium consists of air, ice, impurities, and liquid water (when wet). Ice has a relaxation frequency in the KHz range, which limits the dielectric effects of ice in the microwave region (Matzler 1987), and the strong molecular bonding (high viscosity) in ice restricts the reorientation of molecules to orders of magnitude less than that of liquid water. Liquid water has a high permittivity, and as the relaxation frequency is in the microwave spectrum (due to a relatively lower viscosity), incident microwaves undergo absorption rather than penetration. For dry snow the complex dielectric loss is almost independent of snow structure and the dielectric constant is dependent upon snow density; for wet snow the increase in the dielectric constant and loss are dependent on the volumetric liquid water, and the frequency dependence is the same for that of water (Tiuri et al. 1984).

For pure ice, $\varepsilon' = 3.17$ for frequencies between 10 MHz and 1000 GHz, with slight temperature dependence (Matzler and Wegmuller 1987); the same for air is ~1 (Bean and Dutton 1967; Matzler 1987). For pure ice ε'' is below 1 for frequencies less than 3000 GHz; for typically used microwave frequencies (1 to 100 GHz) ε'' ranges between 0.001 and 0.010 (Figure 2.6) (Jiang and Wu 2004). Dry snow is a mixture of air and ice; therefore, the complex dielectric permittivity can be determined from a weighted mixture of ice and air fractions (i.e. density), when snow is regarded as a homogenous medium (Hallikainen et al. 1986; Matzler 1987). With respect to dry snow, ε' for frequencies ranging from 3 MHz to 18 GHZ,

$$\varepsilon'_{snow} = 1 + X\rho \qquad \textit{Eq. 10}$$

where ρ is snow density and X is a slope coefficient ranging from 1.9 to 2.5 with various studies (Figure 2.6), depending on snow condition and measurement technique (Ambach and Denoth 1980; Hallikainen et al. 1982; Tiuri et al. 1984; Geldsetzer et al. 2009). The dependence on density and relative independence from snow structure (snow grain size and shape) has been noted; however, it has also been noted that varying particle shapes (needles, spheres, oblate spheroids) in theoretical dielectric mixing models for varying snow types (new, very dense, old) do provide improvements (Tiuri et al. 1984). Colbeck (1982) also notes that grain shape and size theoretically increase the dielectric constant, through the resultant shape of funicular water inclusions; however, Geldsetzer et al. (2009) note that confusion arises, as this has also been contradicted by physical measurement (Matzler 1996).

Ulaby et al. (1986), suggests dielectric constant and loss models for dry snow based on the theoretical Polder-van Stanten mixing model with spherical ice crystals (radius 0.5 mm to 5 mm) in an air background at 9.375 GHz frequency which, due to the relative independence of ε'_{snow} to temperature and frequency, are thought valid for the microwave region,

$$\varepsilon'_{dry\ snow} = (1 + 0.51\rho)^3 \qquad \textit{Eq. 11}$$

$$\varepsilon''_{dry\ snow} = \frac{0.34\ v_{ice}\ \varepsilon''_{ice}}{(1 - (0.417 v_{ice})^2} \qquad \textit{Eq. 12}$$

where $v_{ice} = \rho/0.916$, and ε''_{ice} is ~0.001. The loss for dry snow is based on $\varepsilon'_{snow} = \sim 3.15$, and is temperature dependent (Figure 2.6).

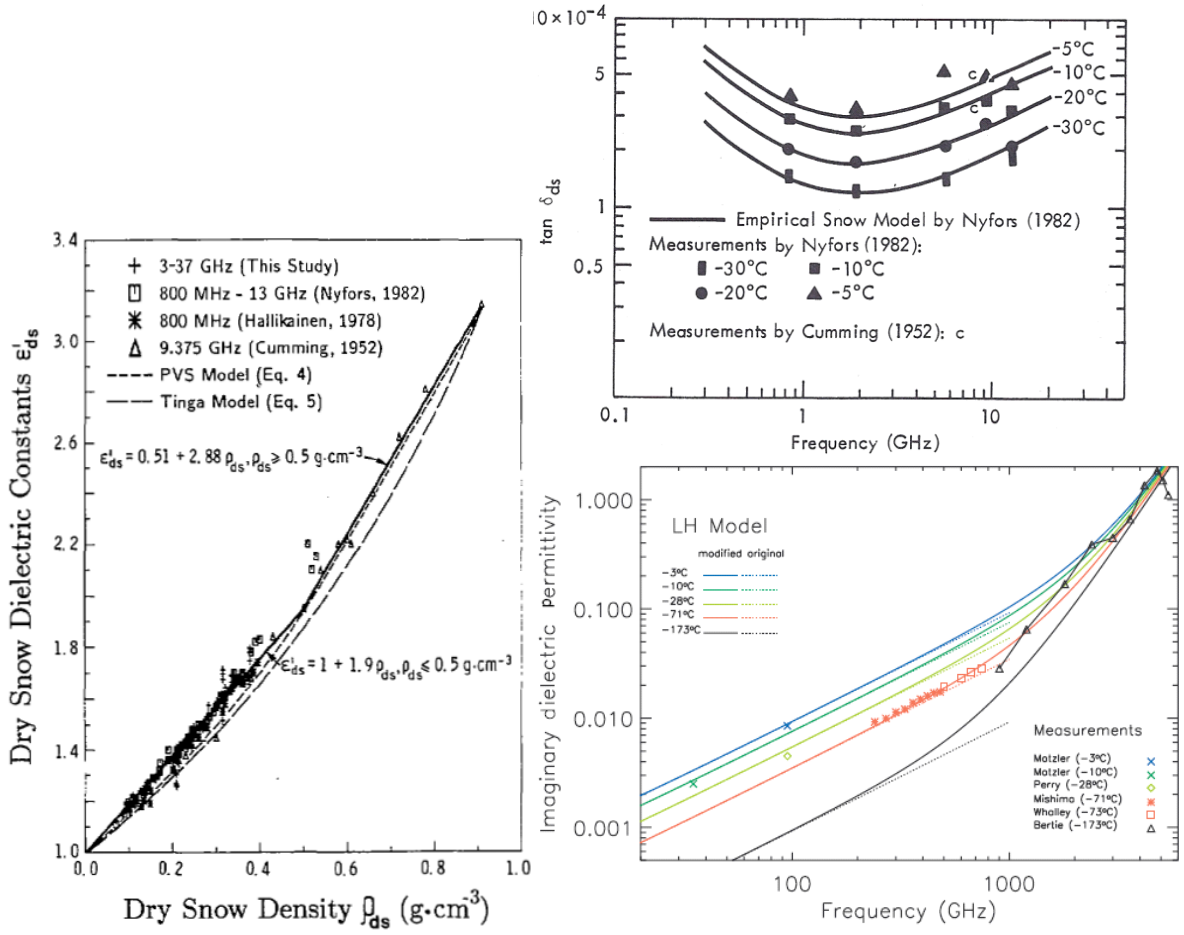

Figure 2.6. Dry snow dielectric constant as a function of density for various studies (Left, from Hallikainen et al. (1986)). Frequency dependent dielectric loss (ε″) of pure ice at various temperatures (Right top, from Ulaby et al. (1986). Right bottom, from Jiang and Wu (2004)).

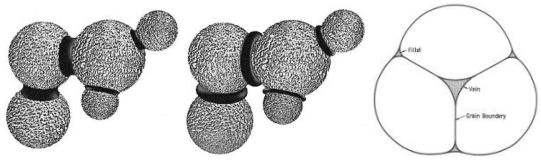

Figure 2.7. Schematic of water menisci at the interstices of ice grains (Left), pendular regime (Middle), from Denoth (1999). Water between crystals (Right), from Colbeck (1982).

Liquid water occurs in moistening macro-porous materials; initially the molecules are bound to a surface contributing only a small increase in permittivity (Figure 2.7) (Behari 2005). As the

liquid water content increases, each subsequent layer of molecules is less bound than the former, until water begins to flow gravimetrically (Spiridonov 1982). Each monomolecular layer is farther away from the surface and is more available for rotation, given an incident EM field, and thus contributes increasingly to the complex permittivity (Escorihuela et al. 2007). The relative fractions of bound and free water depend upon the particle size distribution (texture), particle density, and the shape of the water inclusions (Colbeck 1982; Behari 2005). (Fuller et al. 2008)

The liquid water content of snow determines the definition of wet or dry snow. Wet snow (liquid water content > 1%), defined as having liquid water droplets at the interstices of ice grains, contributes to absorption, causing an increase in the imaginary part of the dielectric constant and a decrease in penetration depth of microwave energy. The dielectric behaviour of liquid water can be described by Debye's empirical equation,

$$\varepsilon^*_{water} = \varepsilon' + j\varepsilon'' = \varepsilon_\infty + \frac{\varepsilon_S - \varepsilon_\infty}{1 + 2\pi j f t} \qquad \textit{Eq. 13}$$

$$\varepsilon'_{water} = \varepsilon_\infty + \frac{\varepsilon_S - \varepsilon_\infty}{1 + (2\pi f t)^2} \qquad \textit{Eq. 14}$$

$$\varepsilon''_{water} = \frac{2\pi f t(\varepsilon_S - \varepsilon_\infty)}{1 + (2\pi f t)^2} \qquad \textit{Eq. 15}$$

where *f* is frequency, ε_S the static dielectric constant, ε_∞ the high frequency limit (relatively constant 4.5 to 4.9), and *t* is relaxation time (Stiles and Ulaby 1981; Matzler 1987). The Debye derived relaxation time t for water,

$$t = \frac{4\pi\eta\alpha^3}{kT} \qquad \textit{Eq. 16}$$

where η is the viscosity, α is the molecular radius, k is Boltzmann's constant (relating particle energy to temperature), and T is temperature, giving a relaxation frequency of ~8.5 GHz for water at 0°C (Stiles and Ulaby 1981). The dielectric constant and loss are presented for liquid water in Figure 2.8 for frequencies ranging from KHz to GHz, and temperatures ranging from 0°C to 100°C.

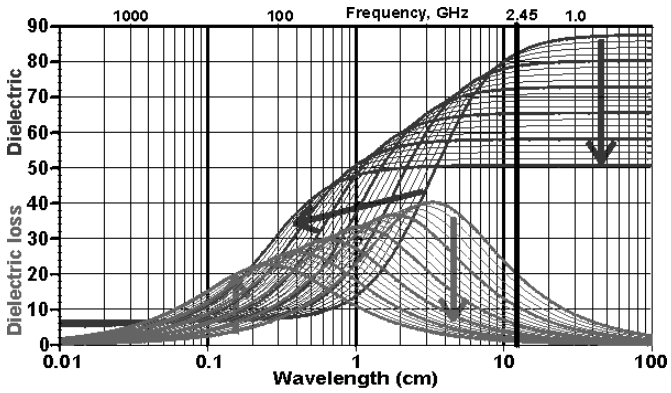

Figure 2.8. The frequency and temperature dependent complex permittivity properties for liquid water (left). Arrows denote increasing temperature from 0°C to 100°C. The Note the relaxation frequency for liquid water at 0°C occurs at ~8.5 GHz. From Chaplin (2011).

For wet snow the weighted mixing model for complex permittivity is similar to that for dry snow, but includes liquid water content. For wet snow the 2 component Polder-Van Stanten mixing model considers water as randomly oriented ellipsoid inclusions in a background of dry snow,

$$\varepsilon'_{wet\ snow} = \varepsilon'_{dry\ snow} + \varepsilon'_{water}\,(0.1\ Wv + 0.8\ Wv^2) \qquad \textit{Eq. 17}$$

$$\varepsilon''_{wet\ snow} = \varepsilon''_{water}\,(0.1\ Wv + 0.8\ Wv^2) \qquad \text{Eq. 18}$$

where Wv is water volume (%), valid for snow in the pendular regime (liquid water content < ~14%) (Colbeck 1982; Denoth 1982; Tiuri et al. 1984). As noted, $\varepsilon'_{wet\ snow}$ and $\varepsilon''_{wet\ snow}$ are frequency dependent with water, thus in the above ε'_{water} and ε''_{water} must be calculated for frequency f, Debye's formulae take the form, *eq.19 and 20*

$$\varepsilon'_{water} = 4.9 + [82.8/(1+(f/f_0)^2] \qquad \text{Eq. 19}$$

$$\varepsilon''_{water} = (82.8(f/f_0)) / (1+(f/f_0)^2) \qquad \text{Eq. 20}$$

where f_0 is the relaxation frequency of water at 0°C (~8.84 GHz) (Tiuri et al. 1984).

Pertinent to snow on sea ice, brine supresses the freezing point of water, impacting dielectric permittivity and loss. The volume of brine wicked into the interstices of snow grains in the basal layers of snow on sea ice create gradients of dielectric permittivity and loss based on brine volume. The capillary action governing brine is thought to resemble that of water wetting (Geldsetzer et al. 2009); therefore, brine wicking to the interstices of snow grains depends upon contact angle, surface tension, snow grain shape, and snow porosity (Colbeck 1974). The brine volume fraction in snow is a function of snow salinity, density, and temperature (Cox and Weeks 1975; Drinkwater and Crocker 1988). A mixture model for the dielectric permittivity and loss associated with brine in snow on sea ice depends upon the connectivity and concentration of salt solution in brine inclusions, and is found in Geldsetzer et al. (2009).

2.1.4.1 Frequency dependent microwave interactions with media: Refraction, Absorption, Reflection, Diffraction, and Scattering

Energy incident upon a planar boundary between two media must be reflected (*i.e.*, scattered), transmitted, or absorbed (Figure 2.9) (Oke 1987) such that,

$$\Psi_\lambda + \alpha_\lambda + \xi_\lambda = 1 \qquad \textit{Eq. 21}$$

where ψ_λ is transmissivity, α_λ is reflectivity, and ξ_λ is absorptivity. Refraction (n) is a velocity modification of energy ($n = c/c_n$) when it is incident upon a substance of different density or complex permittivity (Jensen 2000). Refraction is governed by geometry of a media or target; both transmission and absorption are controlled by dielectric properties. The complex dielectric permittivity is related to the complex refractive index $\varepsilon^* = n^2$, and $n = n' + jn''$,

$$\varepsilon' = n'^2 \qquad \textit{Eq. 22}$$

$$\varepsilon'' = 2n'n'' \qquad \textit{Eq. 23}$$

where n' is the phase speed and jn'' is the loss due to absorption (k_a); this determines the frequency dependent refraction, propagation/scattering, and absorption of incident microwave energy (Matzler 1987; Matzler and Wegmuller 1987). Snell's law predicts the angle of refraction; where the incidence angle is known the angle through media 2 can be predicted (Woodhouse 2006),

$$sin\theta_2 = \frac{n_1\, sin\theta_1}{n_2} \qquad \textit{Eq. 24}$$

Absorption (ka) of energy occurs when the frequency of the radiation is the same as the resonant energy of an atom or molecule; the energy is absorbed and reradiated at a different wavelength (Jensen 2000). Absorption, with respect to microwave remote sensing, is a loss of energy as it is neither scattered (ks) nor transmitted for subsequent scattering. The loss of energy to a media is defined by its absorption coefficient; the transformation of energy into heat over distance into the medium (Ulaby et al 1984, Hallikainen and Winebrenner 1992). Attenuation is an exponential decay of the wave amplitude with distance in a medium, related to penetration depth (δ_p),

$$\delta_p \approx \frac{\lambda\sqrt{\varepsilon'}}{2\pi\varepsilon''} \qquad \textit{Eq. 25}$$

where λ is the wavelength of the incident energy. Penetration (related to ε*) occurs for most applications of microwave remote sensing with the notable exception being liquid water; penetration is the distance over which power is reduced e^{-1} (Ulaby et al. 1984). The extinction coefficient (ke), dependent upon complex permittivity and frequency, for energy through a media is related to absorption (ka) and scattering (ks), such that ke = ka + ks. Scattered energy is that lost to the sensor because of redirection through particle interaction.

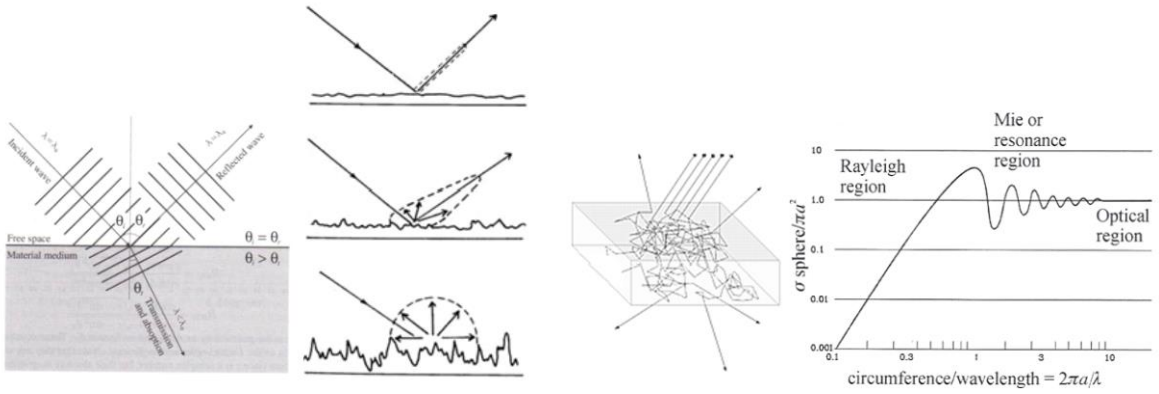

Figure 2.9. Boundary interaction (Left, from Woodhouse (2006)), surface scattering (Middle Left, from Nezlin (2004)), volume scattering (Middle Right, Integra (2010)), radar cross-section for a sphere radius *a*, and incident wavelength (Right, from Woodhouse (2006)).

Woodhouse (2006) described reflection, diffraction, and scattering as the same process occurring on different scales, with the key lying in the size of the elements in proportion to the incident wavelength (Figure 2.9), and the complex dielectric constant and loss of the two media. If the dimensions of media are large when compared to an incident wavelength, and the dielectric constant is high, it can be considered a planar reflecting surface. If the dielectric difference between the two media is small, transmission occurs. The depth of the transmission depends upon the frequency of the energy and the dielectric loss (ka) and scattering loss (ks) within the second media (ke). If the dimensions of media are small, or on the same scale as an incident wavelength, and the dielectric constant is high, the media can be considered a scattering object. Transmission may occur, depending on the dielectric difference between the media, and the loss is governed as previously mentioned. The same fundamental interactions govern each process (Fuller et al. 2008). The interactions are subject to two key properties: the relative complex permittivity's of the media, the shape and size of the boundary in proportion to the incident wavelength. Object boundary and shape must be taken into account as the wavelength

approaches or exceeds the boundary dimensions (Figure 2.9); at these scales the boundary can be considered a discrete object and the wave will diffract or scatter with interaction.

Surface scattering (Figure 2.9) occurs in conditions of two adjacent homogeneous media with a larger dielectric difference. The scattering is governed by surface roughness relative to λ and angle of incident radiation, described by the Fraunhoffer criterion,

$$\sigma < \frac{\lambda}{32\ cos\theta} \qquad Eq.\ 26$$

where σ is the standard deviation of surface height (Ulaby et al. 1986). For a smooth or planar surface the energy leaves the surface in the forward direction at the angle of incidence, resulting in specular reflectance. Diffuse (isotropic) scattering occurs equally in all directions as surface roughness approaches wavelength. As roughness features exceed wavelength, almost all of the incident energy may be reflected back in the incident direction (double bounce). In practical situations, media often present a combination of specular reflectance and diffuse scattering (Trevett 1986). Surface roughness in relation to electromagnetic wavelength affects backscatter probability. The vertical relief, local incidence angle, and surface roughness affect surface scattering/reflection and must be considered.

Energy crossing a media boundary may be available for volumetric scattering within the media. Volume scattering (Figure 2.9) occurs in an inhomogeneous media composed of distributed discrete objects, each having a significant radar cross-section (Woodhouse 2006); volume scattering in snow depends upon snow density and grain size (dielectric constant and scattering cross section), liquid water content and temperature (dielectric loss), and frequency (Ulaby et al.

1986; Moorman 2001; Chen et al. 2003; Scharien 2004). Snow and ice act like volumes under certain conditions; however, surface scattering can dominate if the dielectric difference between the air and snow boundary layer becomes great enough (Woodhouse 2006; Geldsetzer et al. 2007).

2.1.4.2 Measurement and modeling of the electrical properties of snow

Radiometers and scatterometers are used to measure the electrical properties of snow and ice (discussed in more detail in Section 2.2), and have many methods of sampling, requiring careful characterization of snow properties, and reliance on empirical relationships or microwave scattering theory for inversion of snow dielectric and structural properties. Destructive *in situ* sampling is required in order to determine emission and backscatter properties associated with specific snow conditions. Although scatterometer and radiometer measurements are general conducted over natural snow packs, the theory of the foundational relationships occurred in laboratory settings with homogeneous samples (Linor 1980; Ulaby et al. 1986), which may unrepresentative of measured natural conditions (Colbeck 1982; Hallikainen et al. 1986). The importance of the application of remote sensing methods for snow dielectric measurement lies in the potential for all condition, non-destructive sampling, at spatial and temporal resolutions not possible with ground based methods. Work in this area has been and is currently focused on emissivity and backscatter measurements of snow, for modeling inversion of snow physical properties (Hallikainen et al. 1986; Wiesmann and Matzler 1999; Pulliainen 2006).

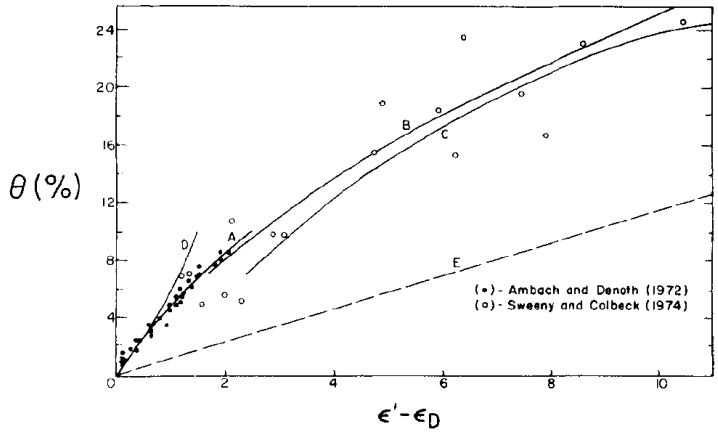

Figure 2.10. The curves A, B, and C (solid black lines) represent theoretical Polder-Van Stanten values of dielectric loss as a function of liquid water content, taking into account the size and shape for water inclusions dependent upon snow grain structure. The black dashed line represents the same, with no account for grain geometry. The dots represent measured data. Curve D is based on measurements conducted by Linor (1980), which were unrepresentative of natural conditions. From Colbeck (1982).

Dielectric properties of snow can be modeled empirically, semi-empirically, and theoretically. As dielectric properties are primarily a function of water content, the accurate accounting of the water content of snow is necessary. The direct measurement of liquid water content is imperfect, and can be insensitive to aspects of the natural configuration of liquid water inclusions (Colbeck 1982). Empirical models may fall subject to error associated with measurement device insensitivity as exampled by Bradford et al. (2009), and particularly when comparing natural and laboratory settings, as exampled by experiments conducted by Linor (1980) (Figure 2.10, Curve D). Care should be taken to compare results that are subject to these discrepancies, with studies involving other devices and under various controls, as well as to theory based results.

Numerical models can assist in understanding complex interactions and feedbacks, which may be impossible to resolve from direct measurement, and allow for sensitivity tests on single variables (Serreze and Barry 2005). Isolating a single variable, even in laboratory environments

may be difficult. The advantage of numerical modeling over direct measurement is generality of application and specificity of characterization, interaction, and sensitivity. Theoretical models must be applicable to practical physical conditions, and should have a physical mechanism or process that can be measured, in order to connect application with theory; without this theoretical model may fall subject to operational irrelevance. Commonly used approximations and coefficients sometimes go ignored (Kontu and Pulliainen 2010). For example, the Delta-Eddington approximation, the Kirchoff scattering model, Small-Perturbation model, Fresnel reflection, and the application of the Debye equation to snow, all contain assumptions and limits to their application. The use of these components requires careful choice based on specific application conditions; the inefficiencies may have undesired cumulative effects when used in concert. Finally, assimilated approaches, combining the greatest level of applicability with the most robust theory, can combine well established aspects of empirical, semi-empirical, and theoretical means in order to minimize error in understanding complex interactions and systems at an operational level (Pulliainen 2006).

2.2 Microwave Remote Sensing

Microwave remote sensing provides an all-weather, all-season, diurnal solution to gathering snow and ice data. Microwave remote sensing is sensitive to snow and ice physical and electrical properties, such as snow water content, snow depth and density (SWE), and brine volume. The results of the satellite microwave retrievals can be more accurate than conventional measurement methods, which tend to overestimate SWE at large scales (Goodison and Louie 1986), are poorly distributed (Robinson et al. 1992), and are biased toward populated areas (Brown et al. 2000; Foster et al. 2005). There exists, however, a high degree of uncertainty in empirical SWE

algorithms, due to the effects of grain size and morphology, snow stratigraphy (Matzler and Wiesmann 1999), brine volume (Barber et al. 1994), and surface cover effects (Derksen et al. 2005; Duguay et al. 2005). The following section briefly describes active and passive microwave fundamentals pertinent to this work.

2.2.1 Radiometer, Scatterometer, and Synthetic Aperture Radar Systems

Passive microwave remote sensing employs a *radiometer* to measure the intensity (and relative attenuation) of radiation emitted from the Earth, at specific frequencies and in specific polarizations. The dimensions of the radiometer horn a control the frequency and polarization of energy received by the antenna. Active microwave remote sensing measurement is accomplished via a *scatterometer,* which emits a beam of radiation illuminating its target, and then receives a backscattered portion of the emitted radiation. Active radar systems can be further subdivided into scatterometers and SAR (Synthetic Aperture Radar). Scatterometers, such as that used in this work, use a conventional beam emitted and received by a relatively small physical antenna and can provide a backscatter signature over a range of incidence angles for a given snow sample site. This allows for the exploration of the effects of snow condition over both surface and volume scattering angles. SAR employs the motion of a craft or satellite to artificially synthesize a relatively lager antenna, which allows for a higher spatial resolution that would otherwise be possible. Satellite based SARs, such as RADARSAT-2, allow for relatively larger spatial coverage, and are used to create images of backscatter for a given area over a relatively smaller range of incidence angle. The bandwidth describes the range of frequency sensitivity of each system, and the beamwidth describes the (angular) instantaneous field of view of the system. Surface-based radiometers and scatterometers allow for a relatively small scan footprints, which

in turn allows for sampling of relatively homogeneous and/or specific snow types. The traditional microwave energy range of the electromagnetic (EM) spectrum is generally recognized to span a wavelength range of approximately 1 mm (1000 GHz) to 30 cm (1 GHz) (Table 2.2), with modern ranges recognized as including wavelengths of 1 m (300 MHz) or more.

Table 2.2. Microwave nomenclature and band ranges for frequency and wavelength. From Woodhouse (2006).

Microwave Nomenclature		
Band	Frequency Range	Wavelength
P (UHF)	0.3 - 1 GHz	1 m - 30 cm
L	1 - 2 GHz	30 cm - 14 cm
S	2 - 4 GHz	14 cm - 7.5 cm
C	4 - 8 GHz	7.5 cm - 3.75 cm
X	8 - 12 GHz	3.75 cm - 2.5 cm
Ku	12 - 18 GHz	2.5 cm - 1.67 cm
Ka	18 - 27 GHz	1.67 cm - 1.11 cm
V	27 - 40 GHz	1.11 cm - 7.5 mm
W	75 - 110 GHz	4.0 mm - 2.7 mm
mm	110 - 300 GHz	2.7 mm - 1 mm

2.2.2 Passive Microwave Brightness Temperature

Energy is radiated according to Planck's Law which describes the intensity of the radiation ($W\ m^{-2}$), per unit direction (sr^{-1}), per frequency (Hz^{-1}), at physical temperature T (Kelvin), and operates according to Planck's function,

$$\beta v(T) = \frac{2hv^3}{c^2}\frac{1}{e^{\frac{hv}{kT}} - 1} \qquad \textit{Eq. 27}$$

where *v* is frequency, *h* is Planck's constant, *c* is the speed of light, and *k* is Boltzmann's constant (Ulaby et al. 1981; Woodhouse 2006). Planck's function predicts an intensity for a given wavelength or frequency of radiation, at a certain temperature. As temperature increases, the intensity increases, and the maximum intensity moves to higher frequencies. In the case of a black body, the theoretical concept of a perfect absorber and emitter of radiation, the energy emitted will equal the energy absorbed. However, in practice, this is not the case, and emissivity is quantified according to how efficiently a body emits energy relative to a black body, for a given frequency (Woodhouse 2006).

The Raleigh-Jeans limit reduces the Planck function to give microwave Brightness Temperature T_B (unpolarized),

$$T_B(v) = \left(\frac{\lambda^2}{2k}\right) Bv \qquad \textit{Eq. 28}$$

$T_B(v)$ is representative of the Raleigh-Jeans equivalent brightness temperature; the temperature required for a black body to produce a given intensity, represented by units of degrees Kelvin. When employing a single polarization the equation is reduced by a factor of 2, giving (polarized),

$$T_B(v,p) = \left(\frac{\lambda^2}{ka}\right) Bv \qquad \textit{Eq. 29}$$

where *p* represents a specific polarization.

As the Earth emits microwave radiation, the ground cover, including soil, vegetation, snow, and ice, will interact with the emitted energy in one of 3 ways (previously described in Section 2.1.4): reflection (ρ), absorption (ka), and transmission (Υ). Given the law of conservation of energy, the total energy must be the equivalent of the sum of the energy reflected, transmitted, and absorbed. In analyzing the energy and the modification that occurs, we can identify and characterize properties of the overlying cover (Ulaby and Stiles 1980). The cover itself may also emit and scatter energy, adding confusion to remote sensing interpretation of physical properties (Matzler 1994).

More simply, brightness temperature can be characterized as the intensity of energy received at the radiometer, initially emitted from the Earth, and which has passed through a media (e.g. snow). It is a frequency dependant function of physical temperature (linearly related) and emissivity, which varies widely for different materials (shape and dielectric properties). Brightness Temperature can be measured in vertical and horizontal polarizations, which are sensitive to snow volume and snow structure, respectively. As the look angle of the receiver increases away from nadir, the differences between horizontally and vertically polarized emissions increase, resulting in more information for analysis. There are several advantages to passive microwave systems in that they are less expensive, require less power, and have been in operation for nearly 45 years. This has enabled thorough exploration of issues and validations for emission retrievals, such that passive satellite data is employed in an operational SWE retrieval scheme (ESA GlobSnow), which has been used to produce a long term climate record (Takala et al. 2011). Disadvantages of passive satellite systems include a relatively low spatial resolution,

which requires pixel decomposition techniques, thereby adding complexity to interpretation of brightness temperature.

2.2.3 Active Microwave Backscatter

2.2.3.1 The Radar Equation

The measurement of echo return is the basis of active microwave systems. This requires determination of the proportion or amount of backscatter from a target. This is done quantitatively with the Radar equation,

$$P_r(Backscattered\ power\ received\ at\ radar) = \frac{P_t}{4\pi R^2} G_t \sigma \frac{A_R}{4\pi R^2} \qquad Eq.\ 30$$

where P_t is the energy per unit time leaving the active microwave system, G_t is the transmitter-receiver gain, $A_R$is the receiver-antenna aperture, and σ is the radar scattering cross-section (Ulaby et al 1981; Fung 1994). The backscattered power received at the antenna is a function of $P_t G_t$ and a spreading loss due to distance ($= {}^{1}/_{4}\,\pi R^2$). The loss is a reduction in power density over a sphere of radius *R* associated with distance from the antenna. The loss is accounted for in both transmit and receive directions; the received signal must be greater than the noise level of the instrument. The signal to noise ratio (SNR) determines if the signal from a target is greater than the noise generated by the system (Ulaby et al. 1982; Woodhouse 2006),

$$\left(\frac{P_r}{N_o}\right) = \frac{P_t G^2 \lambda^2 \sigma}{(4\pi^3) R^4 N_o} \qquad Eq.\ 31$$

2.2.3.2 Radar Cross Section

The radar cross-section (RCS) refers to the proportion of energy, *I*, returned to the radar relative to the know incident energy (Ulaby et al. 1982),

$$\sigma = \frac{I\ received}{I\ incident} 4\pi R^2 \qquad Eq.\ 32$$

The amount of scattering and therefore the value of σ depend upon target shape, dielectrics, orientation, and roughness (Carsey 1992); and upon the observation angle, frequency, and polarization (Ulaby et al. 1981).The RCS approaches zero as less energy is backscattered; the RCS will be larger when the object/media backscatters energy greater than that which would be scattered by an ideal isotropic scatterer. Given these conditions, accurately determining an estimate of the RCS is primary to active microwave remote sensing.

Scattering is considered from discrete targets (*e.g.* wet ice grains, or water inclusions), distributed targets (*e.g.* bare ground), or often a combination of both (e.g. Fuller et al. 2009). For individual targets, the RCS does not change with respect to total area of observation, as the power returned is constant. With distributed targets, as the area of observation increases the total backscattered power increases proportionally. This increase in backscattered power is, therefore, a description of the backscatter with relation to the size of observation area (*A*); and not the desired target observation. It is a result of instrument configuration bias.

Sigma nought σ^0 defines the normalized differential radar cross-section (NCRS) of a target, rendering the measurement unit-less and independent of viewing geometry (Ulaby et al. 1982),

$$\sigma^0 = \frac{\sigma}{A} \qquad \textit{Eq. 33}$$

The averaging of microwave backscatter takes the form,

$$\sigma^0_{(dB)} = 10\log_{10}(\sigma^0) \qquad \textit{Eq. 34}$$

At a given frequency, target roughness and dielectric properties control σ^0 (Carsey 1992). σ^0 is the product of two functions as expressed by (Ulaby et al. 1986),

$$\sigma^0(\theta) = f_{rt}(\varepsilon^*, \theta) \cdot f_s(\rho(\xi), \theta) \qquad \textit{Eq. 35}$$

where $f_{rt}(\varepsilon^*, \theta)$is the dielectric constant (ε*) dependence and $f_s(\rho(\xi), \theta)$is the surface autocorrelation ($\rho(\xi)$) roughness dependence. This forms the basis with which scattering models are related to geophysical properties of a target or surface (Golding et al. 1998).

Phase differences occur as a result of the reflection of an incoming wave travelling different distances to each point on a surface. This scenario considers a surface to be an infinite number of small point scatterers, and considers orientation and density of anisotropic scatterers within the target (Ulaby et al. 1986; Chang et al. 1996).

2.2.3.3 Fresnel Reflection and Penetration Depth

Microwaves are generated via a dipole antenna; a conducting rod activated by an alternating current. The goal is to generate a stream of coherent pulses that all begin with the same phase. Light from ordinary sources, such as the Sun, is not polarized. The vast molecules that comprise the light source are positioned and oriented randomly; each acting like a small dipole antenna.

Individual molecules may radiate energy in a particular polarization; however, the total emitted radiation is a random mixture of waves with polarization occurring in all possible directions. Certain media, such as the atmosphere or snow can filter out waves of a particular polarization. The interaction of polarized waves with a target allows us to determine some of its physical properties based upon the polarimetric properties of the target. (Ulaby et al. 1981; Rees 2006; Woodhouse 2006; Fuller et al. 2009)

The magnitude of reflected and transmitted energy for a near planar surface is defined by Fresnel reflection coefficients for vertically and horizontally polarized waves. The subscript notations (e.g. $_{HH}$) refer to the send/receive polarization configurations respectively in this work,

$$R_{VV} = \frac{\varepsilon \cos\theta_1 - \sqrt{\varepsilon - \sin^2\theta_1}}{\varepsilon \cos\theta_1 + \sqrt{\varepsilon - \sin^2\theta_1}} \qquad \textit{Eq. 36}$$

$$R_{HH} = \frac{\cos\theta_1 - \sqrt{\varepsilon - \sin^2\theta_1}}{\cos\theta_1 + \sqrt{\varepsilon - \sin^2\theta_1}} \qquad \textit{Eq. 37}$$

where ε is the permittivity. As the Fresnel reflection coefficients are complex numbers,

$$\rho_{VV} = R_{VV} R_{VV}^* = |R_{VV}|^2 \qquad \textit{Eq. 38}$$

$$\rho_{HH} = R_{HH} R_{HH}^* = |R_{HH}|^2 \qquad \textit{Eq. 39}$$

where ρ_{VV} and ρ_{HH} are the coefficients for vertically and horizontally polarized waves, respectively; a value of 0 denotes no reflection and 1 denotes total reflection (Figure 2.11 Left) Ulaby et al. 2004; Rees 2006). Note that when θ is ~60° (pseudo-Brewster angle) and ε = 3.2, the

VV has a minimum reflectance and full transmission; concurrently, the HH is both reflecting and transmitting energy at the boundary interface.

The imaginary part of the dielectric constant, ε'', determines the loss of energy as a wave passes through a medium and, therefore, helps define the penetration depth of the EM energy (Woodhouse 2006). The permittivity of dry snow is determined by density (Drinkwater 1989); the real and imaginary dielectric constant of wet snow increase due to LWC (Tiuri et al. 1984). ε'' increases as LWC increases causing a decrease in penetration depth (Figure 2.11, Left) due to absorption, transmission, and scattering loss (Figure 2.11, Right) (Ulaby et al. 1984).

If scattering losses are ignored penetration depth is given,

$$\delta_p = \frac{\lambda_0}{4\pi}\left\{\left[\left(1+\left(\frac{\varepsilon''}{\varepsilon'}\right)^2\right)^{1/2}-1\right]\frac{\varepsilon'}{2}\right\}^{-1/2} \qquad \textit{Eq. 40}$$

where λ_0 is wavelength, ε' is measured, and ε'' is calculated form wetness (Ulaby et al. 1984), ε''_{wet},

$$\varepsilon''_{wet} = \varepsilon''_w(0.1W_v + 0.8W_V^2) \qquad \textit{Eq. 41}$$

where ε''_w is 36.51 at 5.3 GHz, and W_v is water content (%) (Drinkwater 1989).

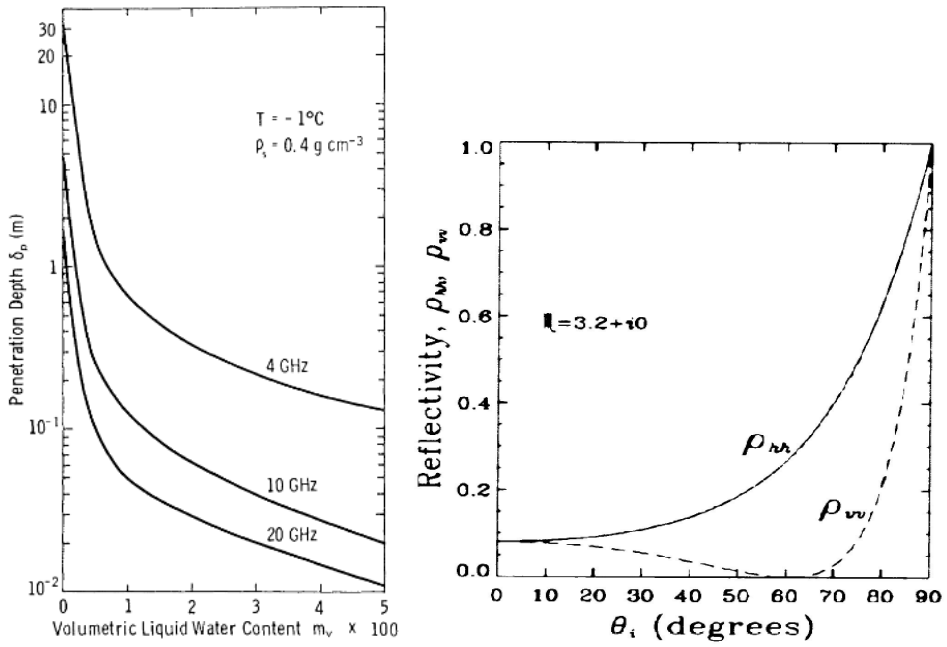

Figure 2.11. Left: Frequency dependent decrease in penetration depth with LWC increase From Ulaby et al. (1984). Right: Reflection as a function of incidence angle. From Woodhouse (2006).

More simply, normalized the radar backscatter coefficient (σ^0) is the frequency dependant power of the received electric wave field, after the emitted electric wave field has interacted with a media. It accounts for the distance to the target and the area of illumination, so that the manipulation of the energy is a function incident angle, and of the physical shape and dielectric properties comprising the target itself. Common incoherence parameters are normalized radar cross-sections including: σ^0_{HH} and σ^0_{VV} (horizontal co-polarization and vertical co-polarization, respectively; *co-pol*) describe targets in a linear polarization and decrease linearly with incidence angle for smooth targets. The linear polarizations over incidence angle are useful in differentiating backscatter response from structure and dielectrics (e.g. Geldsetzer et al. 2007; Fuller et al. 2009). Reciprocity is often enforced for σ^0_{HV}(cross-polarization; *cross-pol*), which is

sensitive to volume scattering within a medium. There are several advantages to active microwave systems in that they have a higher spatial resolution, and generate their own illumination, which is a constant and known quantity. However, these systems are relatively newer (particularly those capable of multiple polarizations) are more expensive and require more power. Validation has been conducted for these systems (e.g. Geldsetzer et al. 2007; Fuller et al. 2009); however, there are currently no major operational snow assimilation schemes (i.e. automated modeling techniques which estimate snow depth/SWE from integrated satellite and available in situ data) employing active microwave remote sensing, snow thermodynamic modeling, and simulated microwave backscatter. However, schemes are in development with regard to snow and ice presence/absence, and the effects of a more complex representation of snow layering on backscatter over first-year sea ice.

2.3 Microwave Emission and Backscatter Modeling

The following section describes several microwave emission and backscatter models including the multilayer adaptation of the Helsinki University of Technology (HUT) model and the Multilayer Snow and Ice Backscatter (MISB) model used in this work.

2.3.1 Multilayered Microwave Emission Models

Contemporary snow microwave emission models are based on the frequency dependent transmission, refraction, reflection, scattering, absorption, and extinction of microwave emissions, as they vary for different snow types and stratigraphic arrangements. The interactions of microwave energy and snow are complicated by the organization of snow particles of varying sizes at spaces smaller than incident micro-wavelengths (*i.e*. snow grains), and by layering

within the snowpack (Tedesco and Kim 2006). The effects of grain-size and layering are considered in models such as the Microwave Emission Model for Layered Snow packs (Matzler and Wiesmann 1999; Wiesmann and Matzler 1999), Dense Media Radiative Transfer theory based on Quasicrystalline Approximation (Liang et al. 2008), and the more recently developed multiple-layer Helsinki University of Technology snow emission model (Lemmetyinen et al. 2010). Combinations of empirical and theoretical components were developed to create more robust semi empirical and theoretical models. The goal of these models is the automated or semi-automated inversion of snow properties such as SWE, for hydrological and climatological applications, at varying temporal and spatial scales.

2.3.1.1 Microwave Emission Model for Layered Snow packs (MEMLS)

The Microwave Emission Model of Layered Snowpacks is a semi-empirical model for frequencies between 5 GHz and 100 GHz developed by Wiesmann and Matzler (1999) (Figure 2.12). MEMLS employs a six-flux theory of coherent and incoherent radiative transfer between layers; the model accounts for snow-grain and layer driven scattering and absorption within the snowpack in three dimensions (six directions), and considers total internal reflection. After the six-flux radiative transfer is applied, the model is reduced to a more simple up- and down-welling radiation scheme (Wiesmann and Matzler 1999). The components of the model are absorption, permittivity, refraction, and reflection coefficients, each based on physical models and measured dielectrics of the snowpack, and an empirical scattering coefficient based on measured snow properties. Primary input data includes: density, snow temperature, liquid water content, correlation length (parameterizes grains size), vertical position/thickness of the layer, ground temperature, and snow ground reflectivity. These inputs are used to derive the secondary

model parameters which comprise the individual components of the model. The secondary model parameters are: dry and wet snow dielectrics, and absorption and scattering coefficients.

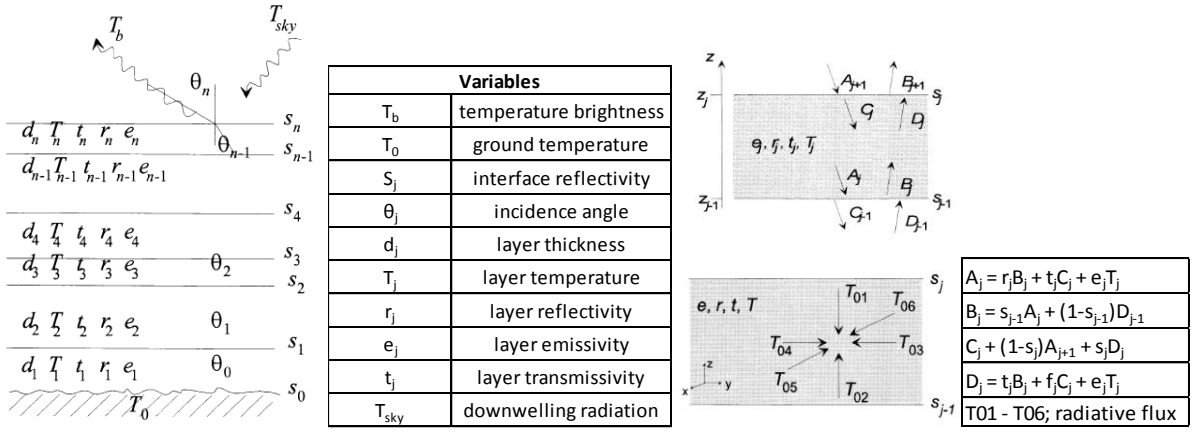

Variables	
T_b	temperature brightness
T_0	ground temperature
S_j	interface reflectivity
θ_j	incidence angle
d_j	layer thickness
T_j	layer temperature
r_j	layer reflectivity
e_j	layer emissivity
t_j	layer transmissivity
T_{sky}	downwelling radiation

$A_j = r_jB_j + t_jC_j + e_jT_j$
$B_j = s_{j-1}A_j + (1-s_{j-1})D_{j-1}$
$C_j + (1-s_j)A_{j+1} + s_jD_j$
$D_j = t_jB_j + f_jC_j + e_jT_j$
T01 - T06; radiative flux

Figure 2.12. Multiple-layer schematic of the MEMLS model (left) and table of variables (right). From Wiesmann and Matzler (1999).

The snowpack is modeled as a stack of horizontal layers, each with values of thickness, correlation length (0.01 mm to 0.3 mm), density, liquid water content, and temperature. The model assumes that the layer interfaces are horizontally planar and employs a spherical snow grain representation (Matzler 1998). The volume scattering component is driven by correlation length; volume scattering is frequency dependent and increases by the correlation length to the power of 2.5 (Matzler and Wiesmann 1999). Matzler (2002) notes the difficulty in comparing snow grain to correlation length for any non-spherical grain shape. This leads to complexities in physical measurement of grain size, with regard to correlation length as an input to the model, in that snow grains have a variety of non-spherical morphologies. This can lead to inaccuracies in model predictions of snow properties (Tedesco and Kim 2006). Application of MEMLS where grain correlation length exceeds 0.3 mm requires a coarse grain approximation (0.35 to 0.71 mm) using the improved Born Approximation (Matzler and Wiesmann 1999), which models Rayleigh

scattering and absorption for isotropically oriented and freely arranged ice particles as oblate spheroids (Matzler 1998).

The model components consider interactions occurring within the layers and at the interfaces of adjacent layers. The six-flux model (2 vertical, 4 horizontal) estimates emission lost due to trapping in the horizontal fluxes (lost in that it is not available for sensing by the radiometer); only vertical fluxes can escape each snow layer or the snowpack at the snow air interface. This reduces to up- and downwelling emission at each layer boundary, allowing 4 components for each layer (2 for the bottom interface and 2 for the top interface). These characterize the emission entering and leaving each interface based on snowpack brightness temperature; ground-snow interface reflectivity and temperature; layer thickness and temperature; and internal reflectivity, transmissivity, emissivity, scattering, and absorption. Multiple reflections are considered and a damping coefficient is applied to account for a reduction in emission through scattering due to repeated passing through a snow layer. The internal scattering phase is considered, given the two-flux model, and both coherent and incoherent phase interactions are calculated, assuming an isotropic scattering function.

The reflectivity at layer boundaries is considered using the Fresnel reflection coefficient for layers thinner than ~ ½ wavelength. If the phase is coherent, the effect of the layer is used for calculations of the two adjacent layers; the coherent layer is then removed from the input of the model, as scattering and absorption are negligible for layers thinner than ~ ½ wavelength. In addition to refraction and reflection effects, changes in emission propagation direction and polarization occur due to volume scattering. The change in emission incidence angle, from the point of view of the radiometer, is considered and weighted according to transmissivity; again,

emission subject to total internal reflection is considered and the loss accounted for. Subsequently, changes in effective polarization are modeled through polarization mixing formula, which account for the difference between horizontal and vertical polarization due to volume scattering.

2.3.1.2 Dense Media Radiative Transfer theory based on Quasicrystalline Approximation (DMRT/QCA)

The multi-layered Dense Media Radiative Transfer theory based on Quasicrystalline Approximation (DMRT/QCA) model employs a Mie scattering component to simulate brightness temperature for natural snowpacks (Figure 2.13). The inputs to the model are particle size, volume fraction, and temperature (Liang et al. 2008). DMRT characterizes propagation and scattering by particles through a pair distribution function dependent upon particle size and volume fraction and coherent interactions; the Quasicrystalline Approximation is based on the assumption that scattering within the snowpack is not caused by single snow grains acting independently (Tsang et al. 2000). DMRT/QCA with sticky particles, considers spherical snow grains as poly-aggregate clusters of crystals, where there is more than one crystal within the distance of an incident wavelength (Liang et al. 2008). When compared with independent scattering theory, which considers Raleigh interactions, the polyaggregate nature of DMRT/QCA considers Mie scattering, which creates differences in extinction, reflection, and scattering coefficients.

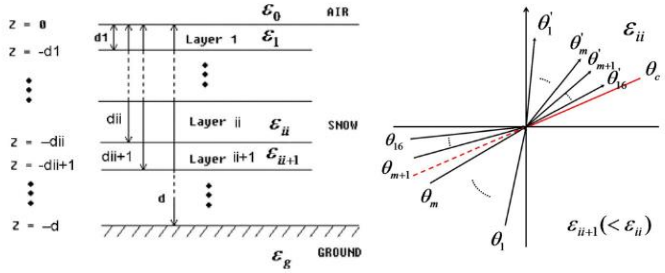

Figure 2.13. DMRT/QCA schematic for a layered medium (left) and the 16 quadrature angle radiative transfer consideration within an individual layer. From Liang et al. (2008).

The multiple-layer model (Liang et al. 2008) builds upon seminal work by Tsang (1987), and calculates radiative scattering for 16 angular paths for each layer. The propagation and extinction coefficients follow Lorentz-Lorenz law (refraction) and the Ewald-Oseen extinction theorem (Tedesco and Kim 2006) based on the Quasicrystalline approximation of the distribution of particles within the media (Tsang et al. 2000). The QCA or "sticky" component of the model, which determines the poly-aggregate nature of the crystals, is set to 0.1 as this value corresponded to a scattering coefficient frequency dependence power of 2.8 (Liang et al. 2008). The value was chosen as it agreed with experimental values conducted by Hallikainen et al. (1987), and no analysis has been conducted on variations to the "sticky" component. The volume scattering and attenuation is modeled through consideration of wave interaction with paired particle spacing (near, intermediate, far) for every particle in the layer, and weighted by pair distribution function; therefore, all possible ranges of scattering interactions are considered (Wen et al. 1990). The radiative transfer between layers is calculated for each of the 16 fluxes according to Snell's law. Through these components, the model includes total internal reflection, refraction, and absorption, for coherent and incoherent radiative transfer for the 16 quadrature angles at layer interfaces, and volume scattering and absorption within the layers.

2.3.1.3 Multiple-layer Helsinki University of Technology snow emission model (HUT)

The original Helsinki University of Technology (HUT) Snow Microwave Emission Model is a semi-empirical physically-based model of microwave emission from a homogeneous snow cover using radiative transfer theory (Pulliainen and Hallikainen 1998) (Figure 2.14). The snow extinction coefficient is an empirical formulation; the soil, forest, and atmospheric representations are semi-empirical formulations. A basic assumption of the HUT model is that scattering is concentrated in the forward direction. The HUT model considers only forward scattering and incoherent emission; therefore, ignoring the effects of superposition and total internal reflection. The forward scattering intensity was empirically determined, and is fixed for all frequencies at a fraction value of 0.96. The snow component presumes emission beginning beneath the snow cover, and considers the attenuation and scattering effects of the snow cover on emission, as well as emission from the snow cover itself. The scattering and extinction coefficients are a function of grain size and dielectrics. The input parameters of the HUT model are snow depth, density, effective grain size, and temperature; sub-surface temperature, dielectric constant and effective RMS height; and near-surface air temperature dependent atmospheric emission and transmissivity contributions.

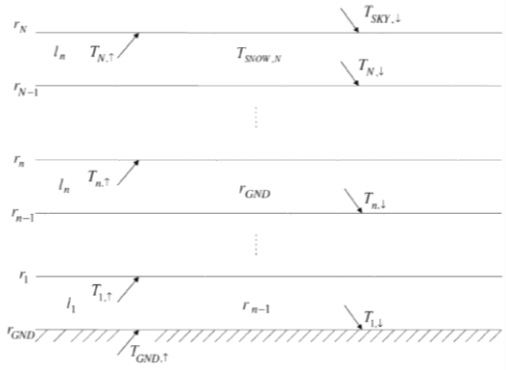

Figure 2.14. Multiple-layer schematic of the HUT model. From Lemmetyinen et al. (2010).

The multiple-layer adaptation of the Helsinki University of Technology snow emission model is a semi-empirical model for frequencies between 5 GHz and 90 GHz developed by Lemmetyinen et al. (2010). The multiple-layer adaptation of the HUT model allows for the parameterization of multiple snow and ice layers each with varying physical properties. The multiple-layer modification is a two-flux (up- and downwelling) approximation of each layer, with Lambertian interfaces between layers and at the snow-air interface. The transmission at layer interfaces is represented by Fresnel coefficients, with reflection represented by a loss factor determined by attenuation through absorption, scattering, and extinction formulae. Each layer consists of an internal upwelling and downwelling component, an upwelling component from the layer below, and a downwelling component reflected from layer above, and reflections of up- and downwelling emissions at the upper and lower interfaces of the layer. The summation of the layered upwelling emission at the snow-air interface gives the emission leaving the snowpack.

The HUT model applies the delta-Eddington (two-stream) approximation to the radiative transfer equation for a single, homogeneous layer of snow (Pulliainen et al. 1999; Lemmetyinen et al. 2010),

$$T_{SNOW} = T_0 \frac{K_a}{K_e - qK_s}\left(1 - \frac{1}{L}\right) \quad \textit{Eq. 42}$$

$$T_{SNOW} = T_{phys} \frac{K_a}{K_e - qK_s}(1 - \exp((-K_e + qK_s) \cdot d_0 \cdot \sec\theta)) \quad \textit{Eq. 43}$$

where T_{phys} is physical temperature, *1/L* is attenuation, K_a is absorption defined by the complex dielectric constant for dry snow with densities (ρ) up to 0.4 g/cm^3 (Matzler 1987),

$$\epsilon' = 1 + \frac{1.60\rho}{1 - 0.35\rho} \quad \textit{Eq. 44}$$

$$\epsilon'' = \epsilon''_{ice}[0.52\,\rho + 0.62\,\rho^2] \quad \textit{Eq. 45}$$

K_e is the extinction coefficient determined by the empirical equation,

$$K_e = 0.0018\, f^{2.8}\, D_{OBS}^2 \quad \textit{Eq. 46}$$

q is a frequency dependent constant (11 GHz - 96 GHz: q = 0.96) defining incoherent forward scattering in a snow pack, K_s is a microwave scattering coefficient from Wiesmann et al. (1998), d_0 is the snow thickness, and θ is the incidence angle.

The multiple-layer HUT model is limited to considering Lambertian, incoherent radiative transfer between layers with emission within layers defined as (Lemmetyinen et al. 2010),

$$T_{n,\uparrow} = S_n\,(T_{SNOW,n} + T_{n+1\downarrow}\frac{t_n \cdot r_{n-1}}{l_n^2} + T_{n-1\uparrow}\frac{t_{n-1}}{l_n} + T_{SNOW,n}\frac{r_{n-1}}{l_n}) \quad \textit{Eq. 47}$$

$$T_{n,\downarrow} = S_n \left(T_{SNOW,n} + T_{n+1\downarrow} \frac{t_n \cdot r_{n-1}}{l_n^2} + T_{n-1\uparrow} \frac{t_{n-1}}{l_n} + T_{SNOW,n} \frac{r_{n-1}}{l_n}\right) \quad \textit{Eq. 48}$$

employing the Fresnel transmission (*t*) and reflection (*r*) coefficients and loss factor (*l*) for layer (*n*). The terms in brackets are the internal upwelling emission($T_{SNOW,n}$), internal down welling emission from layer *n+1* ($T_{n+1\downarrow} \frac{t_n \cdot r_{n-1}}{l_n^2}$), upwelling emission reflected from the layer *n-1* ($T_{n-1\uparrow} \frac{t_{n-1}}{l_n}$), and internal down welling emission from *r-1* $T_{SNOW,n} \frac{r_{n-1}}{l_n}$. S_n represents multiple reflections in layer *n*,

$$S_n = \frac{1}{1 - r_n \; r_n - 1/l_n^2} \quad \textit{Eq. 49}$$

Ice layers, or lenses, are represented by,

$$T_{ICE} = T_{phys} \left(1 - \exp((-K_a) \cdot d_0 \cdot sec\theta)\right) \cdot \quad \textit{Eq. 50}$$

assuming a non-absorbing and non-scattering layer of pure ice.

As previously noted, the model is driven by snow grain size, employing an empirical formula to derive effective grain size from observed grain size,

$$D_{eff} = 1.5 \cdot (1 - \exp(-1.5 \cdot D_{obs})) \cdot \quad \textit{Eq. 51}$$

where D_{obs} is the mean of maximum diameters of snow grains per layer, weighted by the thickness of the layer in the snowpack. The HUT model was chosen for this work as it is the only emission model currently used in operational SWE retrievals (ESA GlobSnow).

2.3.2 Multilayered Microwave Backscatter Modeling

Contemporary snow microwave backscatter models are based on the frequency dependent transmission, refraction, reflection, scattering, absorption, and extinction of microwave backscatter, as they vary for different snow and sea ice conditions, and stratigraphic arrangements. Microwave simulations of based on Strong Fluctuation Theory (STF) (e.g. Jin1984) was applied to snow on sea ice by Barber et al. (1997), and showed good agreement with volume scattering observations at 10 and 37 GHz; however, SFT did not accurately simulate surface scattering interactions. Therefore, simulations based on Radiative Transfer Theory was selected for this work, as layering and potential surface scattering interactions need to be investigated when considering the layered nature of snow, and the interfaces between layers. The lineage of models with pertinence to this work (Multilayered Snow and Ice Backscatter, MSIB) model have a foundation in the methods of Kim et al. (1984) and Ulaby et al. (1984). Surface scattering is modeled using the Kirchoff physical optics method, appropriate for smooth surfaces that can be described by a Gaussian distribution function (Rees 2006). Volume scattering is modeled based on the number density and effective size of ice-particles in each layer (Drinkwater 1989). A two-way loss factor is used to account for reductions in both incoming and outgoing scattering power (Winebrenner et al. 1992; Kendra et al. 1998).

The model considers scattering at the snow-air interface, within the snow volume, at the snow-ice interface, and within the ice volume, and takes into account the effects of brine in the ice and brine-wetted snow on dielectric properties (Barber and LeDrew 1994; Geldsetzer et al. 2009). The Kirchoff physical optics model gives scattering as a function of the dielectric properties and incident angle, for a moderately rough surface (Rees 2006),

$$\sigma^0_{HH}(\theta) = \sigma^0_{VV}(\theta) = \frac{|R(0)|^2 \exp(-\left(\frac{tan^2\theta}{2\sigma_m^2}\right))}{2\sigma_m^2\, cos^4\theta} \qquad \textit{Eq. 52}$$

where R(0) is the Fresnel reflection coefficient as a function of dielectric properties (recall *Eq. 36* and *Eq. 37, Section 2.2.3*), θ is the incident angle, and σ_m is the surface roughness.

The volume scattering component is a function of the number density and effective particle size comprising the media. Volume scattering is given by (Rees 2006),

$$\sigma^0(\theta) = |R(\theta)|^4 \frac{\sigma_V\, cos\theta'}{\gamma}\left(1 - \frac{1}{L^2(\theta')}\right) + |R(\theta)|^4 \frac{\sigma_g^0(\theta')}{L^2(\theta')} \qquad \textit{Eq. 53}$$

where σ_v is the volume scattering coefficient, which can be expressed as half the scattering coefficient, and L is the attenuation coefficient.

2.3.2.1 Multilayered Snow and Ice Backscatter (MSIB) Model

The multilayer snow and ice backscatter model is used to calculate the co-polarized backscattering coefficient (dB) in both vertical (σ^0_{VV}) and horizontal polarization (σ^0_{HH}), by taking into account the surface scattering contributions and transmission of each snow or ice layer interface, and the volume scattering contributions, absorption, and refraction within each snow or ice layer. Total backscatter for the snow-covered sea ice is calculated based on the combined contributions of as many snow and ice layers as are present. Model inputs for each layer are: thickness (cm), density (g cm^{-3}), temperature (°C), salinity (ppt), grain size (m), root-mean square height surface roughness (RMS, mm), correlation length (LC, mm), dielectric permittivity (e′), and dielectric loss (e″); the model is also capable of semi-physical dielectric

mixture modeling (e′ and e″) to account for brine volume interactions, as described in Geldsetzer et al. (2009) and Scharien et al. (2010).

2.3.3 Challenges to Microwave Emission and Backscatter Modeling

There are several challenges to the current understanding of snow microwave emission and backscatter modeling including parameterization of grains, polyaggregate crystals, composition of the individual layers, the determination of individual layers, the order of multiple snow layers, liquid water content, snow water equivalent values, and the complexity of the models themselves with regard to inversion of desirable snow properties from a single brightness temperature or backscatter value.

2.3.3.1 Snow Grain Size

Of primary concern when dealing with microwave interaction through snow is snow grain size. Natural snow cover is often complexly arranged, with a variety of snow grain sizes, which may bond to form clusters of grains or polyaggregate crystals. As individual and collective crystal sizes increase, approaching the wavelength of the emitted energy, Mie scattering occurs. Additional confusion with regard to grain size arises from problems associated with model parameterization of the grain size. For example, physical measurement can note the long and short axis and rounded or cupped shape of the grains; however, models parameterize grains as oblate or spheroid, citing weak shape dependence. The weak shape dependence has been contradicted by others that relate shape to dielectric properties, and therefore attenuation in microwave models (Colbeck 1982). Measurement of the spatial arrangement of the grains (for

example the distances between grains or scattering centers) may employed by through a correlation length variable; however, this is also difficult to measure (Matzler 2002). Various models relate scattering and extinction to frequency by powers ranging from 2.5 to 4; however, the power of the scattering frequency dependence affects the amount of scattering occurring and the extinction length. Given the confusion of grain parameterization and scattering and extinction coefficients, inversion from brightness temperature or backscatter values is complex.

2.3.3.2 Snow Layering

The layers, crusts, and ice lenses occurring in snowpacks can be discontinuous, with high spatial variation in both distribution and quality. The presence, position, and order of snow layers or crusts affects the evolution of snow properties both above and below the layer due to due to modification of the temperature gradient through the snowpack. Ice lenses and crusts also tend to trap and redirect liquid water present in the snowpack thereby potentially enhancing absorption of emission and backscatter, while also adding complexity to the structure of the ice lens through melt and refreeze processes. The simplification of the complex grain bonding, dielectric variations, scattering, reflection, refraction, extinction, and absorption that occurs at layer boundaries requires judicious and sometimes subjective choices in parameterization. Additional ambiguity arises when attempting to objectively consider what constitutes a snow or ice layer or crust.

The inclusion of various snow types and ice crusts in models adds complexity to modeling and emission interpretation. The frequency dependent emission integrates differently for multiple layers, when compared to single layers, through inclusion of the reflection, refraction, scattering,

extinction, and absorption of microwaves at layer interfaces (Liang et al. 2008). Interfaces between snow layers, crusts, and ice lenses that naturally occur in snowpacks are generally characterized in radiative models as Lambertian surfaces and employ Fresnel reflection coefficients to determine the reflection and transmission of radiation. Lenses and crusts tend to reflect and scatter horizontally polarized microwave energy preferentially over vertically polarized microwave radiation. More study of the characterization of the complex boundary interactions on microwave energy is required, to determine the role of the order and complexity of layering for depth hoar, windslab, fresh snow, crusts, and ice lenses on microwave emission and backscatter.

Snow cover stratigraphy varies seasonally, in both the types and the sequence of layers. The stratigraphy of snowpacks affect snow cover characteristics as the snow pack matures over the course of a season through thermodynamic processes (Colbeck and Jamieson 2001). The sequence and composition of layers in snow affects grain size, density, and permittivity (Colbeck 1982; Colbeck and Jamieson 2001), and therefore the derivation of snow water equivalent and snow depth, through scattering, reflection, and absorption of microwaves. The overall response microwave energy to snow cover is, therefore, not simply the averaging of snow properties, but lies in the properties of each layer and the sequence of the layers themselves (Colbeck 1991). The frequency dependence of microwave energy on extinction, scattering, and reflection cause integration of the snow pack stratigraphy over a greater depth for lower frequencies and over a shallower depth for higher frequencies. Models which rely on differences or ratios of multiple frequencies, and relatively linear relationships between snow water equivalent or snow depth and emitted intensity, may encounter additional error when modeling complexly layered snow packs,

as layer constituents may affect frequencies in a non-linear fashion. Preferential reflection and refraction of horizontally polarized microwaves at layer interfaces within the snowpack, cause a decrease in horizontally polarized microwave energy, when compared to vertically polarized microwave energy (Liang et al. 2008), which may be exploited to lend insight into the number and quality of layers present in a snow pack.

2.3.3.3 Layering and Model Complexity

The more complex a microwave model becomes, the more difficult the inversion for snow parameterization. When relying on satellite data, a single temperature brightness or backscatter value is often the only output to characterize snow condition over pixels that often include complexly varied terrain. Added confusion stems from the many-to-one issue (Durand and Margulis 2007), whereby a single brightness temperature or backscatter value that can represent two or more snow conditions (Barber and LeDrew 1994; Derksen, LeDrew, Walker et al. 2000, Barber et al. 2009). As models become more complex in order to better characterize the intricacies of microwave interactions with snow, the inversion of that process for snow parameterization becomes dependent upon an increasing number of variables, processes, and interactions that must be characterized from a single brightness temperature or backscatter value.

2.3.3.4 Brine

Specific to snow cover on sea ice, the effect of brine on dielectric properties with regard to microwave energy interactions, adds complexity to microwave modeling through variability in surface and volume scattering mechanisms (Barber and LeDrew 1994; Barber et al. 1994). Brine supresses the freezing point of water, and thus impacts dielectrics (Barber et al. 1995; Geldsetzer et al. 2009). The dielectric mismatch due to brine at the snow-ice interface, reduces penetration

depth and causes specular surface scattering away (for smooth surfaces) from the scatterometer, resulting in less backscatter. However, the brine wetting of large (depth hoar) snow grains in the lower layers of the snow pack, create gradients of dielectric permittivity and loss, decreasing penetration depth through the snow, which may mask specular reflectance from the snow–ice interface and increase volume scattering. The capillary action governing brine is thought to resemble that of water wetting (Geldsetzer et al. 2009); therefore, brine wicking to the interstices of snow grains depends upon contact angle, surface tension, snow grain shape, and snow porosity (Colbeck 1974). The volume of brine varies temporally, spatially, and seasonally. Additionally, the uneven wicking of brine may result in a dielectrically rough surface, which is difficult to measure and impacts the frequency-dependant surface roughness parameterization in microwave models.

2.4 A Snow Water Equivalent Retrieval Scheme and Snow Numerical and Thermodynamic Modeling

The section reviews the GlobSnow SWE retrieval scheme pertinent to this work. It then briefly reviews the history of development of key components to state of the art thermodynamic models. It then describes the SNTHERM thermodynamic snow model used in this work.

2.4.1 GlobSnow SWE Assimilation Scheme

A SWE retrieval scheme based on the single-layer HUT model developed by Pulliainen (2006) is currently employed by the European Space Agency GlobSnow project (www.globsnow.info) for operational snow water equivalent retrieval (Figure 2.15). It is a spatial application of the single-layer HUT model, on a hemispheric scale, that employs atmospheric and vegetation (forest

biomass) emission models, and assimilates ground based physical snow depth and grain size data and space-borne radiometer data, for inversion of SWE. The advantage of this method is that the model output includes statistical error variance estimates for each 25 x 25 km pixel with SWE estimates. Modifications of the HUT model have been used to assess application for various landcover classes (Kontu and Pulliainen 2010; Rees et al. 2010; Gunn et al. 2011; Takala et al. 2011; Derksen et al. 2012).

Snow depth observations from weather stations are spatially interpolated using kriging to provide *observed SD* values; an exponential autocorrelation function of the spatial variability is calculated (Takala et al. 2011). Mountainous regions and the deepest 1.5% of depth measurements are removed to avoid anomalies. The *observed SD* data are input to a single-layer HUT model giving snow depth, density, and average grain size; forest biomass (stem volume) emissions and atmospheric emissions are accounted for in respective sub-models (Pulliainen et al. 1999).

The modeled HUT T_B is then fit to satellite T_B at the locations of the surface-based measurements and optimized for grain size (i.e. HUT modeled T_B is fit to the satellite measured T_B by adjusting the effective grain size variable),

$$\min_{do}\{(T_{B,19V,mod}(d_O, D_{ref}) - T_{B,37V,mod}(d_O, D_{ref})) - T_{B,19V,obs} - T_{B,37V,obs}\} \qquad Eq.\ 54$$

where d_O is grain size, D_{ref} is snow depth, with subscript V referring to vertically polarized T_B at 19 and 37 GHz, and the *mod* and *obs* referring to the modeled and observed values, respectively. Snow density is fixed at 0.24 g cm^{-3}. Final estimated snow grain size (and standard deviation) is determined by averaging values from regional stations (the grain size is set to a minimum of 0.2

mm, smaller grains are rounded up). A surface of effective snow grain size, and variance, is then interpolated using kriging based on effective snow grain values at the surface-based measurement locations.

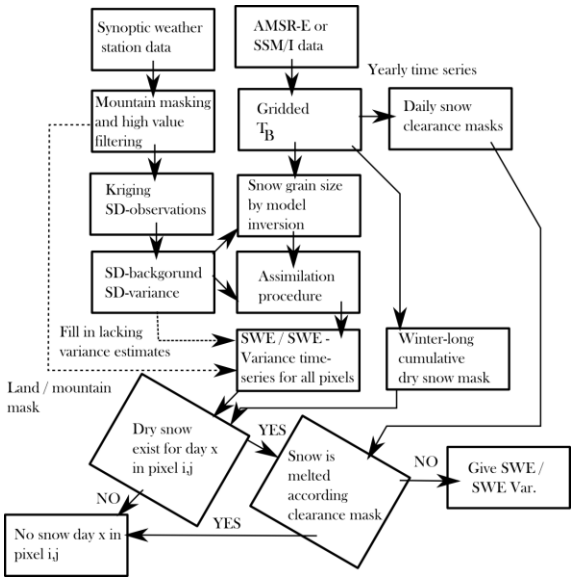

Figure 2.15. The SWE retrieval algorithm developed by Pulliainen (2006) and employed by the GlobSnow project.

A spatially continuous surface of *radiometer SWE* values is produced using the HUT model employing the effective grain size, and landcover information. The simulated values are compared to spaceborne radiometer measurements at the pixel scale. The estimates are tuned to observations by modifying the SWE. The interpolated effective grain size (with variance from kriging) is used in the cost function to constrain grain size in the SWE estimation.

The assimilation for each pixel is then performed by weighting the *radiometer SWE* and the *observed SD*, providing a final estimate of SWE with statistical uncertainty; the variance adjusts the weighting of *radiometer SWE* and *observed SD*,

$$min_{D_t}\left\{\left(\frac{\left(T_{B,19V,mod}(D_t)-T_{B,37V,mod}(D_t)\right)-\left(T_{B,19V,obs}(D_t)-T_{B,37V,obs}(D_t)\right)}{\sigma_t}\right)+\left(\frac{D_t-\widehat{D}_{ref,t}}{\lambda_{D,ref,t}}\right)^2\right\} \quad Eq.\ 55$$

where $\widehat{D}_{ref,t}$ is the snow depth estimate from kriging for the day under consideration (t), $\lambda_{D,ref,t}$ is the estimate of standard deviation from the kriging interpolation, and D_t is the snow depth.

A dry snow mask is necessary to control the effects of wet snow, and a snow clearance date is also employed. If a grid cell has never been estimated to have dry snow, it is labeled as having no snow. If the snow clearance estimation determines the pixel to be snow free, it is labeled as having no snow. In the case that a pixel has snow according to the snow clearance date estimation, and the pixel is included in the dry snow mask, SWE is estimated for that cell and variance of the estimate is given.

More simply, the assimilation method developed by Pulliainen (2006) weights SWE, estimated by fitting a single-layer HUT radiative to remotely sensed microwave emission data coupled with available in-situ SWE measurements, by their respective statistical uncertainties. This retrieval method is operationally employed in the European Space Agency's Globsnow project and has recently been used produce a long term climate record (Takala et al. 2011). The 3 stage process begins with an optimization to determine an effective grain size. The single-layer HUT model is used with snow depth (SD) observations from weather stations and a fixed density (0.24 g cm^{-3}), to fit modeled TB to observed satellite TB at 19V and 37V GHz (Pulliainen and Hallikainen 2001). This initial accuracy of effective grain size is essential to optimization and assimilation performance (Pulliainen 2006), as it includes error in the relationship between the HUT model and radiometer TB (i.e. vertical integration of snow grain size and stratigraphic

layering, scattering saturation), in landcover TB contribution (e.g. forest stem volume), and in snow density (fixed at 0.24 g cm^{-3}) (Pulliainen 2006; Takala et al. 2011). The second stage of the assimilation is a synoptic estimation of grain size, and its standard deviation, is achieved through Kriging interpolation from weather station SWE observations (SWE = SD · density). This produces a continuous surface of grain size values, and variance for any pixel/grid location. The final stage estimates SWE using respective statistical uncertainties to weight the simulated or ground observed SWE estimates (this component also considers temporal changes in SWE, weighted by its standard deviation, to regulate the magnitude of day-to-day change in SWE by taking into account previous retrievals). Thus, increased distance from station observations (or time from previous retrievals) decreases weight on those observations, giving relatively more weight to the modeled SWE retrievals. This is of particular importance with regard to large swaths of the sub-Arctic which rely on relatively few observation points and which contain extreme heterogeneity of snow properties (Pulliainen 2006; Takala et al. 2011). The assimilation technique considers the non-linear sensitivity of TB to SWE, and reduces contribution from components adaptively with statistically inaccuracy (Pulliainen 2006). Use of this assimilation technique has resulted in RMSE values of 15 mm to 40 mm SWE, and has reduced systematic error when compared to direct TB inversion as saturation occurs when SWE $\gtrsim$ 130 mm, and when compared to interpolation of synoptic station observations (Pulliainen 2006; Takala et al. 2011).

2.4.2 A review of the development of key components to state of the art thermodynamic models

2.4.2.1 Albedo

Initial surface energy balance models considered incoming and outgoing radiation as a function of albedo and latitude, ignoring important associated feedbacks. Dunkle and Bevans (1956) parameterized albedo using a simple two-stream flux of incident diffuse radiation; however, the parameterization of multiple scattering and absorption within the snow pack was insufficient, and the authors note lack of consideration of direct radiation as a weakness of the model. Choudhury and Chang (1979) followed this work with a two-stream model employing the Schuster-Schwartzschild approximation (isotropic forward and backscattering) for a single scattering ($0.6\ \mu m < \lambda < 2\ \mu m$), requiring grain size as an input (0.2 mm to 1 mm) and backscattering coefficient of 7.5%. The authors note good agreement between modeled and measured results, and difficulty determining the effects of direct and diffuse radiation. Giddings and LaChapelle (1961) developed a random walk model of diffusion that demonstrated good agreement for albedo greater than 80%, but poor model performance for less than 60%; Wiscombe and Warren (1980) noted that this work did not resolve the confusion surrounding the diffuse and direct components of incident radiation. These works assumed, incorrectly, that albedo was a result of reflection from grains, and not refraction through them, and considered only diffuse isotropic scattering. This lead to problems representing direct radiation effects associated with Sun zenith angle, and the necessity for tuning parameters to fill gaps in understanding, and achieve agreeable results.

A refraction based model (Bohren and Barkstrom 1974) employed geometrical optics for a single spherical grain interaction and radiative transfer theory for extrapolation to snowpacks, capturing

the strong forward scattering component. This work found good agreement between model and measurement of albedo (±2%) and noted extinction as proportional to density and inversely proportional to the square-root of grain size; and diffusely illuminated albedo as density independent and proportional to the square root of grain size. This work was expanded to larger grain sizes and the infrared portion of the spectrum by Berger (1979), and was used to calculate snow emissivity. These works introduced refraction based scattering, and radiative transfer theory, which negated the need for variable tuning to achieve agreeable results; however, separate models were required to parameterize frequency dependent absorption for small and large optics (Wiscombe and Warren 1980).

Wiscombe and Warren (1980) employed a Mie scattering model ($0.3\ \mu m < \lambda < 5\ \mu m$) with a delta-Eddington approximation to account for multiple forward scattering interactions, in order to parameterize albedo as a function of effective snow grain size (50 μm to 1 mm), which represented the optical properties of actual grains using spherical particles. They recognized the necessity of the modeling of albedo for understanding of feedback mechanisms in future climate models. Additional input variables included solar zenith angle and the ratio of direct and diffuse incident radiation. This allowed calculation of albedo for the entire solar spectrum ($0.3\ \mu m < \lambda < 5\ \mu m$) for diffuse or direct radiation at any zenith angle. Absorption is based on the frequency dependent absorption of ice with regard to visible and near-infrared parts of the spectrum. Complete model parameterization as a semi-infinite layer, required snow depth, density, and grain size. The model overestimated albedo in the visible part of the spectrum; the authors attributed this to the effect of impurities in the measured snow. Marshall and Warren (1987)

developed a simplified spectrally-averaged 2 part albedo (0.3 to 0.7 um, 0.7 to 3.0 um) to increase computational efficiency for thermodynamic modeling.

2.4.2.2 Thermal conductivity of snow and sea ice

2.4.2.3 Snow

Sturm et al. (1997) provide a review of snow conductivity data collected in various studies originating in 1886, which primarily associated thermal conductivity with snow density. Several methods for data collection and derivations have been employed, each with limitations and advantages, with primary concern centering about external radiative inputs and the long duration of the sampling allowing for structural metamorphosis and temperature variation. Radiation and convection were not considered in this work as heat is transported at rates several orders of magnitude less than the aforementioned. The authors note 3 pathways for heat conduction in snow: the ice lattice, air pore spaces, and vapor transport associated with latent heat from sublimation and condensation. Sturm et al. (1997) employ a steady state heat flow method, which addresses concerns with a short sampling time and the ability to sample with little contamination in natural snow covers. As a result, several heat conduction pathways are noted and models are provided based on density, temperature, and snow type, the later as a proxy for vapor flux and degree of bonding. Density ($R^2 = 0.79$) as a quadratic function,

$$k_{eff} = 0.138 - 1.01\rho + 3.233\rho^2 \quad \{0.156 \leq \rho \leq 0.6\} \qquad \textit{Eq. 56}$$

$$k_{eff} = 0.0230 + 0.234\rho \quad \{\rho < 0.156\} \qquad \textit{Eq. 57}$$

where ρ is density (g cm^{-3}) and k_{eff} is in W m^{-2} K^{-1}. This interpolates to agreeable values with regard to the density of ice; however, the interpolation of zero density is not reasonable even though it falls within 95% confidence. The authors note that the conductivity of snow as a function of density employing a logarithmic relationship ($R^2 = 0.76$) better meets requirements of a best linear unbiased estimate,

$$log_{10}(k_{eff}) = 2.650\rho - 1.704 \quad \{\rho \leq 0.6\} \qquad \textit{Eq. 58}$$

however, large inaccuracies arise when this relationship is extrapolated to the density of ice. Sturm et al. (1997) propose a maximum likelihood estimation,

$$k_{MLE} = 10^{(2.650\rho - 1.652)} \quad \{\rho \leq 0.6\} \qquad \textit{Eq. 59}$$

which also displays large inaccuracies when extrapolated to the density of ice (more than twice the measured value). A fit of thermal conductivity as a function of density and varying snow types is provided, with the authors indicating that the relationship to density is actually a relationship to the degree of vapor flux and bonding between grains. Finally, the authors note a temperature bias for thermal conductivity based on vapor transport. This model didn't take into account the effects of liquid water or brine as would be the case in warm and/or sea-ice based snow packs, which have significant impact on conductivity; however, brine mixture models have more recently been developed for snow over sea ice (Geldsetzer et al. 2009). The need for a series of models to encompass the breadth of conductivity over various physical properties suggests that there are properties, perhaps un-measureable, that are responsible for inaccuracies (Arons and Colbeck 1995); however, the density and bond strength relationships are reasonable

approximations. For wet snow the conductivity of liquid water, the nature of its distribution, and shape of water inclusions, must be also be considered. Parameterizations of snow in climate models have tended to use fixed values, which limits important dynamic inputs of snow.

2.4.2.4 Sea Ice

The thermal conductivity and capacity of sea ice is affected by brine pockets and their distribution. As ice cools and warms, brine pockets change size and salinity concentration through freezing and melting the walls of the pocket, in order to maintain a thermal equilibrium. Models for sea ice thermodynamic conductivity must include the latent heat exchanges and a subsequent decreased heat capacity of sea ice due to brine activity. Bitz and Lipscomb (1999) review of sea ice thermodynamics note that classic models (Maykut and Untersteiner 1971; Ebert and Curry 1993) do not make adjustments in required energy input to account for ice proportions already ablated through internal brine melting. Additionally, assumptions of linear temperature gradients through sea ice result in unrealistic growth rates (Maykut 1986). Thus, failure of classic models occurs as a result of the overestimation of the density of sea ice and the associated energy required for melting, particularly when ice is already close to melting temperature. For these reasons Bitz and Lipscomb (1999) argue that thermodynamic models of sea ice should account for heat capacity and energy of melting, both of which differ greatly from that of pure ice, and therefore the models do not conserve energy. Energy conservation can act as a constraint for ablation, ensuring that energy balance is maintained for application in larger climate models. The model proposed by Bitz and Lipscomb (1999) parameterize drained brine pockets as filled with water, not air, which results in an underestimation of the rate of cooling, but conserves energy with regard to the amount of unmelted ice. The consideration of brine pockets, and their non-

linear distribution within the ice, is necessary to more accurately parameterise sea ice-energy interactions. Energy conservation is important with regard to inputs to larger coupled atmosphere-ice-ocean models; results of the aforementioned work indicate that the energy conservation model improves ice sensitivity to changes in albedo estimations, and in ice growth and ablation estimates over previous non-conserving models. The effects of oceanic inputs to the water exposed portions of sea ice are not well parameterised, as fixed values (~2 W m^{-2}) are generally used; however, variations (up to ~15 W m^{-2}) occur (Lecomte et al. 2011).

2.4.2.5 Cloud radiative forcing

Zhang et al. (1996) provide a review of the impact of clouds on surface radiative fluxes, and note that complex interactions between clouds, snow, and ice have large and rapid effects on long and shortwave radiation, which has an impact on snow melt in the Arctic. Classic models indicate that radiative forcing plays an important role on the timing of spring melt through changes in net surface radiation; however, the effects of those changes were contradictory citing both warming and cooling (Ambach and Denoth 1980; Maykut 1986; Robinson et al. 1992). Hanson (1961) measured a twofold increase in net radiation over sea ice on cloudy days when compared to clear days; these results were confirmed by Ambach (1974) with measurement of an almost threefold increase. As previously noted, clouds reduce incident solar radiation and increase long and shortwave radiation through re-radiance and reflection, respectively. The increased warming through a greenhouse effect more than offsets cooling though shortwave radiation reflected to space at the top of the cloud; the condition and height of the clouds, govern the magnitude of the increase (Zhang et al. 1996). Clear breaks often result in a refreezing of the surface, as the enhancement of radiation by clouds is removed, even though the direct solar radiation is more

intense. Zhang et al. (1996) present a model of surface radiation flux employing a Mie scattering radiative transfer model which includes the effect of clouds, haze, CO_2, H_20, and 0_3. The model determines the cloud forcing for long and shortwave radiation by subtracting the clear sky radiation from cloud covered radiation at the surface; the cloud forcing is then the addition of the long and shortwave components. Cloud character was then parameterized based on liquid water content (g m^{-3}), thickness, optical depth, droplet radius (a function of aerosol content and composition, 4 μm to 11 μm), and liquid water path, with atmospheric vapor content set to 100%. The snow albedo was found using Mie scattering theory and assumed snow radius of 200 μm and density of 350 kg m^{-3}, and sensible and latent heat fluxes were specified. Snow depth was set to 0.35 m and soil parameters were specified below the snowpack. This model included atmospheric characteristics of a 6.5°C lapse rate, and average relative humidity and pressure, and a linear temperature profile; however, Serreze and Barry (2005) note the importance of low level temperature inversions, which affect the aforementioned characteristics. Surface turbulent flux was characterized with 10 m wind speed and relative humidity set to 5 m s^{-1} and 85% respectively. Given the above, the model includes conditions of the general background atmosphere, clouds, turbulent flux, snow, and soil. Results show that longwave cloud forcing increases rapidly but saturates with liquid water path (50 g m^{-2}); the shortwave cloud forcing increases slowly and steadily, even after longwave radiation forcing saturates. Both long and shortwave forcing is sensitive to liquid water path and droplet radius. The absorption and re-radiation of longwave radiation leaves a larger proportion of shortwave radiations at the surface, resulting in a high shortwave albedo (Maykut 1986; Zhang et al. 1996); and cloud emissivity is dependent upon cloud height due to differing cloud characteristics (lower clouds have a warmer base and higher emissivity). Through the above, high, cold, thin cloud cover can delay melt due

to low emissivity, and less re-radiation and multiple reflection, conversely low, warm, thick cloud cover can advance melt due to higher emissivity, and increase absorption, re-radiation, and multiple reflection; the advance or delay is governed by the timing and type of cloud cover in relation to the surface albedo. There are areas of concern for this work as several parameters for important sub-systems (e.g. snow albedo) are simply fixed, and therefore cannot respond dynamically to model perturbations. Also a one-dimensional model does not consider the 3 dimensional nature advection of snow from near-by accumulation zones, of horizontal conduction through leads, and the importance of ice fog/diamond dust on reflection, scattering, and absorption of radiation, which are significant factors when considering atmospheric radiative processes in the Arctic (Serreze and Barry, 2005).

2.4.3 State of the art numerical modeling of snow thermodynamics

Current "state of the art" numerical modeling of snow and sea ice thermodynamics naturally build upon successes and failures of past models, with components adapted and adopted from previous models. An advantage of numerical models is the understanding of complex interactions and feedbacks that may be impossible to resolve from direct measurement; this allows for improvement of previously unsuccessful components of models, for multi-layer adaptations, and for removal of negligible components. The results of these developments are complex but efficient models, which better capture the dimensionality of real conditions. State-of-the-art snow models include multi-layered thermal conductivity, density, and temperature, and addresses vertical heat diffusion, new snowfall, and surface and internal melting. Additional snowpack dynamics include density based on wind speed, and flooding from sea ice depression by snow, which results in a snow-ice/slush refreeze layer. Snow inputs for model initiation can

be measurement based or can be computed from reanalysis. Flux between the snow surface and atmosphere are represented, as well as albedo. Sensible and latent heat are considered both within the snow pack, between layers, and in turbulent fluxes at the surface. Differences in energy between internal and external heat fluxes are used to model sea ice growth/ablation. Initiation and perturbation of the model occurs with air temperature and relative humidity, snowfall, and radiative fluxes (Q_L and Q_S). Snow representations are improved when compared to past models and are well within the natural variability of snow on sea ice; however, a fixed oceanic heat flux may not accurately represent ice formation and accretion at the ice-ocean interface, which affects brine expulsion, and in turn thermal conductivity and capacity. Current state of the art models characterize thermodynamic processes and feedbacks associated with albedo, water vapor, clouds, temperature inversions/lapse rates, aerosols, flooding, advection, and latent and sensible heat transfers for use in climate system modeling.

2.4.3.1 SNTHERM89.rev4

SNTHERM is a state-of-the-art one-dimensional, multilayer thermodynamic model originally developed for snow and soil temperature simulations developed by Jordan (1991), and which was later adapted for sea ice (Jordan and Andreas 1999; Andreas et al. 2004). SNTHERM uses hourly meteorological variables to simulate thermodynamic processes of air, soil, and liquid, solid, and vapor states of water. The simulated outputs include snow cover properties such as temperature, SWE, grain size, liquid water content, layer thickness, and depth, which are pertinent to microwave remote sensing. Snow and sub-surface layers are divided into control volumes. Numerical solutions for each volume is calculated from equations for heat and mass balance. Heat fluxes are transferred from snow to sub-surface, which in turn updates snow

temperatures at each time step (5 seconds). Snow accumulation, densification, metamorphosis, and ablation are considered with regard to the impact of each on optical and thermal properties of the volume. For each precipitation event, SNTHERM adds a new layer to the top of the snowpack; the layer is combined with the one below if and when the layer thickness reaches a prescribed minimum (Jordan 1991; Durand 2007). The model predicts grain growth from thermal and vapor gradients, and accounts for water percolation, which is artificially drained from the bottom of the snowpack-surface interface. It requires an initial state of snow, ice, or soil character including, the number of layers (nodes), grain size, density, temperature, mineral density, heat capacity, and thermal conductivity. SNTHERM is driven by hourly meteorological variables including temperature (K), relative humidity (%), wind speed (m s^{-1}), incoming and outgoing shortwave radiation and incoming longwave radiation (W m^{-2}), and precipitation amount (SWE, mm), and effective particle size (m).

The SNTHERM89.rev4 (SNTHERM, n.d.) (Figure 2.16) was used in this work as it is thoroughly validated, flexible, publicly available, and easy to use. As such, it does not treat sea ice specifically; however, sea ice parameters can be entered as layers in the model to account for the thermal capacity and conductivity. SNTHERM bases grain growth for dry snow on current grain size and vapor flux through the snowpack, with a set maximum flux and kinetic growth limit of 5 mm grain diameter. The model assumes no vapor flux between the bottom layer and that directly above it (Jordan 1991; Jordan and Andreas 1999), resulting in slowing grain growth for the layer above (Durand 2007). SNTHERM89.rev4 does not account for brine wicking (capillary action) in the snow and associated salinity values. This is an important consideration, as brine-wetted snow affects C-band backscatter through both increased loss and volume

scattering, and impacts seasonal thermodynamic processes (Barber et al. 1994; Geldsetzer et al. 2007).

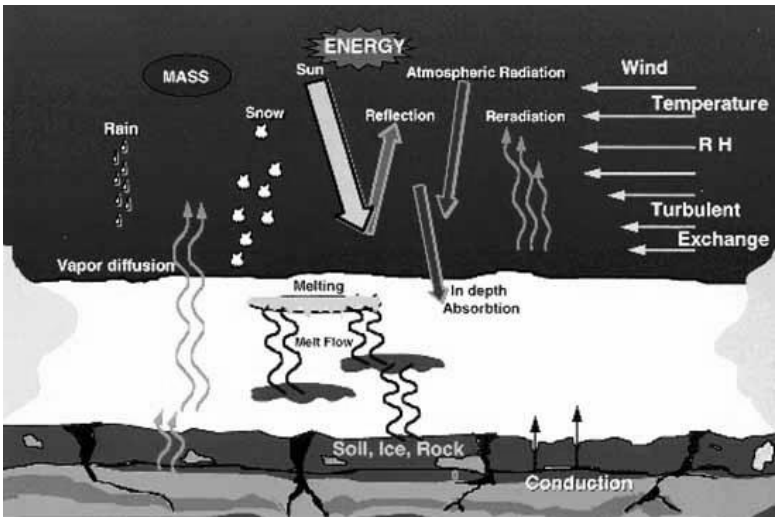

Figure 2.16. From ERDC Cold Regions Research and Engineering Laboratory. (SNTHERM Snow Thermal Model)

Chapter Three: **C-band backscatter from a complexly-layered snow cover on first-year sea ice**

3.1 Abstract

We present a case study of observed and modeled C-band microwave backscatter signatures for a complexly-layered snow cover on smooth, landfast, first-year sea ice. We investigate how complexly-layered snow affects the backscatter, by comparing signatures with those for a simple snow cover, and through model sensitivity analysis. Backscatter signatures are obtained using a surface-based scatterometer, on sea ice in Hudson Bay, Canada. Coincident in-situ snow and ice geophysical measurements, and on-ice meteorological observations, describe the snow cover formation and structure. A multi-layer snow and ice backscatter model is used to iteratively add and subtract components of the complex snow cover to assess their impacts on the overall backscatter. For incidence angles between 20° and 70° the backscatter from a complex snow cover on smooth first-year sea ice is significantly higher than backscatter from a simple snow cover on similar sea ice. Sensitivity analysis suggests that rough ice layers formed within the complex snow cover and those superimposed at the sea ice interface, are the physical mechanisms that affect an increase in surface and volume backscattering. This has implications for sea ice mapping, geophysical inversion, and snow thickness studies.

3.2 Introduction

3.2.1 Context

Freezing rain/precipitation events are increasing in frequency across the Canadian Arctic, the frequency of blowing snow events are decreasing particularly in the spring, and days with no weather events are decreasing in frequency (Hanesiak and Wang 2005). An expected increase in

the timing and magnitude of late winter season rain events in the high Arctic, and associated increases in 95th percentile precipitation events, with more precipitation falling as rain rather than snow (Trenberth et al. 2007), has contributed to a change in the Arctic sea ice extent, thickness, and composition (Barber et al. 2009). Loss of Arctic Sea ice is associated with changes in albedo due to changes in snow and ice cover distribution, thickness, composition, and duration (Curry et al. 1995).

Snow cover distribution plays a significant role in the Arctic ecosystem, as it has high spatiotemporal variability which needs to be better understood (Iacozza and Barber 2001). Snow cover on sea ice is highly variable spatiotemporally, and has significant reflective and thermodynamic properties, which play an important role in the exchange of heat and energy across the ocean-sea ice-atmosphere interface, and therefore, on sea ice formation, ablation, extent, and thickness (Maykut 1982; Ledley 1991; Curry et al. 1995; Iacozza and Barber, 2001). The presence of brine, forced from sea ice into the overlying snow cover during first-year ice (FYI) formation, changes the dielectric and thermal properties of snow cover and, therefore, affects ice formation and ablation (Maykut and Untersteiner 1971; Geldsetzer et al. 2009).

From winter to early melt, the snow cover on Arctic sea ice has been generally thought of as a two layer system consisting of randomly oriented, fine-grained, lower density fresh snow overlying coarse-grained depth hoar of highly variable density (Crocker 1992; Barber et al. 1995). Spatiotemporal variability and complex layering stem from several factors including ice roughness, storm length and intensity, precipitation type, and predominant wind direction and speed (Iacozza and Barber 2001). With increased alternation of rain and snow storm events occurring in the early spring and late fall (Trenberth et al. 2007), the layering of snow packs will

become more complex (i.e. an increase in the number of ice lenses and drainage channels and inclusions within the snow pack).

3.2.2 Microwave interactions

Microwave energy undergoes surface scattering at lower incidence angles (< 30º) and backscatter return falls in a general linear trend with increasing incidence angle, as microwave energy is increasing directed away from the sensor in a specular fashion. At greater incidence angles (> 30º), volume scattering, which is masked by surface scattering at lower incidence angles, becomes the dominant scattering type and returns backscatter with an intensity greater than that of the surface scattering, as energy is reflected back by crystals, rough ice layers, and ice inclusions (Drinkwater and Crocker 1988). In homogeneous dry snow conditions, microwave energy passes through the snowpack with little return, and the primary backscattering and attenuation occurs because the brine at the snow ice interface, due to a strong dielectric mismatch (Nghiem et al. 1995a).

Microwave interaction with snow covered sea ice is a function of both radar parameters (incidence angle, wavelength, and polarization) and snow and ice electro-thermo-physical properties (size, shape and orientation of scatterers, surface roughness, and dielectric permittivity and loss). At C-band, dry snow is generally transparent to microwaves due to low dielectric permittivity and randomly oriented proportionally small grains with respect to microwave length (Barber and Nghiem 1999). Commonly observed coarse-grained, saline depth hoar at the base of the snow can exhibit high brine volume resulting in increased surface and volume scattering, decreased penetration depth, and increased spatial heterogeneity. Below the brine-wetted snow layer, the snow–ice interface contributes surface scattering as a function of its roughness, and

brine inclusions in the upper sea ice layers contribute additional volume scattering. (Crocker 1992; Barber and Nghiem 1999; Geldsetzer et al. 2009).

3.2.3 Research Objectives

This work presents in-situ geophysical data, C-band microwave response, and modeled backscatter for complexly-layered snow data collected in Churchill, Manitoba in 2009. We compare geophysical data and associated microwave backscatter response to snow pack conditions over smooth FYI, and conduct a sensitivity analysis to assess the effects and importance of the ice layers and their properties on overall backscatter from the snowpack. To help achieve our research goal, we will specifically address three interrelated research questions:

1. What are the observed geophysical characteristics and C-band backscatter signatures for a complexly-layered snow cover on first-year sea ice?

2. How do observed and simulated C-band backscatter compare for a complexly-layered snow cover over first-year sea ice?

3. How do the components of a complexly-layered snow pack over first-year sea ice contribute to C-band backscatter?

4. What are the implications of these to microwave backscatter classification of sea ice?

3.3 Methods

3.3.1 Study Area and Sites

The Complex Snowpack sampling location for this study was located on landfast smooth first-year sea ice in the western Hudson Bay coastal region (N 58.8121 W093.8953), about 23 km east

of Churchill, Manitoba (Figure 3.1). The experiment was conducted on May 15th, 2009 on a pan of smooth first-year sea ice approximately 4 km long and 1.5 km at its widest, and was oriented south-west to north-east and included snow geophysical and surface-based backscatter measurements of complexly-layered snow.

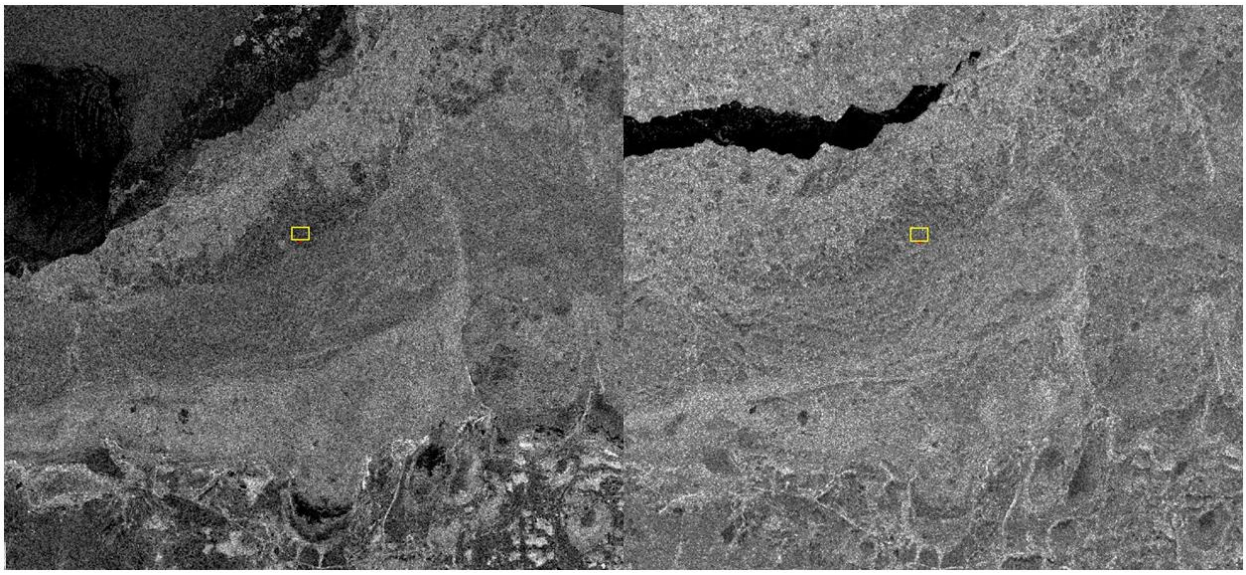

Figure 3.1. RADARSAT-2 σ^0_{HH}: April 7 (left, FQ12), May 15 (right, FQ19). The smooth pan of ice is approximately 4 km x 1.5 km at its widest, the yellow area of interest within that pan is 300 m x 400 m x 45 m, and the red dot is the scatterometer location (40 m x 45 m).

For comparison, a Simple Snowpack sampling site is also used, located in Allen Bay, (N74.6975 W094.8156) on smooth first-year sea ice, near Resolute Nunavut. The experiment was conducted on May 19, 2006 on a pan of smooth first-year sea ice including geophysical and surface-based backscatter measurements of a 21 cm simple snow cover. The study area is more fully described in Geldsetzer et al. (2009).

3.3.2 Data Collection

3.3.2.1 Meteorological Data

For the Churchill 2009 data set, air temperature and relative humidity were collected 2 m above the snow-ice interface by a meteorological station located on the sea ice, within 500 m of the sample site. Environment Canada Churchill weather station observations were also used (wind speed, precipitation type); these data were gathered at the Churchill airport, about 20 km from the study sites. Meteorological data for the Resolute 2006 data set was collected via the Environment Canada Resolute weather station 3 km from the sample sites.

3.3.2.2 Snow Geophysical Data Collection for both Churchill 2009 and Resolute 2006

Snow pit (1 m^2) samples at the Churchill 2009 site were carried out over the course of the day, at 3 sites adjacent (within 5 m) to the scatterometer scan area, during scatterometer data acquisition. Snow pit samples at the Resolute 2006 site were carried out similarly, but at 4 times daily for the sample period. Snow properties sampled from the non-illuminated snow face at 2 cm vertical resolution include: temperature (±0.05°C); grain morphology and long and short axis lengths determined from pictures of grains on standard grid cards, dielectric properties (e', e'') measured at both 20 MHz (±2%) and 50 MHz (±1.5%); snow depth was measured using a standard collapsible meter stick. The 20 MHz and 50 MHz measurements of e' were converted to 5.5 GHz values employing models from (Geldsetzer et al. 2009). Additional notes regarding snow structure (e.g. ice layers, polyaggregate crystals) were also made. Density samples were taken at 2 cm intervals for the entire snow depth employing a 66 cm^3 density cutter, with samples bagged for weighing on a digital scale (±0.01 g), giving a snow density accuracy of ±0.04 g cm^{-3} (Drobot and Barber 1998). Precise sampling was difficult where ice layers occurred in the snowpack. Marsh and Woo (1984) found ice layer densities ranging from 630 kg m^{-3} to 950 kg m^{-3}, with an

average of 800 kg m^{-3}. More recent work by Watts et al. (unpublished) averaged 0.877 g cm^{-3}, which was used for ice layer density in this work. Salinity (±0.5%) was recorded using a conductivity meter on melted snow density samples, in the lab at the end of the field day.

3.3.2.3 Microwave backscatter

Surface-based C-band microwave backscatter measurements were obtained continuously throughout the day from a fixed location, using a frequency-modulated continuous-wave scatterometer (5.5 GHz central frequency) mounted at a height of 2.20 m (2.26 m for Resolute 2006) (Figure 3.2 and Table 3.1). Samples were acquired from 20° to 70° (21° to 67° for Resolute 2006) elevation in 2° increments, and integrated over a minimum azimuthal range of 80° (50° for Resolute 2006). A full description and validation of the scatterometer, signal processing, accuracy, and near-field correction are available in Geldsetzer et al. (2007). Scatterometer samples were selected concomitant to geophysical samples.

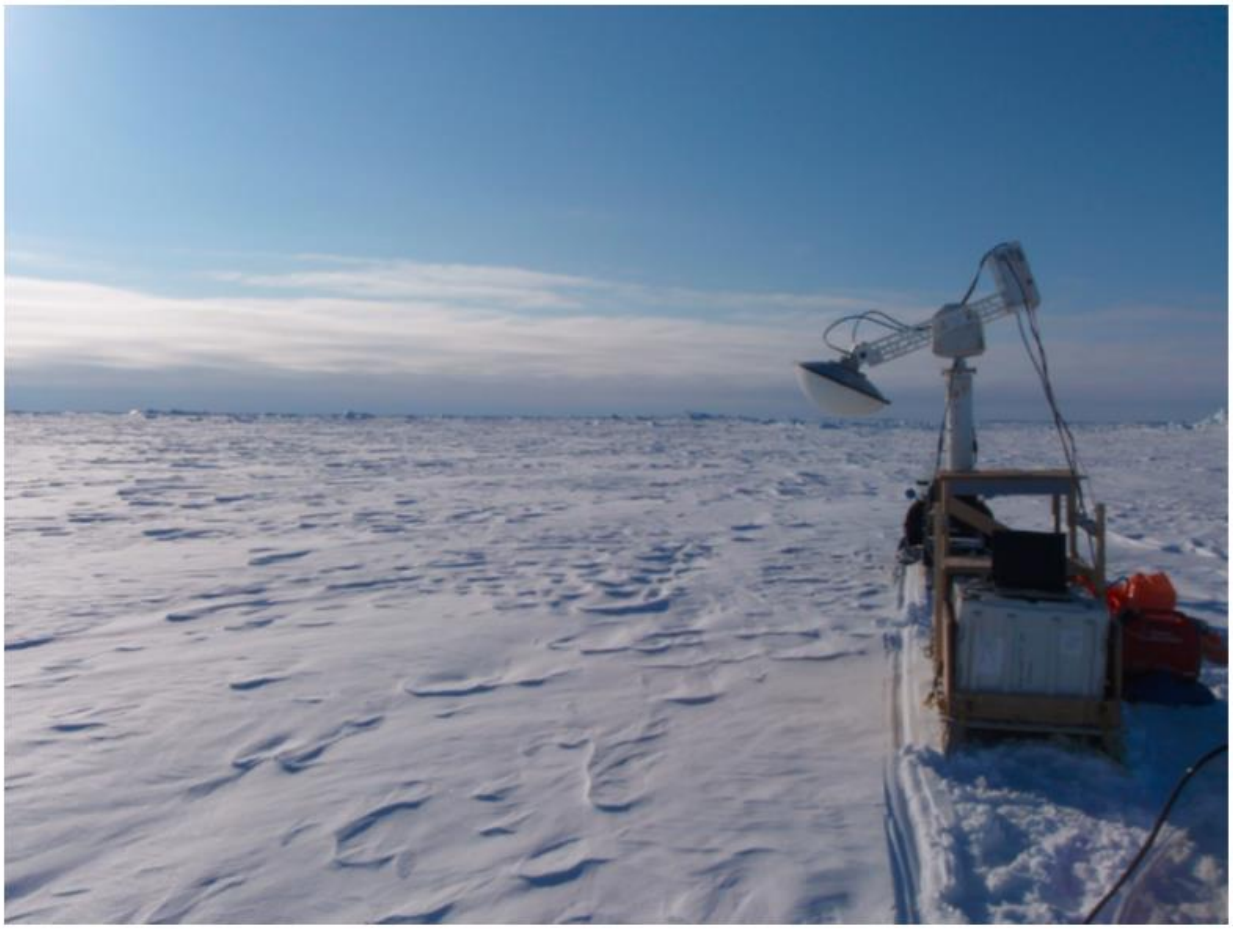

Figure 3.2. Surface-based scatterometer and study site on May 15th 2009, near Churchill MB. Note the natural variability of snow depth and surface texture.

Two RADARSAT-2 images are used: the first image is from April 7, when the ice surface was primarily snow-free (see meteorology and geophysical, Sections 3.4.2 and 3.4.3); the second image coincides with the scatterometer measurements on May 15th, with 25–35 cm of complex snow cover (Figure 3.1. RADARSAT-2 σ0HH: April 7 (left, FQ12), May 15 (right, FQ19).Figure 3.1). RADARSAT-2 fine quad-polarized (FQ) images are calibrated to sigma-naught, orthorectified (nearest neighbour) to 5×5 m, and filtered using a Refined Lee filter with a 7×7 window. The resulting ENL is ~5, providing an expected residual standard deviation due to

speckle of ~2 dB. Areas of Interest (AOIs) are used to sample images for: 1) the area immediately adjacent to the scatterometer measurements; 2) for the FYI pan; and 3) for the nearby Churchill runway, for pseudo-invariant comparison.

Table 3.1. Surface-based C-band scatterometer specifications.

RF output frequency	5.5 GHz ±250MHz
Antenna type	0.61 m parabolic reflector, dual linear polarization
Antenna beamwidth	5.4°
Cross polarization isolation	>30 dB, measured at the peak of the beam
Transmit power	12 dBm
Bandwidth	5-500 MHz, user adjustable
Range resolution	0.30 m
Polarization mode	Polarimetric (HH,VV,HV,VH)
Noise floor	Co ~ -36 dBm, Cross ~ -42dBm
External calibration	Trihedral corner reflector

The microwave parameters calculated and presented in this work, from both the surface-based scatterometer and RADARSAT-2, are: the co-polarized backscattering coefficient (dB) in both vertical (σ^0_{VV}) and horizontal polarization (σ^0_{HH}); and the cross-polarized (σ^0_{HV}) backscattering coefficient (dB). Further details regarding these parameters are available in Chang et al. (1996), Bernier and Fortin (1998), and Geldsetzer et al. (2007).

3.3.3 Multi-layer Snow and Ice Backscatter Model

A multilayer snow and ice backscatter model is used to calculate the co-polarized backscattering coefficient (dB) in both vertical (σ^0_{VV}) and horizontal polarization (σ^0_{HH}), by taking into account

the surface scattering contributions and transmission of each snow or ice layer interface, and the volume scattering contributions, absorption, and refraction within each snow or ice layer. Total backscatter for the snow-covered sea ice is calculated based on the combined contributions of as many snow and ice layers as are present. This constitutes an expansion of the methods of Kim et al. (1984) and Ulaby et al. (1984). Surface scattering is modeled using the Kirchoff physical optics method, appropriate for smooth surfaces that can be described by a Gaussian distribution function (Rees 2006). Volume scattering is modeled based on the number density and effective size of ice-particles in each layer (Drinkwater 1989). A two-way loss factor is used to account for reductions in both incoming and outgoing scattering power (Winebrenner et al. 1992; Kendra et al. 1998). The MSIB model is implemented and fully described in Scharien et al. (2010).

Model inputs for each layer are: thickness (cm), density (g cm^{-3}), temperature (°C), salinity (ppt), grain size (m), root-mean square height surface roughness (RMS, mm), correlation length (LC, mm), dielectric permittivity (e′), and dielectric loss (e″); the model is also capable of semi-physical dielectric mixture modeling (e′ and e″) as fully described in Geldsetzer et al. (2009) and Scharien et al. (2010). RMS and LC were held constant at 5 mm and 30 mm respectively for this work to approximate the rough interfaces.

3.4 Results

3.4.1 Formation of Complexly-Layered Snow

Previous to April 11, 2009 the sea ice at the study site was scoured clear of snow by high winds. On April 11th, the brine at the surface of the FYI was subsequently superimposed by a rough, discontinuous, ice layer formed by a mixed snow and freezing rain event. Between April 14th and 15th, 13 cm of snow recovered the pan, and a mixed snow and rain event created a thin

discontinuous freshwater ice layer at the air-snow interface. Drainage from the rain event created inclusions and poly-aggregates in the snow beneath the ice layer. Various snow storm events between April 16th and May 6th then covered this ice layer. A warming and rain and event on May 11th created a 2 cm to 4 cm thick freshwater ice layer between 18 cm and 22 cm above the snow-ice interface, and drainage through the snowpack created ice inclusions up to 3 cm along the short axis. This ice layer was then covered by a subsequent snowfall event from May 12th to May 15th, resulting in a total snow depth of 25 cm to 35 cm; variation in snow thickness was due to the natural undulating structure of snow on smooth sea-ice. The formation of complexly-layered snow cover is stark in contrast to more commonly observed simple snow covers. Figure 3.3 provides a conceptual understanding of the simply and complexly-layered snow packs.

The 21 cm thick simple snow pack, collected in Resolute 2006, was composed of a melt freeze layer, a windslab layer, and depth hoar, overlaying smooth first-year sea ice. This configuration is typical of the simple snow configurations used in previous research (Barber et al. 1995; Barber and Nghiem 1999; Geldsetzer et al. 2009). It is used in this work for comparison of modeled backscatter; it provides a baseline example for typical backscatter from simple snow over smooth sea ice. This is used for comparison with backscatter contribution of the various components of complexly-layered snow (Section 3.4.7).

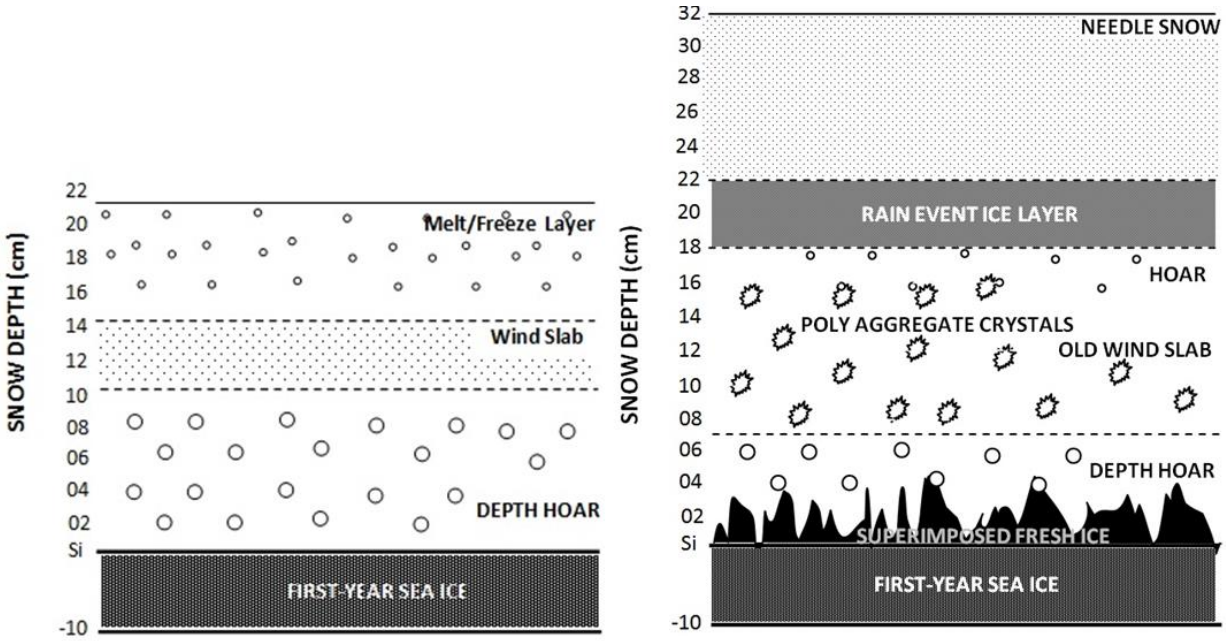

Figure 3.3. Simple (left) and Complexly-Layered (right) snow schematics for conceptualization.

3.4.2 Meteorological Data

May 15th, 2009 was a sunny, cloudless day, with sunrise at 0447h and sunset at 2139h. The 2 m air temperature reached a minimum of -15°C at 0600h and climbed steadily to a high of -1.2°C at 1600h; while the 2 m relative humidity increased from 65% to 80% over roughly the same time period.

3.4.3 Snow Geophysical Data

Figure 3.4 through Figure 3.8 present measured snow geophysical data and include conceptual and actual representations of snow layering, snow grains and inclusions, and ice layers. The geophysical samples were taken throughout the day with Sample 1 taken at 0737h, Sample 2 taken at 1155h, and Sample 3 taken at 1725h, and represent a range of spatially variable snow conditions.

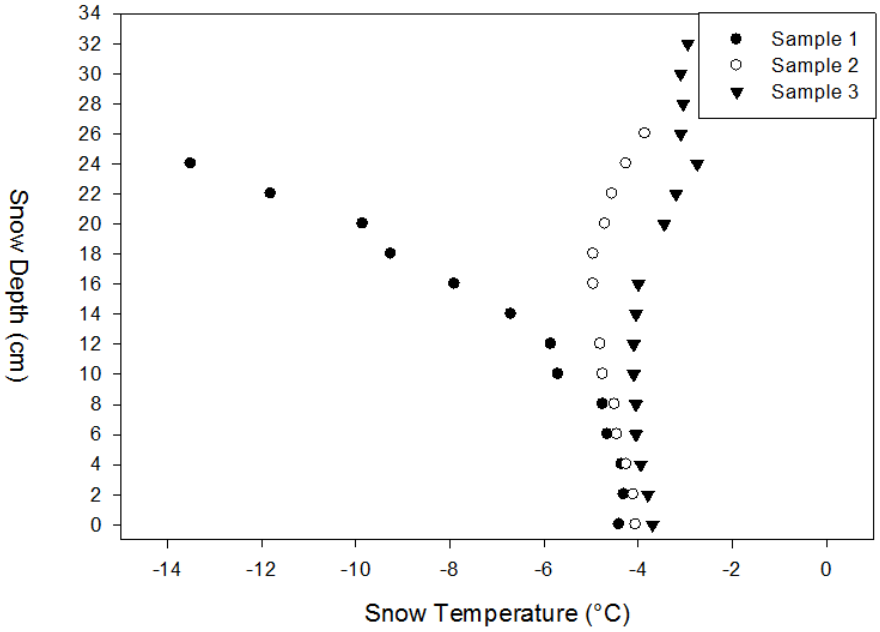

Figure 3.4. Temperature for Complexly-Layered Snow, Churchill, Manitoba 2009. Zero depth is the sea ice surface.

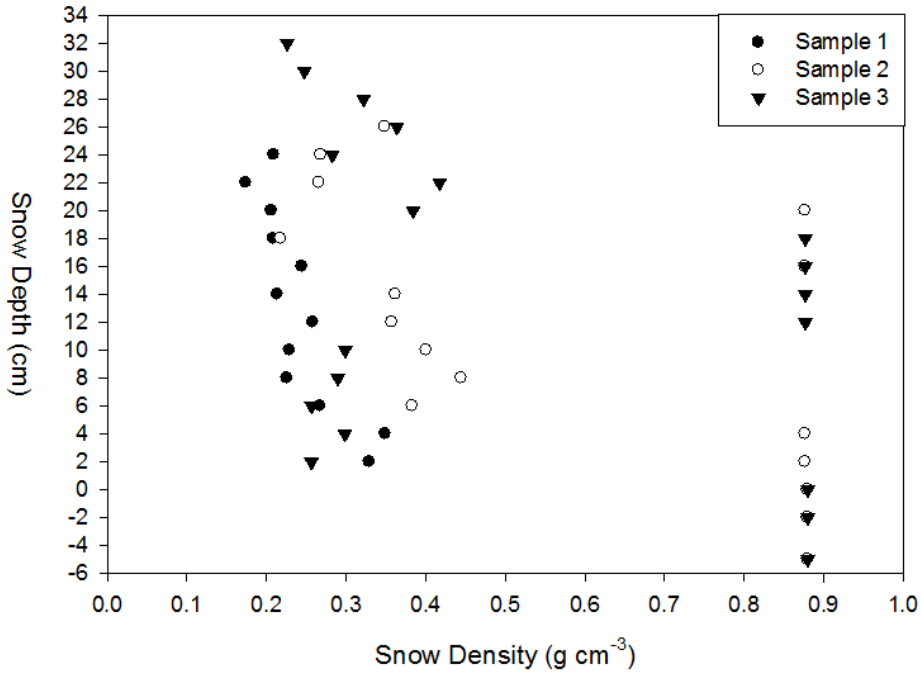

Figure 3.5. Snow density for Complexly-Layered Snow, Churchill, Manitoba 2009. Zero depth is the sea ice surface.

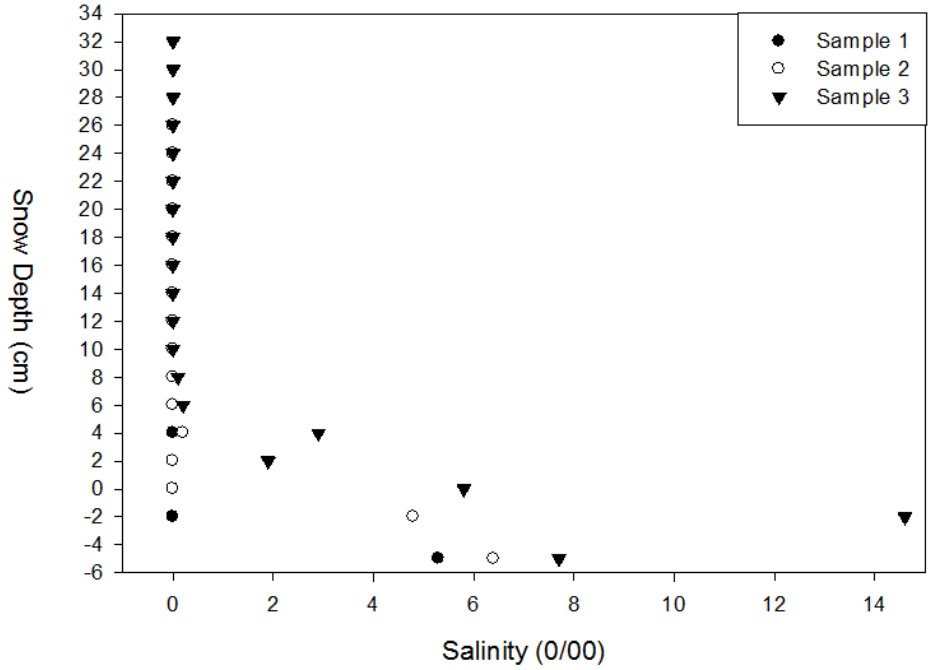

Figure 3.6. Salinity for Complexly-Layered Snow, Churchill, Manitoba 2009. Zero depth is the sea ice surface.

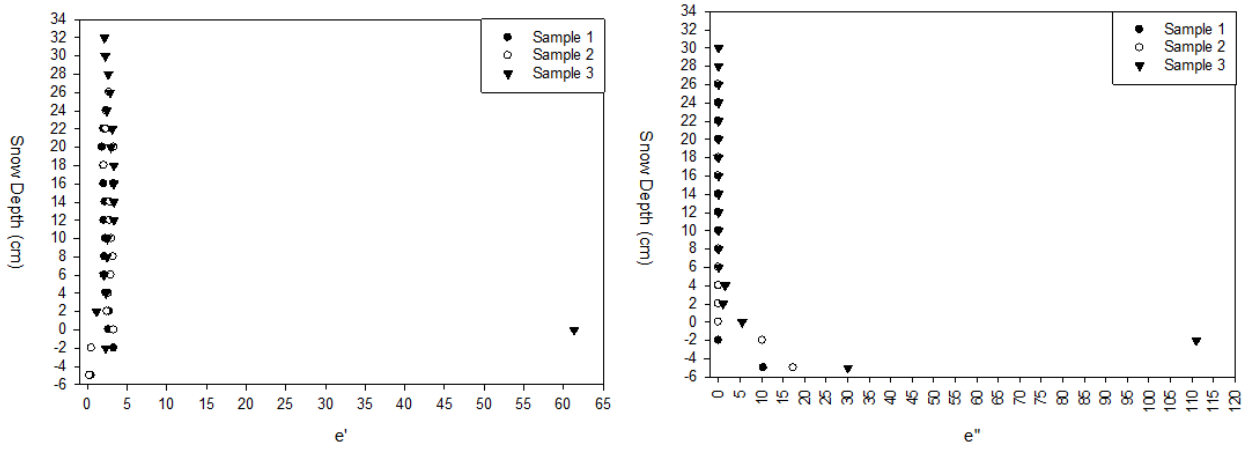

Figure 3.7. Dielectric permittivity (e') and loss (e") for Complexly-Layered Snow, Churchill, Manitoba 2009. Zero depth is the sea ice surface.

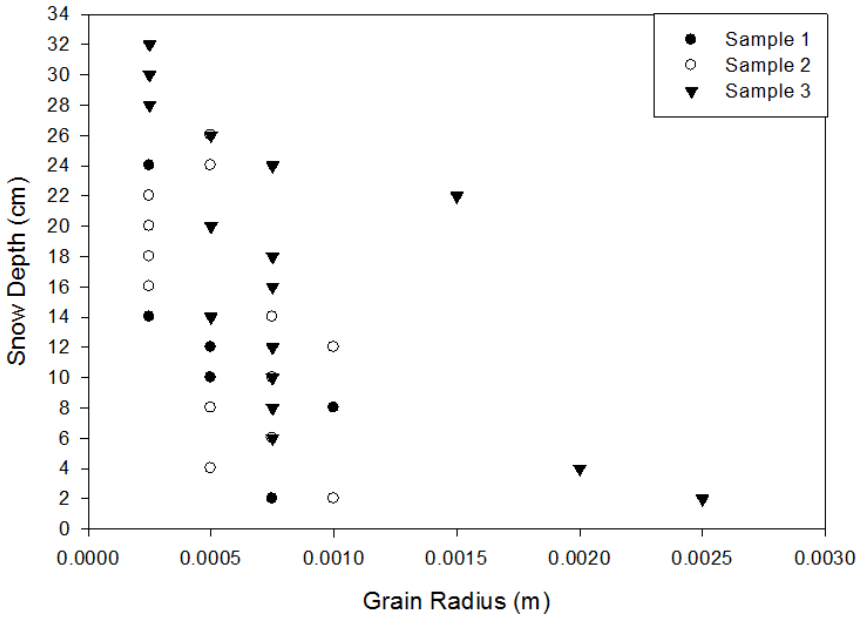

Figure 3.8. Predominant snow grain radius for Complexly-Layered Snow, Churchill, Manitoba 2009. Zero depth is the sea ice surface.

The snow temperature increased from -13°C to -4°C from morning to evening for the upper most layers on May 15th, 2009 in Churchill; however, the temperature remained relatively constant at -4°C for the lower 8cm. The snow densities generally ranged from 0.2 g cm^{-3} to 0.4 g cm^{-3}. Higher densities occur at the warming/rain-event ice-crust, and superimposed ice overlaying the smooth first-year sea ice. We could not obtain a density for these layers due to equipment and sampling limitations; therefore, these were given densities of 0.877 g cm^{-3} (Watts et al. unpublished).

Brine wetting typically takes place in the lower 6 cm of the snowpack in the depth hoar just above the snow-sea ice interface; the brine in this work occupied the bottom 2 cm to 4 cm of the depth hoar only in Sample 3. Samples 1 and 2 had depth hoar that was largely devoid of brine, as the superimposed ice layer at the sea ice interface primarily trapped the brine in the sea ice. The

brine present in the lower 6 cm of the Churchill 2009 snow pack ranged from 0 to 7 ppt, with the average being about half that of typical values (Barber and Nghiem 1999). The variance in these values can be attributed to the discontinuous nature of the superimposed fresh-ice layer in Churchill 2009, which affects the availability of brine to the snowpack for wicking. The dielectric permittivity data generally shows values falling between 1.3 and 4; the exception in a high permittivity, thin brine layer on the surface of the sea ice and below the superimposed ice. The dielectric loss ranges from 0 to 30; again with an exception for the thin brine layer.

Dominant crystal size was observed to increase generally with depth, as is expected, but also increased adjacent to the ice crusts and lenses. The data reflect the increased variability of snow grain diameter that may occur in complexly-layered snow covers, when compared to that of simple snow covers. This is likely due to variation in crystal growth and morphology as a result of modified thermal and vapor gradients within the snow pack, caused by the rain event, drainage channels, and the subsequent rain event ice layer. These measurements are not representative of the many larger inclusions and polyaggregate crystals that occurred with the general snow matrix for the complexly-layered snow cover.

3.4.4 Observed C-Band Backscatter from Complexly-Layered Snow

SAR measurements on April 7th, show σ^0_{HH} at the scatterometer study site (Figure 3.1: red spot) is −18.9 dB. This value, at an incidence angle of 32°, is indicative of smooth FYI. σ^0_{HV} at the scatterometer study site is −34.2 dB, also indicative of smooth FYI (Geldsetzer et al. 2007; Geldsetzer et al. 2009; Gill and Yackel 2012) (Table 3.2). σ^0_{HH} for the FYI pan area (yellow rectangle) is −17.1 dB. The higher value for the pan compared to the scatterometer site, is primarily due to a small proportion of high-backscatter areas within the larger smooth area.

These are likely associated with the protruding ice blocks that can be seen in the background of the photograph of the surface-based scatterometer (Figure 3.2). The σ^0_{HH} and σ^0_{HV} values fall at the transition from smooth FYI to rough FYI (Geldsetzer et al. 2007; Geldsetzer et al. 2009; Gill and Yackel 2012).

Between April 7th and May 15th, the expected difference in σ^0_{HH}, due to incidence angle dependency, assuming no change in snow structure for smooth FYI, is a reduction of −1.7 dB (Makynen et al. 2002). However, at the scatterometer study site, σ^0_{HH} increases by 5.7 dB, to −13.2 dB. For the FYI pan, σ^0_{HH} increases by 3.9 dB, to −13.2 dB. The expected difference for σ^0_{HV} is < 1 dB (Gill and Yackel 2012); however, it too, increases significantly, by 6.9 to 8.2 dB.

The May 15 σ^0_{HH}, σ^0_{VV} and σ^0_{HV} values for smooth FYI are indicative of rough FYI to deformed FYI (Makynen and Hallikainen 2004; Gill and Yackel 2012), and may even be mistaken for multi-year sea ice (Geldsetzer et al. 2007). Given that the morphology of the underlying sea ice does not change, as can be observed (Figure 3.1: left and right), it is unlikely that the sea ice surface roughness changes between April 7th and May 15th. Therefore, the increase in σ^0_{HH}, σ^0_{VV} and σ^0_{HV} between April 7th and May 15th is likely a function of the development of and layering in the snow cover. Additional evidence for this is that the May 15th scatterometer site σ^0_{HH} and σ^0_{VV} values are similar to those for the FYI pan, suggesting that differences in backscatter from the underlying sea ice are masked by the snow cover. The low standard deviation values suggest homogeneity for the scatterometer site and the pseudo-invariant runway, as expected. The FYI pan as a whole is likely somewhat less homogeneous.

Table 3.2. Churchill study area RADARSAT-2 measurements. 2009-04-07 image is FQ12 (32.2° incidence angle); 2009-05-15 image is FQ19 (39.1° incidence angle). Backscatter and standard deviation values are in dB.

	2009-04-07	2009-05-15	2009-04-07	2009-05-15	2009-04-07	2009-05-15
	σ^0_{HH}	σ^0_{HH}	σ^0_{VV}	σ^0_{VV}	σ^0_{HV}	σ^0_{HV}
Scatterometer site 72 pixels ~ 40×45 m	−18.9 ± 1.8	−13.2 ± 1.4	−18.2 ± 1.5	−13.2 ± 1.1	−34.2 ± 1.7	−26.0 ± 1.8
FYI pan 4800 pixels ~ 300×400 m	−17.1 ± 2.0	−13.2 ± 1.9	−17.6 ± 2.1	−13.9 ± 1.9	−31.0 ± 2.1	−24.1 ± 2.2
Runway (asphalt) 426 pixels	−19.5 ± 1.7	−20.7 ± 1.5	−19.5 ± 1.7	−19.8 ± 1.7	−28.8 ± 1.5	−28.3 ± 1.6

The surface-based scatterometer operated continuously through the day on May 15th. The observed backscatter remained relatively constant, which suggests averaging of heterogeneous snow conditions in the approximately 8 m x 8 m scan footprint. This interpretation is reinforced by the close agreement of the backscatter magnitudes from the RADARSAT-2 data (Figure 3.9 through Figure 3.11).

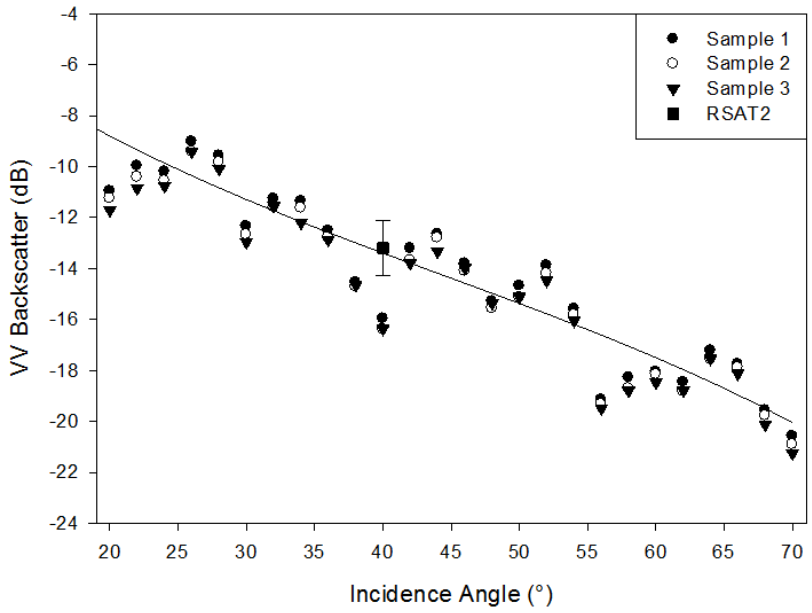

Figure 3.9. Observed C-Band Backscatter (σ°vv) for Complexly-Layered Snow, Churchill, Manitoba 2009. Trend line is a cubit fit and the RSAT2 data point is the red area in Figure 3.1

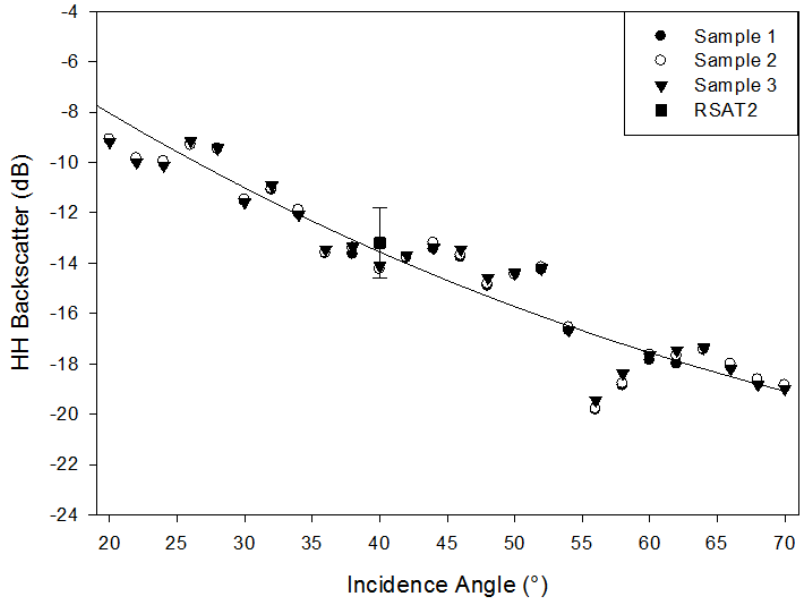

Figure 3.10. Observed C-Band Backscatter (σ°_{HH}) for Complexly-Layered Snow, Churchill, Manitoba 2009. Trend line is a cubic fit and the RSAT2 data point is the red area in Figure 3.1.

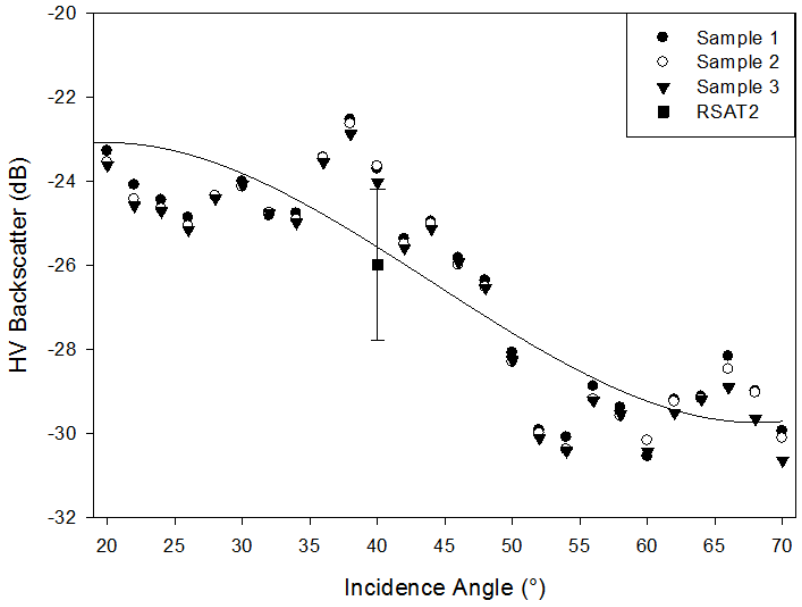

Figure 3.11. Observed C-Band Backscatter ($\sigma°_{HV}$) for Complexly-Layered Snow, Churchill, Manitoba 2009. Trend line is a cubic fit and the RSAT2 data point is the red area in Figure 3.1.

3.4.5 C-Band Backscatter from Complexly-Layered Snow

These results show an increased co-pol and cross-pol backscatter for the complexly-layered snowpack, when compared to other similar studies of simple snow (Barber et al. 1995; Geldsetzer et al. 2007; Geldsetzer et al. 2009) (Figure 3.9 through Figure 3.11). The observed backscatter σ^0_{VV}, σ^0_{HH}, and σ^0_{HV} for complexly-layered snow is 5 dB to 10 dB greater than that for simply-layered snow for similar underlying smooth, first-year sea ice conditions. The 2 cm to 4 cm thick, mid-snow pack ice layer, as well as large and polyaggregate grains bonded to the ice layer, were located between 18 cm and 23 cm above the sea ice interface. Ice inclusions (5 cm x 2 cm) and snow crystal axes approaching 18 mm were present in the snow below this ice layer, enabling further potential volume scattering; although the dielectric properties of this layer suggest minimal influence at C-band.

A potential explanation for the comparative increase is that the complex ice layering, variety of grain shapes and sizes, large ice and polyaggregate inclusions, and rough interfaces caused by the superimposed ice at base of the snow pack, scatter much of the microwave energy, and thus, the surficial interaction (attenuation) with the brine skim below is masked by the snowpack structure. We investigate this by comparing modeled and observed backscatter, and via modeled sensitivity analysis (Sections 3.4.6 and 3.4.7). This is likely due to surficial and volume interactions of microwave energy with the mid-snow pack ice layer and/or the rough superimposed ice layer at the base of the snow pack.

3.4.6 Comparison of Observed and Modeled C-Band Backscatter for Complexly-Layered Snow

Backscatter is modeled for the three samples, parameterized using the geophysical observations in Table 3.3. The modeled backscatter, compared with observed, is within 2 dB for incidence angles between 20 and 30 degrees (for all samples) and underestimates (5 dB for Sample 1 and Sample 2) or overestimates (5 dB to 10 dB for Sample 3) between 30 and 70 degrees incidence angle (Figure 3.12). This is likely due to the heterogeneous nature of the snow sampled.

Table 3.3. Model inputs for Samples 1, 2, and 3.

Sample 1	Thick	Dens	Temp	Sal	Grain(m)	Sample 2	Thick	Dens	Temp	Sal	Grain(m)	Sample 3	Thick	Dens	Temp	Sal	Grain(m)
Layer # 12	0.02	0.209	-13.5	0	0.00025	Layer # 13	0.02	0.349	-3.9	0	0.0005	Layer # 16	0.02	0.226	-3	0	0.00025
11	0.02	0.174	-11.8	0	0.00025	12	0.02	0.269	-4.3	0	0.0005	15	0.02	0.248	-3.1	0	0.00025
10	0.02	0.206	-9.9	0	0.00025	11	0.02	0.266	-4.6	0	0.00025	14	0.02	0.322	-3.1	0	0.00025
9	0.02	0.209	-9.3	0	0.00025	10	0.02	0.7	-4.7	0	0.00025	13	0.02	0.364	-3.1	0	0.0005
8	0.02	0.245	-7.9	0	0.00025	9	0.02	0.218	-5	0	0.00025	12	0.02	0.282	-2.8	0	0.00075
7	0.02	0.213	-6.7	0	0.00025	8	0.02	0.877	-5	0	0.00025	11	0.02	0.877	-3.2	0	0.0015
6	0.02	0.259	-5.9	0	0.0005	7	0.02	0.362	-5	0	0.00075	10	0.02	0.384	-3.5	0	0.0005
5	0.02	0.229	-5.7	0	0.0005	6	0.02	0.358	-4.8	0	0.0001	9	0.02	0.877	-3.9	0	0.00075
4	0.02	0.226	-4.8	0	0.001	5	0.02	0.401	-4.8	0	0.0005	8	0.02	0.877	-4	0	0.00075
3	0.02	0.267	-4.7	0	0.00075	4	0.02	0.445	-4.5	0	0.00075	7	0.02	0.877	-4.1	0	0.0005
2	0.02	0.35	-4.4	0	0.0005	3	0.02	0.383	-4.5	0	0.0005	6	0.02	0.877	-4.1	0	0.00075
1	0.02	0.33	-4.3	0	0.00075	2	0.02	0.88	-4.3	0.2	0.001	5	0.02	0.299	-4.1	0.1	0.00075
0	0.05	0.88	-4.4	5.3	0.00005	1	0.02	0.88	-4.1	4.8	0.00005	4	0.02	0.287	-4.1	0.2	0.00075
						0	0.05	0.88	-4.1	6.4	0.00005	3	0.02	0.257	-4.1	2.9	0.00075
												2	0.02	0.298	-4	1.9	0.0002
												1	0.02	0.257	-3.8	5.8	0.00025
												0	0.05	0.88	-3.7	14.6	0.00005

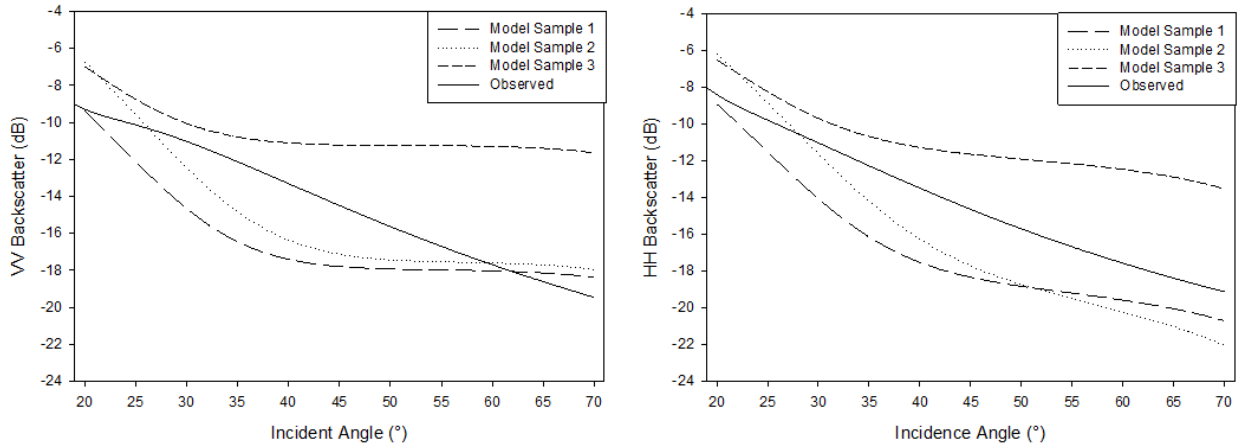

Figure 3.12. Comparison of Observed and Modeled (MSIB) C-Band Backscatter (σ°_{w}, σ°_{HH}) for Complexly-Layered Snow, Churchill, Manitoba 2009. Observed is a cubic trend line as in Figure 3.9 and Figure 3.10.

To investigate how backscatter may be spatially averaged, the modeled backscatter was averaged for snow Sample 1 and snow Sample 3, the two most diverse observations in all geophysical respects (i.e. end-members). The resulting backscatter provided a closer relationship to the observed backscatter (Figure 3.13: left and right). This indicates that the geophysical heterogeneity input to the model is a likely cause of model estimation errors when compared to observed backscatter. This argument is supported by the good agreement of the observed surface-based backscatter which integrated over an 8 m x 8 m footprint, with that of the RADARSAT-2 area (Figure 3.9 through Figure 3.11). This heterogeneity of snow properties may be more prevalent in complexly-layered snow covers when compared to simple snow covers, and may therefore, have greater effect on model output from limited in-situ snow sampling. This in turn may affect geophysical inversion and sea ice classification from backscatter models which use a spatially or temporally limited sample set of geophysical data input and/or validation.

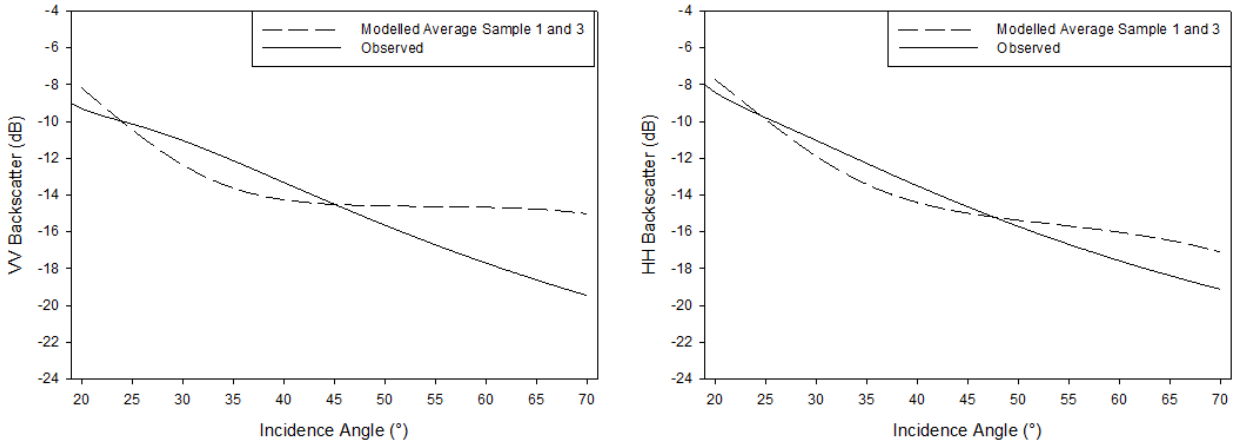

Figure 3.13. Comparison of Observed and Average Modeled (MSIB) C-Band Backscatter (σ°_w, σ°_{HH}) for Complexly-Layered Snow, Churchill, Manitoba 2009.

3.4.7 Modeled Analysis of Layer contribution

A sensitivity study is used to investigate the relative backscatter contributions of the complex snow layers (Figure 3.14). Various configurations of the Sample 2 snow cover are used, as this snow cover most consistently had the mid-snow pack ice layer and the superimposed ice layer at the sea ice interface (Table 3.4). Model runs are for: 1) "No ice layers"; 2) "Mid ice layer only"; 3) "Superimposed ice layer only"; and 4) "All layers". For comparison, observed backscatter from a simple snow cover on similarly smooth FYI is included. The simple snow cover observations were obtained with the same scatterometer near Resolute, Nunavut, in 2006. The simple snow cover is 21 cm thick and is conceptualized in Figure 3.3. The averaged observed backscatter from the complexly-layered snow cover is also included. The model runs generally fall between the observed backscatter for simple and complexly-layered snow on first-year sea ice.

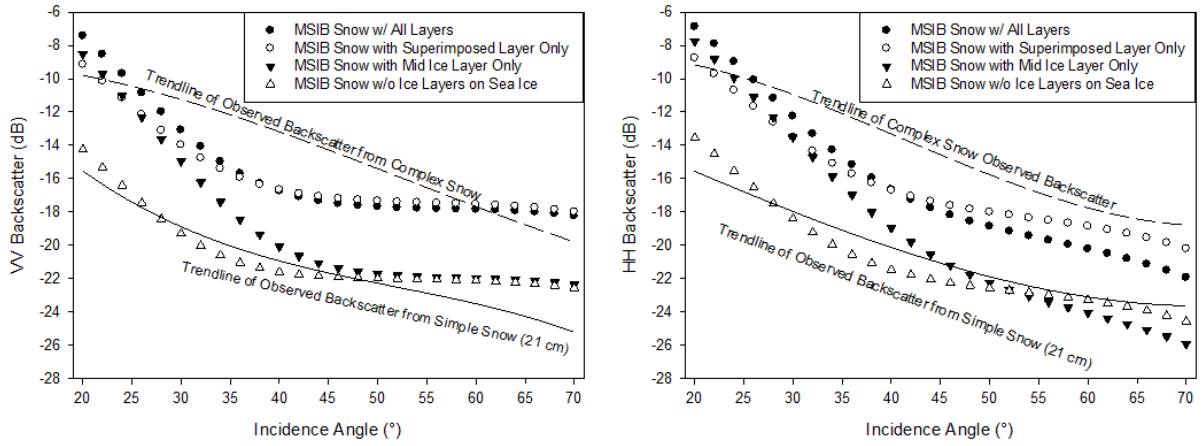

Figure 3.14. MSIB model ($\sigma°_{VV}$, $\sigma°_{HH}$) of 1155h complex snow cover, with and without ice layers present. Comparison with observed Sample 2 Complexly-Layered 24 cm (Churchill 2009) and observed Simple 21 cm (Resolute 2009) snow cover.

Table 3.4. Model inputs for Layer Contribution Comparison using Sample 2.

		No Layers				Superimposed Only		Midlayer Only		All Layers	
LyrID	Thick	Dens	Temp	Sal	Grain(m)	Dens	Grain(m)	Dens	Grain(m)	Dens	Grain(m)
13	0.02	0.349	-3.9	0	0.0005	0.349	0.0005	0.349	0.0005	0.349	0.0005
12	0.02	0.269	-4.3	0	0.0005	0.269	0.0005	0.269	0.0005	0.269	0.0005
11	0.02	0.266	-4.6	0	0.00025	0.266	0.00025	0.266	0.00025	0.266	0.00025
10	0.02	0.242	-4.7	0	0.00025	0.242	0.00025	0.7	0.00025	0.7	0.00025
9	0.02	0.218	-5	0	0.00025	0.218	0.00025	0.218	0.00025	0.218	0.00025
8	0.02	0.29	-5	0	0.00025	0.29	0.00025	0.877	0.00025	0.877	0.00025
7	0.02	0.362	-5	0	0.00075	0.362	0.00075	0.362	0.00075	0.362	0.00075
6	0.02	0.358	-4.8	0	0.0001	0.358	0.0001	0.358	0.0001	0.358	0.0001
5	0.02	0.401	-4.8	0	0.0005	0.401	0.0005	0.401	0.0005	0.401	0.0005
4	0.02	0.445	-4.5	0	0.00075	0.445	0.00075	0.445	0.00075	0.445	0.00075
3	0.02	0.383	-4.5	0	0.0005	0.383	0.0005	0.383	0.0005	0.383	0.0005
2	0.02	0.383	-4.3	0.2	0.001	0.88	0.001	0.383	0.001	0.88	0.001
1	0.02	0.383	-4.1	4.8	0.0005	0.88	0.00005	0.383	0.0005	0.88	0.00005
0	0.05	0.88	-4.1	6.4	0.00005	0.88	0.00005	0.88	0.00005	0.88	0.00005

3.4.7.1 Modeled σ^0_{HH} and σ^0_{VV} Contribution to Backscatter

The σ^0_{HH} "Snow on Sea Ice - No Layers" model run agrees well with the Resolute 2006 observed backscatter for a 21 cm thick simple snow cover. This suggests that the Churchill 24 cm snow

cover would exhibit the expected low backscatter of smooth FYI in the absence of the mid and superimposed ice layers.

Adding the mid-snow pack ice layer, through the "Mid Layer Only" model run, causes up to a 5.5 dB (σ^0_{HH} and σ^0_{VV}) increase at 20° incidence angle, which declines to a -2dB σ^0_{HH} decrease at 70° incidence angle (0 dB σ^0_{VV} at 55° incidence angle). This indicates that the high density, small grain size, and rough but weak dielectric mismatch of the mid-snow pack ice layer may affect backscatter at small incidence angles.

The addition of the rough Super-imposed ice layer and removal of the Mid Ice Layer (Super Imposed Layer Only) also increases backscatter at incidence angles < 30°; but not more so than the Mid layer only scenario. However, at incidence angle > 30°, the Superimposed ice layer displays up to 4 dB greater backscatter than for the Mid Layer only and No Ice layer scenarios. This increase is caused by both greater surface and volume scattering. The greater surface scattering originates from the large dielectric mismatch at the superimposed ice interface, given its high density and salinity; and the greater volume scattering also originates from the superimposed ice layer, again due to the high density and salinity.

The All Layers model run is a parameterization of the snow pack including both the Mid and Superimposed layers. The All Layers run results in up to a 2.4 dB increase in backscatter for incident angles less than 45°, and a backscatter loss of up to 2 dB for σ^0_{HH} (up to 0.09 dB σ^0_{VV}) for incidence angles greater than 45°, when compared to the Super Imposed Layer Only model run.

3.4.7.2 Layer Contribution

The model runs indicate that with both the mid-snow pack and superimposed surface ice layer, the results agree well with observed backscatter for complexly-layered snow, and that when both of these layers are replaced with the properties of adjacent snow in the model, the model results agree well with that of a simple snow cover. The model suggests that the superimposed ice layer contributes the most to the observed backscatter increase. However, the model also suggests that even in the absence of a superimposed ice layer, the mid snowpack layer would cause a significant increase in backscatter at C-band at small incidence angles when compare to that of a simple snow cover with no Mid Ice layer.

3.5 Discussion

The frequency, incident angle, and polarization dependent manipulation of microwave energy by brine, leading to snow cover thickness and snow water equivalent estimates, enables the linkage of microwave response to thermodynamic models required to parameterize snow and sea ice energy balance in climate modeling (Barber and Thomas 1998). The expected increase rain occurrence in events both later in the fall and earlier in the spring season (Trenberth et al. 2007), may seal significant quantities of brine under a freshwater ice layer within the snowpack, or against the sea ice interface. This can cause subsequent snowfalls on the superimposed ice layer to be relatively brine free and complexly-layered.

Earlier in the study season, brine had been present in the lower depths of the snow pack, as is typical; however, a rainfall event melted the snow pack and sealed the brine to the sea ice under a discontinuous and rough, superimposed ice layer up to 4 cm thick. Therefore, brine was less available to be introduced into subsequent snow falls through normal capillary-wicking

processes. The variation in snow salinity may have been due to spatial variation associated with the discontinuous fresher ice layer superimposing the sea ice interface. When a high permittivity brine layer is present, surface and volume backscatter can increase due to brine coated depth hoar grains, and penetration depth decreases as brine is a lossy medium (Nghiem et al. 1995a).

A rough, discontinuous, and less saline superimposed ice layer directly above smooth first-year sea ice, likely reduced microwave attenuation that is typical of the saline first-year sea ice, as the superimposed ice allowed only for a relatively thin layer of brine wetted snow to form within the depth hoar layer. This may cause difficulty in geophysical inversion and snow and sea ice mapping and classification based on backscatter, with assumed average snow grain sizes, densities, and brine volumes. Sea ice classification may also be confused as the backscatter values seen in the complexly-layered snow over smooth first-year sea ice are close to those of multi-year ice (Nghiem et al. 1995b).

This is reinforced by the model, and strengthens the case for increased surface and volume backscattering from complexly-layered snow, relative to simple snow, which is potentially a result of dielectrically rough, inconsistent, and relatively fresh, superimposed ice layer at the sea ice interface. According to the model, rough dielectric mismatch between the minimally brine wetted snow, and the superimposed ice at the base of the snow pack, reduced penetration depth enough so that the incident signal does not experience loss or reflectance from the greater, smooth dielectric mismatch of the brine at the sea-ice interface and below. This appears to result in increased surface and volume scattering from the rough and varied snow, inclusions, polyaggregate, and superimposed ice layers, which have a weak but rough dielectric mismatch, to cause increased scattering. At lesser incident angles (surface scattering), the Mid Ice layer

appears to increase backscatter to values greater than that which would occur from the Superimposed Ice layer alone. At greater Incident angles (volume scattering), the Mid Ice layer may be absorbing more signal as it passes through a relatively thicker ice layer, when compared to lower incidence angles, due to the incident angle itself, causing the lower dB values at greater angles. This is compared to loss and reflection that results from very smooth first-year sea ice surface, with a relatively greater dielectric mismatch which occurs in the case of simple snow.

3.5.1 What are the observed geophysical characteristics and C-band backscatter signatures for a complexly-layered snow cover on first-year sea ice?

For complexly-layered snow, the brine and density values, which affect dielectric and thermodynamic properties, differ from that of simple snow. The mid snow pack ice layers increases density above typical values, and the superimposed ice layer serves to diminish the amount of brine in the depth hoar at the snow ice interface by about half, when compared to that of a typical simple snow cover. For complexly-layered snow on smooth first-year sea ice, the observed magnitude of σ^0_{VV}, σ^0_{HH}, and σ^0_{HV} is greater than for a simple snowpack of equal depth; more closely mimicking that of rough FYI, or even multi-year ice.

3.5.2 How do observed and simulated C-band backscatter compare for a complexly-layered snow cover over first-year sea ice?

Model results show good agreement with the observed backscatter when spatial heterogeneity is accounted for through averaging. The averaged model results overestimate backscatter (more pronounced for σ^0_{VV}) at incident angles greater than 55°.

3.5.3 How do the components of a complexly-layered snow pack over first-year sea ice contribute to C-band backscatter?

The model runs indicate that with both the mid-snow pack and superimposed surface ice layer, the results agree well with observed backscatter for complexly-layered snow, and that when both of these layers are replaced with the properties of adjacent snow in the model, the model results agree well with that of a simple snow cover. The model suggests that the superimposed ice layer contributes the most to the observed backscatter increase, and that even in the absence of a superimposed ice layer, the mid snowpack layer would cause a significant increase in backscatter at small incidence angles, when compared to a typical simple snow cover.

3.6 Conclusions and Implications

An expected increase in the timing and magnitude of late winter season and freezing rain events in the high Arctic, can seal brine under freshwater ice and can create inter-snowpack ice layers, resulting in relatively brine free and complexly-layered snow covers on first-year sea ice. The reliance on microwave signal return for geophysical inversion and sea ice classification, becomes less reliable when considering complexly-layered snow covers. Scattering from ice layers, ice inclusions, rough interface layers, and a heterogeneous array of snow crystal shapes and sizes throughout the volume may mask typical backscatter and loss signatures associated with brine-wetted depth hoar and smooth sea ice layers below.

Generally, snow packs are parameterized as a homogeneous medium with a smooth gradient of crystal sizes and an average density of 0.250 to 0.300 g cm^{-3} in order to populate inversion models. With more precipitation falling as rain both later at the beginning of the winter season and earlier at the end of the winter season, modeling must include complexly-layered snow pack

scenarios, which do not necessarily exhibit typical two-layer simple snow structure organization, crystal size and density values, brine values and distributions, or surface roughness.

The mid snow pack layering, densification, and general lack of brine within the snowpack has implications for sea ice classification particularly with regard to FYI and MYI discrimination, and also has potential modeling and real world implications for melt timing and melt rate of first-year sea ice. The superimposition of rough, relatively fresh ice over first year sea ice, has implications for microwave backscatter response, as snow dielectrics are affected though hindrance of brine wicking. The differences in backscatter signatures for complexly-layered and simple snow are likely due to dielectric permittivity and loss variations, associated with different brine and density profiles in the snow pack. This may have implications for geophysical retrieval and classification strategies that are based on microwave backscatter. Future work (presented in Chapter Five:) will focus on development of an assimilation technique using both snow and microwave models for geophysical inversion, in order to better differentiate complexly layered snow from rough FYI and Multi-year Ice for classification, hydrologic, and climate modeling purposes.

Chapter Four: **Plot Scale Passive Microwave Measurements and Modeling of Layered Snow**

4.1 Abstract

The excavation of snow layers was used to compare observed and modeled plot-scale brightness temperature (TB) values for 19 and 37 GHz, with regard to snow water equivalent (SWE), snow type, grain size, and layered structure, for 3 land cover types acquired near Churchill, Manitoba, Canada in March of 2010. In-situ snow geophysical measurements were input to the Helsinki University of Technology (HUT) multi-layer snow emission model and performance was characterized by RMSE and MBE. Emission scattering from depth hoar was disproportionate to its SWE contribution when compared to other snow types, and also masked observed scattering contributions from upper snow layers. The simulated and observed TB diverged above 130 mm SWE, as the model did not capture scattering extinction or snowpack emission. These may impact the initial effective grain size optimization process if applied to the GlobSnow SWE assimilation technique. Grain size is optimized to fit emission simulations to TB from satellite observations; the model's continued sensitivity to SWE above observed signal saturation may be attributed to the existing snowpack. These inaccuracies may then by carried forward in the assimilation process, through variance calculations use to weight the contributions of assimilation modules, leading to less accurate SWE retrievals.

4.2 Introduction

Snow water equivalent (SWE) is a measure of the hydrologic value of snow, and thus accurate SWE information is paramount to monitoring and inventorying water for hydrologic and climate applications (Jonas et al. 2009). However, snow properties exhibit great spatio-temporal variability (Chang et al. 1987a). The coarse spatial resolution of satellite-based radiometry for

SWE retrieval, necessitates the averaging of microwave emission over large areas consisting of heterogeneity in landcover and snow properties (Lemmetyinen et al. 2010). Uncertainty also stems from simplification of the complexly-layered nature of snow (Lemmetyinen et al. 2010; Rees et al. 2010) and from difficulties with parameterization of snow microstructure (Rutter et al. 2014; Lemmetyinen et al. 2015). These are required for input to snow emission models recently used in the state of the art SWE retrievals (Pulliainen 2006; Durand et al. 2008). Specifically, improved characterization of the effects of snow grain size and snowpack layering are required to address uncertainties in these retrievals (Pulliainen 2006; Durand et al. 2008; Lemmetyinen et al. 2010; Lemmetyinen et al. 2015). The purpose of this study is to compare snow emission model results to observations from an excavation field experiment conducted near Churchill, Manitoba (in March of 2010), in order to assess the effects of snowpack structure, snow type, snow grain size, and SWE contribution to passive microwave brightness temperature (TB). While layer removal experiments were previously employed to study brightness temperature variation and contribution associated with surface ice lenses (Rees et al. 2010; Montpetit et al. 2013), this work includes excavation of layers down to bare ground, and hence includes consideration of the relative contributions from depth hoar and wind slab layers. These results are interpreted within the context of the GlobSnow assimilation technique for the operational retrieval of SWE (Takala et al. 2011).

Snow cover stratigraphy varies seasonally in both the type and the sequence of layers. The stratigraphy of snowpacks affect snow cover characteristics through thermodynamic processes, as the snowpack matures over the course of a season (Colbeck and Jamieson 2001). Snow covers would be layered simply due to storm cycles throughout the winter. However, warming and

cooling periods, melt metamorphosis and refreezing, wind redistribution, snow loading and scouring, and changes in snow density through compaction add complexity to this layering (Wakahama 1968; Colbeck 1991). The layers, crusts, and ice lenses occurring in snowpacks can be discontinuous, with high spatial variation in both vertical and horizontal distribution and properties (Rutter et al. 2014). The presence of an ice lens or crust affects grain development both above and below the layer due to modification of the temperature gradient, airflow through the snowpack, subsequent melt-water drainage, and seasonal melt processes (Colbeck 1991). This causes further complexities in snow grain morphology, depth, density, SWE, and dielectric properties, which are specifically of interest in the interpretation of microwave remote sensing data.

SWE retrievals based on the attenuation of microwave emission from the ground by snow (measured by radiometers as brightness temperature) show a consistent underestimation of SWE for deep snowpacks (>~130 mm) and strong dependence on snow grain microstructure (Chang 1987a; Hall 1987; Hallikainen 1989; Derksen, LeDrew, Goodison 2000; Kelly et al. 2003). Frequency dependant saturation limits direct inversion for SWE greater than about 130 mm (De Seve et al. 1997), as further increases in SWE are no longer related to observed decreases in TB (Durand and Margulis 2006; Derksen 2008). There is a reversal in the 37 GHz response as the snow transitions from a scattering medium to an emitting medium between 120 mm and 180 mm SWE (Schanda et al. 1983; Matzler 1994; Derksen 2008). This adds confusion to SWE retrieval as a single brightness temperature value will represent two or more snow conditions separated by over 100 mm SWE (Schanda et al. 1983; Matzler 1994; Derksen 2008). Single-layer SWE inversion models which rely on differences or ratios of multiple frequencies (19 GHz – 37 GHz),

encounter additional error through averaging of heterogeneous snow properties such as stratigraphy and microstructure. Therefore, the overall response of TB to snow cover lies not in the simple averaging of snow properties, but lies in the properties of each layer and the sequence of the layers themselves (Colbeck 1991). The importance of layering in snow led to development of multilayer microwave emission models based on radiative transfer, such as MEMLS (Wiesmann and Matzler 1999; Matzler and Wiesmann 1999), DMRT (Tsang et al. 1985; Tsang 1987), and the multiple-layer modification for the Helsinki University of Technology (HUT) model (Pulliainen et al. 1999; Lemmetyinen et al. 2010).

Studies employing the multiple-layer HUT model have demonstrated up to a 38% improvement in model accuracy (Lemmetyinen et al. 2010) and a 50% reduction in bias (Rutter et al. 2014) when compared to the single-layer HUT model (e.g. 37 GHz); however, these also noted reduced performance for lower frequencies (e.g. 19 GHz) (Lemmetyinen et al. 2010). When simulating a relatively simply-layered and homogenous snow cover, the greatest improvement in model performance came with the first additional layer (Lemmetyinen et al. 2010; Rees et al. 2010). Larger differences in the properties of adjacent snow layers (e.g. grain size) resulted in better performance for the multi-layer simulations when compared to those of the single-layer model runs. There is particular importance in considering proportions of depth hoar and wind slab in the model, with regard to grain size and its effect on the extinction coefficient, as these are not linearly related (Derksen et al. 2014; Lemmetyinen et al. 2015). A two-layer hut simulation improved performance over the single-layer model at 19 and 37 GHz, but only when employing an empirical scaling relation (Kontu and Pulliainen 2010). This restricts the maximum observed grain size to <1.6 mm in order to mute the effects of larger observed grain sizes typically

occurring in depth hoar (Lemmetyinen et al. 2015). The modeled effective grain size had some relation to observed physical grain size for well controlled cases, which is important to accurate regional-scale microstructure parameterization for SWE inversion. Error was also attributed to the soil roughness and dielectric parameterisation, and several optimization solutions were attempted with mixed results (Lemmetyinen et al. 2015).

The assimilation method, developed by Pulliainen (2006), fits a single-layer HUT radiative transfer model to satellite TB measurements using snow depth measurements from available weather stations. This retrieval method is operationally employed in the European Space Agency's Globsnow project (www.globsnow.info), and has recently been used to produce a long term climate record (Takala et al. 2011). The assimilation technique considers the non-linear sensitivity of TB to SWE, and weights contribution from individual components adaptively with the statistical inaccuracy of those components (Pulliainen 2006). Use of this assimilation technique has resulted in RMSE values of 15 mm to 40 mm SWE, for snow depths less than ~100 cm and SWE less than ~150 mm. It has also reduced systematic error when compared to direct TB inversion as saturation occurs when SWE $\gtrsim$ 130 mm, and when compared to interpolation of synoptic weather station observations (Pulliainen 2006; Takala et al. 2011). A description and validation of the GlobSnow assimilation employing a single-layer HUT radiative transfer model is available in Lemmetyinen et al. (2010) and Takala et al. (2011).

While single-layer radiative transfer models are employed in operational snow assimilation programs (e.g. GlobSnow) multiple-layer adaptations have been evaluated (Durand and Margulis 2006; Pulliainen 2006; Durand and Margulis 2007; Durand et al. 2008; Lemmetyinen et al. 2010; Takala et al. 2011; Durand et al. 2011; Lemmetyinen et al. 2015). The multiple-layer radiative

transfer models which invert SWE from satellite TB values remain constrained by previously noted sensitivity to grain size, snow layering, and saturation effects. These lead to inaccuracies particularly for deep and/or late season snow, which typically exhibits increased metamorphic and spatial heterogeneity. This has resulted in the development of data assimilation techniques such as the ensemble Kalman filter (EnKF) (Sun et al. 2004; Durand and Margulis 2006) and that employed in the ESA GlobSnow project (Pulliainen 2006; Takala et al. 2011). The assimilation of a snow/land radiative transfer model, updated with available physical and remote sensing observations, gives some freedom from site and scale restrictions, and allows for an accounting of statistical uncertainties associated with model state variables (Durand and Margulis 2006; Pulliainen 2006; Durand and Margulis 2007; Takala et al. 2011). These have led to significant improvements in the accuracy of SWE retrievals, when compared to direct inversions, and assimilations employing single-layer radiative transfer models. However, the lack of consideration of stratigraphy information in assimilations still leads to significant error (Durand et al. 2011; Toure et al. 2011).

This paper presents 19 and 37 GHz dual-polarization microwave brightness temperature measurements, acquired through a sequential layer by layer excavation experiment (from undisturbed snow to bare ground) for comparison with multi-layer HUT snow emission model simulations. The objective is to characterize the contributions of various snow layer types (e.g. fresh/recent snow, wind slabs, ice crusts, depth hoar) to the observed and simulated TB, for complexly-layered snowpacks over several subarctic landcover types (i.e. forest, fen, drifts). These are considered within the context of application of the single- or multi-layer HUT model in the GlobSnow assimilation technique.

4.3 Methods

4.3.1 Study area and sites

Churchill, Manitoba (Lat. 58°N, Long. 94°W) is situated in a low-elevation low-relief wetland area in the High Subarctic ecoclimatic zone on the western coastal region of Hudson Bay. It is characterized by the transition zone between tundra and boreal forest (Pivot et al. 2002). Field measurements were acquired 23 km east of Churchill, in forest, fen, and drift sites over the winter of 2009-2010 (described fully in Derksen et al. (2012)) (Figure 4.1). In March 2010, ground-based multi-frequency (19 GHz, 37 GHz) dual-polarization (vertical V, horizontal H) microwave radiometer measurements were made of the undisturbed snow cover, and repeated as individual layers were sequentially removed from the snowpack. The radiometer system is described in Derksen et al. (2012). Individual layers were manually removed based on the visual identification of snow layers (snow density, snow grain size, the presence of ice crusts), with microwave measurements made after each layer was removed. The excavation continued successively in this fashion until the bare ground interface was exposed.

Figure 4.1. Left: Churchill study area sample sites (Map courtesy of P. Toose, Environment Canada). Right: Mobile radiometer system.

4.3.2 Microwave data

The mobile dual-polarized passive microwave remote sensing radiometers measured emission at 19 GHz and 37 GHz in vertical and horizontal polarizations, and were calibrated every 2-5 days using cold point (LN2) and warm point (Echosorbe) targets (Table 4.1). A non-linear, multi-iterative process developed by Radiometric Inc. was used to derive the final calibration coefficients for the conversion of measured voltages to brightness temperature. These are described fully in Derksen et al. (2012).

Table 4.1. Radiometer specifications.

Frequency (GHz)	19	37
Bandwidth (MHz)	1000	2000
Sensitivity (K)	0.04	0.03
Accuracy (K)	< 2	< 1
Antenna Beam Width (°)	6	
Look Angle (°)	53	
Spatial Footprint (m)	0.6 x 0.6	

4.3.3 Snow sampling

Measured snow parameters were used as inputs to the multi-layer HUT model for comparison to measured TB. The snow properties were manually sampled along the non-illuminated face of snow pit, so as to minimize solar contamination and metamorphosis of the snow crystals during sampling. Density was sampled every 5 cm vertically in the snowpack using a standard 100 cc density cutter and weighed using a hanging scale (±1% of sampled weight). Characterization of layering within the snowpack was conducted through visual and physical interpretation of the snow pit sampling face. Snow temperature measurements (±0.2°C) were sampled at 2 cm intervals through vertical profile of the snow pit and were taken next to the density samples. Permittivity was also measured at 2 cm intervals using a Toikka snow fork (500 MHz – 900 MHz; e′ 1.5%, e″ 1.5%) (Tiuri and Shivola 1986). Measured snow grain specific surface area (SSA), later converted to optical grain size, was sampled every 5 cm vertically through use of an InfraRed Integrating Sphere (IRIS) (Gallet et al. 2009; Monpetit et al. 2012). This measured hemispheric reflectance at 1330 nm. Directionally lit snow grain photography employed LEDs to illuminate approximately 20 snow grains, for three-dimensional (3D) modeling of individual snow grains, sampled every 5 cm depth in the snowpack. The cardinal-directional lighting of the

grains by the LEDs, allows for digitized results to quantify grain dimension (axis, eccentricity, projected surface, and specific surface area) for each layer, as described in Derksen et al. (2012).

4.3.4 Multi-layer HUT simulations

The semi-empirical HUT model is a snow emission model for frequencies between 5 GHz and 90 GHz, which assumes only forward scattering and incoherent emission. The empirical scattering (ks), absorption (ka) and extinction (ke) coefficients are a function of grain size, dielectrics, and frequency (Hallikainen et al. 1987). The multiple-layer modification is a two-flux (up- and downwelling) approximation of each layer, with Lambertian interfaces between layers and at the snow-air interface. The multiple layer adaptation of the HUT model allows for the parameterization of multiple snow and ice layers, each with varying physical properties (Lemmetyinen et al. 2010). The transmission at layer interfaces is represented by Fresnel coefficients, with reflection represented by a loss factor determined by attenuation through ka, ks, and ke formulae. The summation of the layered upwelling emission at the snow-air interface gives the emission leaving the snowpack. The HUT model and its inputs are fully described in Pulliainen (2006) and Lemmetyinen et al. (2010).

The input layers to the multi-layer HUT model matched the observed excavated layers, which were taken from measurements of layer thickness, temperature, density, SWE, and grain size. A simple layer thickness weighting related all observed snow properties to the values used for input to the multi-layer HUT model, consistent with Lemmetyinen et al. (2015). The direct downwelling sky and tree emission contribution is assumed to be relatively constant over the course of time required for each snowpit excavation, and was not taken into account. As per Monpetit et al. (2013), the downwelling and tree emissions contributed primarily to coherent

emission intensity with interactions pertaining to ice lenses. As previously noted, the HUT model does not consider coherent scattering; however, this remains a potential source of error. Additional error may stem from downwelling emission caused by emission from the snow itself being reflected back to the radiometer by trees surrounding the open sample areas. This can vary with the removal of snow layers, and so remains a potential source of uncertainty. The mean grain axis measurements from the 3D LED system and optical radius measured by IRIS system, were averaged together for each layer to create an 'observed grain size' for input to the multi-layered HUT model (Kontu and Pulliainen 2010; Derksen et al. 2012; Rutter et al. 2014). However, there were no 3D LED measurements acquired for the fen sites. A linear relationship between the IRIS and 3D LED grain diameter, for the forest and drift sites, was used to derive the observed grain size values for the fen sites. The grain sizes required to match the simulated to the observed 37V TB were also derived, holding all other parameters constant, for empirical extinction coefficients developed by (Hallikainen et al. 1987) (grain diameter < 1.6 mm) and by Roy et al. (2004) (grain diameter > 1.6 mm). Leppanen et al. (2015) provide an accounting of the error for measured and IRIS SSA derived optical grain size values, in comparison with SNOWPACK simulations, and show the potential error is generally greatest for depth hoar. Kontu and Pulliainen (2010) and Rutter et al. (2014) provide a further comparison of grain size scaling factors, extinction coefficients, and associated error with regard to HUT model simulations. The grain size parameterization used in this work was chosen as an objective "middle ground" solution between the classical measured grain size, and the more recent SSA derived grain size (Derksen et al. 2012). We acknowledge that uncertainty due to the treatment of snow microstructure will impact the microwave simulations, due to the specific nature of many of the grain size parameterization choices currently available, which are described more

fully in other studies (e.g. Wiesmann and Matzler 1999; Matzler and Wiesmann 1999; Pulliainen et al. 1999; Pulliainen 2006; Kontu and Pulliainen 2010; Rutter et al. 2014; Leppanen et al. 2015). The surface roughness (3 mm) and dielectric constant for the ground layer (6-j) were fixed for all sites, consistent with other studies (Derksen et al. 2012; Lemmetyinen et al. 2015).

4.4 Results

The complexly-layered March snowpack was a result of precipitation events primarily in December and January, with temperatures of -15°C to -30°C through to March (Derksen et al. 2012), driving kinetic snow grain metamorphosis. Several melt events in March, caused by anomalous temperatures nearly 25°C above normal, created melt/freeze ice crusts with high spatial variability both vertically and horizontally (Derksen et al. 2012; Rutter et al. 2014). The focus of analysis was measurements from 9 sites (3 forest, 2 fen, and 4 drift), with the snowpack at each site composed of between 4 and 7 layers.

4.4.1 Site overviews

The three sampled forest sites had similar snow depths, ranging from 57 to 61 cm. The forest snowpacks contained no wind slab due to the sheltering effect of the forest vegetation. Sampled SWE totals ranged from 168 to 197 mm. The measured IRIS and 3D grain sizes for these sites ranges from a minimum of 0 .1 mm (IRIS) in the upper layers, to a maximum of 6.5 mm (3D LED) for depth hoar lower in the snowpack (Figure 4.2). This resulted in an averaged observed grain size ranging from 1.3 to 3.7 mm through the snowpack for input to the model. The two sampled fen sites were the shallowest of the snowpacks (49 and 50 cm) due to long fetches and scouring by wind transport above vegetation height. The fen sites held an average of 196 mm of SWE. The snow at the fen sites was comprised of depth hoar and wind slab. The IRIS SSA

measurement was converted to optical grain sizes ranging from 0.3 to 0.6 mm. The grain size for the fen site was modeled from a relationship between the IRIS and 3D LED grains for the forest and drift sites ($n = 20$, $R^2 = 0.82$). This resulted in 3D led grain sizes ranging between 2.4 and 3.9 mm, and average observed grain sizes of 1.4 to 2.3 mm (Figure 4.3) which were employed to drive the HUT simulations. The deepest sampled snow was accumulated in topographic depressions, creating the four drift sites. The snow depth at the sampled drift sites ranged from 70 to 180 cm, with SWE ranging from 280 mm to 720 mm and averaging 471 mm. The drifted snowpack was composed of large grained depth hoar, high density wind slab, and recent fresh snow at the surface. Measured IRIS and 3D grain size ranged from 0.6 to 4.9 mm, and resulted in an observed grain size ranging from 0.5 to 3.5 mm (Figure 4.4) for input to the model.

4.4.2 Multi-layer HUT performance

The observed and simulated TB were compared by excavated layers, and model performance was characterized by root mean square error (RMSE) and mean bias error (MBE) (Table 4.2). This was done for the undisturbed snow pack, and for aggregated snow layers for SWE greater and less than 130 mm. The simulations show reasonable agreement with observed TB for the vertical polarization when compared to the horizontal polarization, which are sensitive to snow volume and snow structure, respectively (Hall 1987; Matzler 1994; Rees et al. 2010). These values are in the range found in previous studies (Lemmetyinen et al. 2010; Kontu and Pulliainen, 2010; Rees et al. 2010; Rutter et al. 2014). In all cases, the 19 GHz RMSE is lower than that of the 37 GHz, which is at least partially indicative of the relative insensitivity of 19 GHz emission to dry snow conditions. The unique layered-excavation and TB observation process resulted in reversal of the 37V TB emission occurring on average at the 130 mm SWE

threshold, which agrees well with previous non-excavation based studies carried out over similar landcovers (Matzler 1994; Derksen et al. 2010; Lemmetyinen et al. 2015). The RMSE and MBE for less than 130 mm SWE improves for all configurations, when compared to that greater than 130 mm SWE (Table 4.2). This indicates that the observed and simulated TB show better agreement for the lower layers of the snowpack, which is comprised primarily of large grain depth hoar (Figure 4.2 through Figure 4.4). This is due to the failure of the simulation to capture the typical 37 GHz reversal of the observed TB, as evident in the increased absolute MBE for SWE greater than 130 mm. As the observed TB begins the reversal to increased TB values with additional SWE, the multi-layer HUT model continues to predict decreased TB values, and exhibits continued sensitivity to additional SWE. This is a consistent error which others have attributed to the empirical extinction coefficient and to the sensitivity of the model to effective grain size (Rees et al. 2010; Kontu and Pulliainen 2010; Rutter et al. 2014).

Table 4.2. Vpol and Hpol (T_B, K) comparison (RMSE, MBE) for forest, drift, fen sites for greater and less than the 130 mm SWE level in the snowpack.

	V19 RMSE	V19 MBE	V37 RMSE	V37 MBE	V19-37 RMSE	V19-37 MBE	H19 RMSE	H19 MBE	H37 RMSE	H37 MBE	H19-37 RMSE	H19-37 MBE
Forest	8.6	7.6	26.6	16.1	21.7	-8.4	18.0	11.1	32.0	23.2	28.1	-12.2
SWE > 130 mm	8.7	8.6	37.4	37.2	28.9	-28.6	19.8	12.7	45.5	45.1	34.3	-32.4
SWE < 130mm	8.5	6.9	10.5	-1.3	12.1	8.2	16.0	12.6	13.2	5.6	11.3	6.2
Drift	11.9	6.9	52.0	37.8	44.0	-30.9	19.5	7.0	50.0	38.6	45.8	-31.6
SWE > 130 mm	12.0	6.1	62.1	61.3	56.0	-55.2	20.5	0.2	57.7	57.3	58.4	-57.2
SWE < 130 mm	7.7	5.2	16.9	7.1	15.2	-1.9	13.6	12.1	19.6	13.6	14.7	-1.5
Fen	11.4	-9.4	23.0	-12.8	7.4	6.7	12.8	-8.1	17.0	-8.2	3.8	3.4
SWE > 130 mm	12.6	-12.6	22.5	22.5	35.0	-35.0	22.4	-22.4	18.2	18.2	40.6	-40.6
SWE < 130 mm	10.3	-7.9	21.4	-20.6	14.6	12.7	7.0	-3.6	14.5	-13.7	12.3	10.1

4.4.3 Layered excavation of the snowpack

4.4.3.1 Forest

For the initial undisturbed snow packs, the simulations show decreased 37V T_B when compared to the observations. For the typified forest site (Figure 4.2), the simulation underestimates the

undisturbed condition by 28.7 K. As snow layers are sequentially removed from the forest site, the observed scattering contributions for the upper excavated layers show little change in measured T_B, and thus little sensitivity to removal of SWE. The observed 37V T_B for the typified forest site remains consistent at 172.6 (±2.5) K, even as 61 mm of SWE is removed through excavation of a surface ice layer, and a recent snow layer composed of rounded grains. Conversely, the multi-layer HUT simulations show sensitivity to the same SWE removal, with a decrease in 37V T_B of 31.8 K. The excavation of a mid-pack ice crust and depth hoar (excavated in two layers) removed the remaining SWE (116 mm). There is good agreement between the simulations and observations for these excavations, particularly when SWE drops to less than 130 mm. These results also illustrate the relative insensitivity (less than 4 K) of both 19V and 37V observed and simulated T_B to each of the ice crusts, consistent with Rees et al. (2010). The amount of change in T_B exhibited by the model and observations for both 19V and 37V (Figure 4.2 Center Left), further demonstrate the difference in sensitivity of the HUT simulations and observations to SWE for the excavated snow layers. In these cases, the T_B difference can be thought of as the amount of change in emission as the layer above was excavated. For example, an upper and lower layer have a combined 37V T_B of 180 K at the snow-air interface, after the upper layer is removed the emission from the lower layer snow-air interface is 200 K. Thus the difference is 180 K - 200 K, or -20 K. Another way to interpret this in Figure 4.2 (Left) is that the absolute value of that change (i.e. |20|) is the change in 37V T_B emission as snow/SWE layers are added in upward succession. The two lower excavated layers of the snowpack, comprised of large grained depth hoar, demonstrate similar observed and simulated (in brackets) 37V T_B changes of -54 K (-47 K) and -25K (-30 K), respectively. Above 130 mm SWE, an average additional 0.85 K (37V) is simulated for each additional 1 mm of SWE, when considering all

sampled forest sites. This decrease does not match TB observations. The forest K mm^{-1} SWE rate is greater than those of other sites in this study because of the addition of SWE through high-density ice lenses. These were present in forest sites alone, and contribute relatively little change in vertically polarized TB, but contribute a large amount of SWE due to the higher density of ice relative to snow.

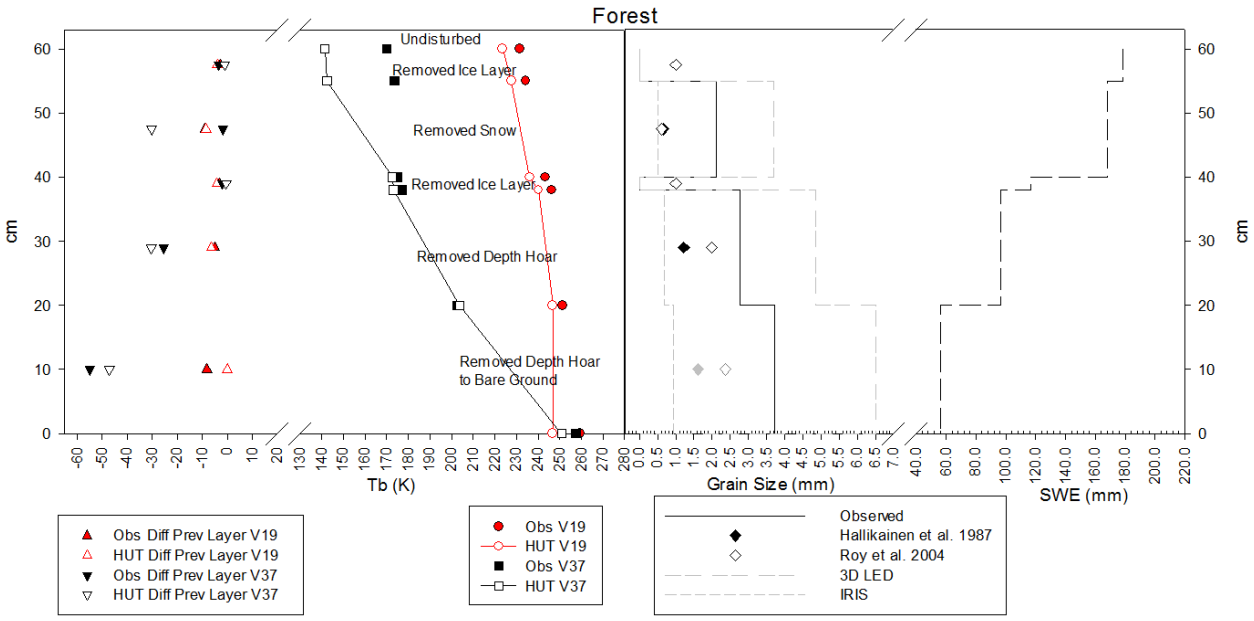

Figure 4.2. Typical forest snow site sample. Left: T_B Layer difference from the layer above (negative values indicate inclusion of the layer above exhibited increased T_B values). Center Left: observed and simulated T_B. Center Right: snow grain size. Right: SWE.

The observed grain size for the forest sites used to drive the HUT simulations are illustrated in Figure 4.2 (Center Right). Also depicted is the optimized grain size required by empirical extinction coefficients developed by Hallikainen et al. (1987) and by Roy et al. (2004) (developed for sizes greater than 1.6 mm). This was done to match the simulated 37V T_B to the observed, holding all other parameters constant. For all cases in this work, the required grain

sizes were achieved by adding individual snow layers with parameters from snow measurements, from the bare-ground successively upward, and matching simulated to observed 37V T_B by varying grain size only. For all cases, the initial grain sizes required at the bottom of the snowpack include both the difference in the observed and simulated 37V T_B for bare ground conditions and in the initial layer of depth hoar, in order to fulfill the requirement to have the simulations and observations match at each layer interface (designated with grey symbols in Figure 4.2 through Figure 4.4). Both extinction coefficients result in similar required grain sizes at diameters less than 1.6 mm, with greater separation for those larger than 1.6 mm. The extinction coefficient developed by Roy et al. (2004) for grain sizes greater than 1.6 mm, is generally closer to the observed grain size used to drive the simulations, when compared to the original Hallikainen et al. (1987) coefficient. For the forest site, the diameter of grains required to match the simulated TB to observed for an estimated ice crust density of 0.87 g cm^{-3} (Marsh and Woo 1984; Fuller et al. 2014), varies between 1 and 3 mm, which is similar to the observed grain sizes in the layers encompassing the ice lenses. The required grain size for both extinction coefficients agree above 130mm SWE because there is so little observed 37V T_B change required between layers, as the observed signal is saturated. Thus the required grain size to simulate these changes above saturation level is very small, which is observed for all cases in this work.

4.4.3.2 Fen

The undisturbed condition of the fen snowpack shows the 37V simulations underestimating observations by 15.2 K. The observed fen site emission shows behavior similar to the forest site, in that the initial observed 37V T_B remained almost constant at 165.5 K (±2.8), even as 102 mm SWE was removed through excavation of windslab (in 2 layers). The multilayer HUT

simulations show sensitivity to the removal with a 34.9 K increase in T_B. This difference causes the simulation to transition from underestimating to overestimating observed T_B values for the remainder of the excavations, to a maximum difference of 20.6 K for the final depth hoar layer. However, the general trend of difference in emission from the previous layer show reasonable agreement between observations and simulations below 130 mm SWE (Figure 4.3, Center Left). As with the forest site, the majority of observed and simulated change in T_B for the typified fen site is caused by the depth hoar (Figure 4.3, Left). Below 130 mm SWE (36 cm SD), simulated and the observed T_B differences, that occur with each snow layer, agree reasonably well for both 19V and 37V. Here the observed and simulated 37V T_B changes with the excavation of depth hoar layers by -30 K (-18 K), -20 K (-24 K), and -12 K (-13 K), respectively. Above 130 mm SWE the layered fen simulations depart from relative agreement with the observations, and the simulations show decreased T_B due to scattering averaging of 0.45 K mm^{-1}. The removal of the windslab at the 130 mm SWE level results in the observed 37V T_B layer difference becoming positive (Figure 4.3, Left) as extinction occurs with additional SWE. For all cases above the 130 mm SWE level, the model fails to capture signal saturation and extinction, and continues showing negative T_B differences (Figure 4.3, Left).

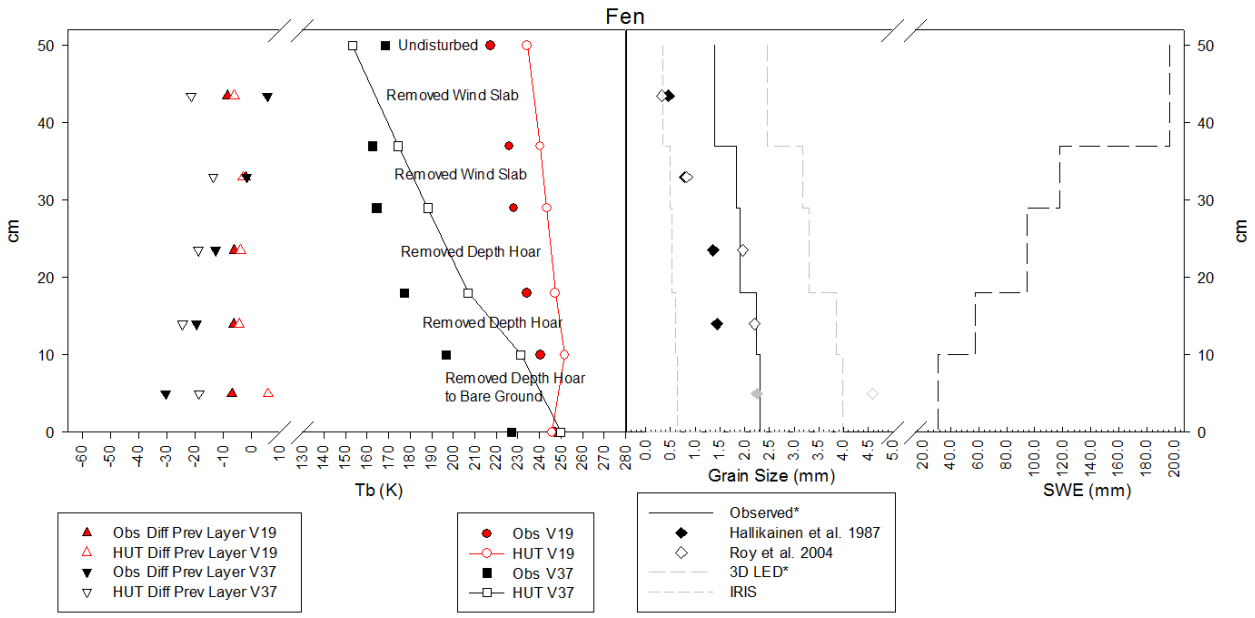

Figure 4.3. Typical fen snow site sample. Left: T_B Layer difference from the layer above (negative values indicate inclusion of the layer above exhibited increased T_B values). Center Left: observed and simulated T_B. Center Right: snow grain size. Note the asterisk indicating the grain sizes modeled from the relationship between IRIS and 3D grain sizes from other sites. Right: SWE.

For fen sites, the average RMSE and MBE of the observed and simulated T_B (Table 4.2) are in the range found by other studies. However, the consistent overestimation for both 19V and 37V by the simulation, particularly for SWE less than 130 mm (i.e. depth hoar), may be due to the method employed to find an observed grain size. The 3D grain size was estimated from the 3D-IRIS relationship for the drift and forest sites. While the R^2 is reasonable at 0.82, kinetic grain metamorphosis is modified by landcover effects on snowpack formation and weather events; therefore, physical differences in the grain sizes and shapes are part the cause of the uncertainty in the relationship. This uncertainty, which may cause part of the consistent overestimation for both 19V and 37V, suggests that a larger depth hoar grain size input to the HUT model would create more scattering and increase the simulated emission scattering and absorption and loss.

This would bring the simulations more in line with observations, particularly below the 130 mm SWE level. The RMSE and MBE indicate that while the grain size methods are not consistent with other cases in this work, the model performance remains consistent overall.

4.4.3.3 Drift

The undisturbed condition for the typified drift site (Figure 4.4) shows the largest difference between simulations and observations (49.7 K). As layers were excavated, the removal of recent fine surface grains (146 mm SWE) and windslab (64 mm SWE) caused a decrease in observed 37V (24.4 K), as the undisturbed snow pack itself was emitting radiation at that frequency. As the first layers of SWE were removed through excavation, scattering became the primary influence on emission from the ground, causing the changes in T_B. This occurs as the SWE decreases by 211 mm (to a total of 123 mm remaining) with excavation of the top 3 layers of snow, and as the snowpack transitions from an emitting medium to a scattering medium. The HUT model fails to capture this trend, and instead shows steadily increasing 37V T_B simulation values, which results in the model slightly overestimating the observations with removal of the depth hoar layers. The simulations show increased scattering, a -24 K difference (an average of 0.45 K mm^{-1} SWE for all drift sites above 130 mm SWE) due to additional SWE contributions (Figure 4.4, Center Left). As with the forest and fen sites, the drift sites show the excavated depth hoar layers at the base of the snowpack cause the greatest change in T_B for 37V observations and simulations, with -48 K (-45 K) and -25 K (-15 K), respectively (Figure 4.4, Left).

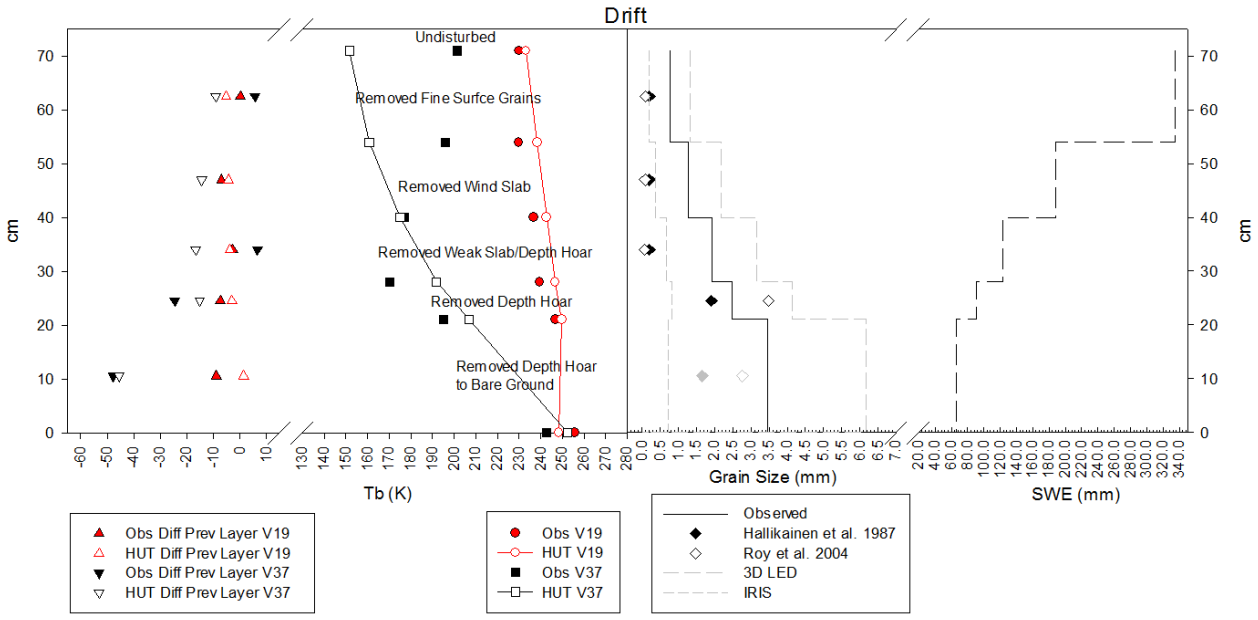

Figure 4.4. Typical drift snow site sample. Left: T_B Layer difference from the layer above (negative values indicate inclusion of the layer above exhibited increased T_B values). Center Left: observed and simulated T_B. Center Right: snow grain size. Right: SWE.

For all cases, the 19V emission shows an observed T_B decrease of between 15 K and 30 K (36 K and 87 K for 19H) through the layering, which is simulated well by the model (within an average of an 11 K decrease for all cases when comparing bare ground to full snow cover) and can be attributed to a small amount of scattering at this frequency (Lemmetyinen et al. 2015).

In summary, the excavation technique allows for a direct comparison of observed and simulated T_B as related to grain size, snow type, and SWE contribution for each bulk layer in the snowpack. Our process shows good agreement between the simulated and observed T_B for the depth hoar layers, which is reflected in the RMSE and MBE results below the 130 mm SWE level (Table 4.2). When SWE exceeds 130 mm, the simulations do not capture the behavior of

the observations. This is important when considering single or multi-layer simulations which rely on matching 37V T_B only at the snow-air interface.

4.4.4 SWE proportions and TB by snow type and layering

4.4.4.1 SWE proportions

The insensitivity of the observed 37V T_B measurements to SWE above the 130 mm level results in an inability of 37V T_B observations to account for in 37% to 72% of the measured snowpack SWE (Table 4.3). In the 3 forest sites the depth hoar holds an average of 63% (113 mm SWE), with the remaining 68 mm (37%) average SWE contributed by snow and ice crusts. The 2 fen sites held an average of 52% (102 mm) of total SWE above the 130 mm saturation level, and an average of 225 mm SWE (72% of total SWE) is present in the upper layers of the 4 drift sites. The plot excavation process demonstrates that there is a marked difference in the sensitivity of the simulated and observed 37V T_B centered about the saturation SWE level. The observed 37V is insensitive to SWE greater than the saturation level, which is masked by scattering from large grains of depth hoar and by emission from the snowpack (Matzler 1994; Lemmetyinen et al. 2015). Conversely, HUT simulations remain sensitive to the addition of SWE, and simulations fail to capture the saturation and extinction of the 37V signal shown in the observations. This results in underestimations of simulated 37V T_B at the snow-air interface.

Table 4.3. Average SWE contribution for snow type in percentage and mm by site class.

Sampled Sites	Depth Hoar	Wind Slab	Ice Crust	Recent Snow	Snow (Rounded Grains)	Average Sampled SWE
Forest %	63	0	18	0	19	100
SWE (mm)	114	0	33	0	35	181
Drift %	32	49	0	19	0	100
SWE (mm)	148	235	0	89	0	471
Fen %	48	52	0	0	0	100
SWE (mm)	95	102	0	0	0	196

4.4.4.2 Observed and simulated contributions of 37 GHz T_B with SWE by snow layer type

A direct comparison of 37 V and H T_B differences by snow type and SWE, through the layer excavation process, reveals the SWE and snow-type specific relationships between simulations and observations. The Top half of Figure 4.5 illustrates the change in 37GHz T_B by snow type with regard to SWE contribution (in this case snow type and SWE are aggregated from the excavated layers from the 3 forest sites, 2 fen sites, and 4 drift sites). The vertical and horizontal polarization observations and simulations are depicted in Figure 4.5 Left and Right, respectively. The Bottom half of Figure 4.5 illustrates the relationship between observed and simulated changes in 37GHz T_B with regard to snow type.

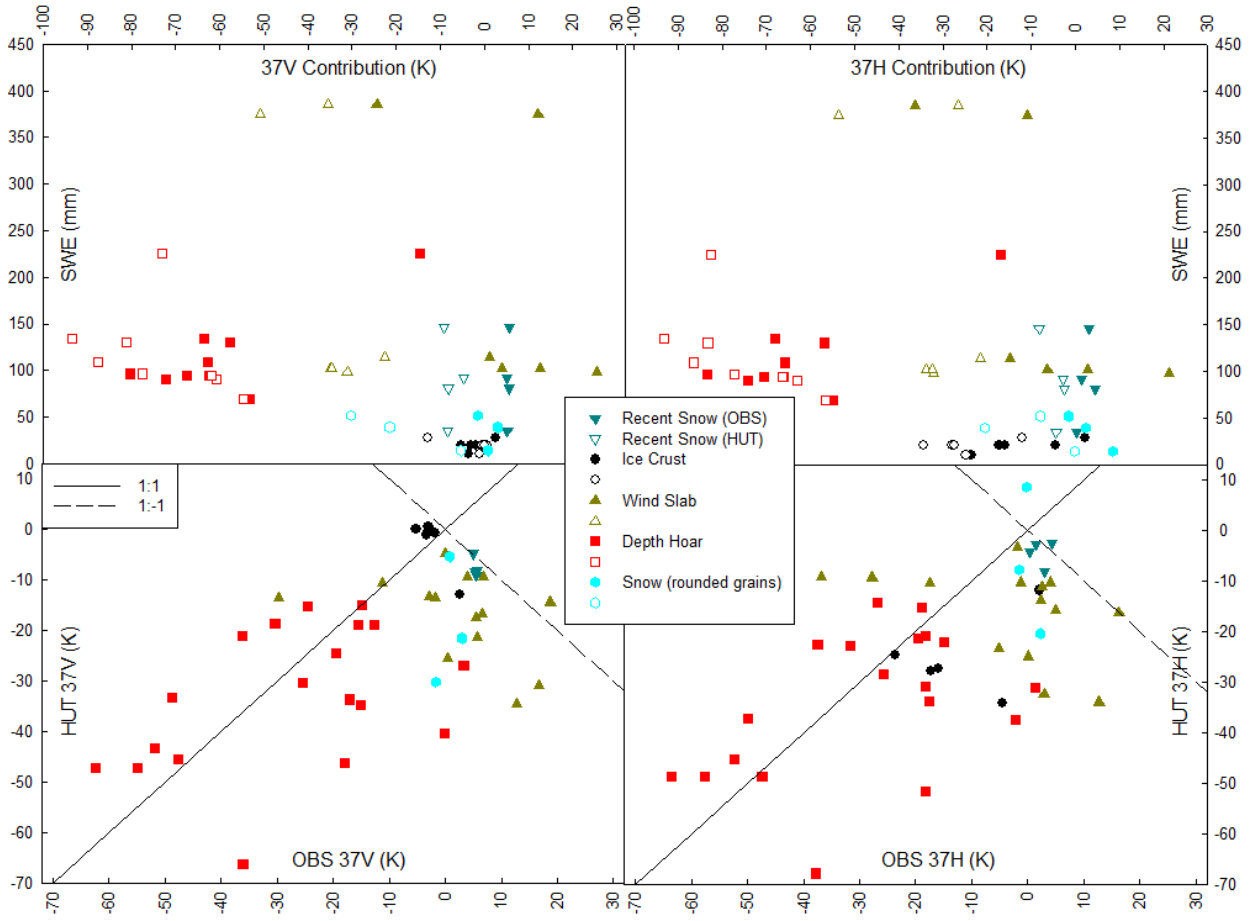

Figure 4.5. Top: Contribution of T_B by snow type for observations and simulations. As previously, in these cases the TB difference can be thought of as the amount of change in emission due to the addition of that snow type, and thus can be thought of as the T_B and SWE contributions by snow type. Bottom: T_B difference by snow type for Observed and HUT simulations.

The contribution of SWE by snow type in relation to 37 V and H T_B shows the strong sensitivity of the measurements to the depth hoar, and hence the importance of correctly modeling these layers (Figure 4.5, Top). The depth hoar causes greater change in 37V and 37H T_B, but it contributes roughly the same level of SWE when compare to other snow types. While the depth hoar represents a wide range of change in T_B (spanning about 75 K) for both 37 V and H observations and simulations, the SWE contribution associated with those changes is similar to

that from other snow types, which demonstrate less T_B difference. This is generally matched by the simulations with the exception of a few observations for the deepest drift sites, where the saturation level is reached in the lower 40 cm of the depth hoar. These 2 deepest of drift sites (SWE 540 mm and 720 mm) influence the agreement between simulations and observations (R^2 = 0.22 V, 0.22 H), as large volumes of depth hoar also occur above 130 mm SWE. The magnitude of change in scattering from depth hoar for observed 37GHz TB is over represented with regard to the SWE contribution, particularly when compared to that of other snow types. Thus, the primary observed scattering signature for snow is contributed only from the depth hoar layers.

The ice crusts contribute relatively little change in both SWE and 37V T_B, when compared with other sources, and the simulations agree relatively well (R^2 = 0.84). The 37H T_B demonstrates increased sensitivity to ice crusts as expected; however, the simulations exhibit more change (-10 to -20 K) than the observed (R^2 = 0.16). The 37V simulations show little difference from observations with regard to ice crusts; however, the 37H simulations show an underestimation and inverse relationship to ice crust observations. This occurs only when the ice crusts are lower than the 130 mm saturation level.

Finally, there are similar levels of SWE contribution from both the windslab and recent snow, when compared to that of the depth hoar. However, the change in the observed 37 GHz values for these SWE contributions is mirrored, not matched, by the simulations. The inverse relationship between observations and simulations occurs because the windslab (R^2 = 0.17V, 0.19H) and recent snow (R^2 = 0.46V, 0.0003H) layers occurred above 130 mm SWE level, and the simulations continue to show increased scattering with additional SWE. The simulations do

not capture observed scattering extinction in any case (note that no hollow 'HUT' symbols are present above 0 for both the V and H 37 GHz contribution, Figure 4.5 Top). This reinforces the previous results which indicate relative agreement for simulations and observations below 130 mm SWE, and a marked divergence above that level, as the simulations fail to capture observed scattering extinction, and emission from the snow pack itself. Thus, scattering contributions from the upper layers of the snowpack are not evident in the observations; however, the simulations continue to show only increased scattering with these SWE contributions.

4.5 Discussion

4.5.1 The sensitivity of HUT to SWE

The results in this work indicate that for all snow cover types, as the SWE increases above ~130 mm, the multi-layer HUT model produces TB values that continue to decrease, and so are biased lower than observations, as simulations show continued scatter with additional SWE. The empirically derived extinction coefficient in the HUT model fails to capture the 37 GHz saturation and insensitivity to additional SWE. The use of the layered-excavation sampling technique showed that the model reasonably simulates scattering due to large-grained depth hoar. This agrees with previous work that have shown improvements in accuracy with a 2 layer model which considers depth hoar and another smaller grained layer (Lemmetyinen et al. 2015). The greatest change in TB occurs because of scattering generated by depth hoar at the bottom of the snowpack. Large SWE contributions from other snow types (wind slab, recent snow) do not result in similar changes in observed TB. This masking of SWE contribution for various snow types, by scattering from depth hoar that is disproportionate to its SWE contribution, complicates the linear relationship of 19V – 37V TB for direct inversion of SWE, which can leave up to 50%

of SWE unaccounted for. A potential moderating effect on scattering during the seasonal transition of the snowpack from a scattering to an emitting medium, could be due to the depth hoar acting as a coherent scattering layer as grain size and shape changes due to densification and kinetic processes (Rosenfield and Grody 2000). However, as Rosenfield and Grody (2000) note, this results in coherent scattering which the HUT model does not consider, but which may be an additional source of error. The addition of a depth hoar layer as input to the HUT radiative transfer model could more accurately account for the scattering of the 37V signal occurring due to depth hoar microstructure, which is generally underrepresented in single-layer HUT simulations.

4.5.2 Grain size

Single layer implementations of the HUT model underrepresent larger grains and over represent smaller grains, as grain size is homogenized through averaging (Kontu and Pulliainen 2010; Rutter et al. 2014). However, as simulated scattering is not linear with grain size, frequency dependent scattering by many grains of the same size is not the same as that from both larger and smaller grains, as demonstrated by Rutter et al. (2014). This is evident in the grain sizes required to match the simulations to TB for the various snow layers and types. The grain size required by the extinction coefficient developed by Roy et al. (2004) would likely agree well with the observed grain size for depth hoar (below 130 mm SWE), had simulated and observed initial ground state been identical, as explored in Lemmetyinen et al. (2015). The required grain size for both tested extinction coefficients agree for smaller-grained snow layers in the upper snow pack (e.g. Wind slab, recent snow).

4.5.3 Implications for GlobSnow assimilation

The GlobSnow assimilation method (Pulliainen 2006) weights a single-layer HUT radiative transfer model estimation of SWE, optimized using satellite TB measurements and available in-situ SD/SWE measurements, by their respective statistical uncertainties (Takala et al. 2011). The assimilation begins with an optimization to find an effective grain size. The single-layer HUT model is used with snow depth observations from weather stations and a fixed density, to fit modeled to observed TB by varying grain size. The optimization of a single effective grain size integrates error from physical inputs (including vertical heterogeneity) and the TB fitting processes, and is therefore not necessarily related to physical grain size. The initial accuracy of effective grain size, in the first stage of the assimilation, is essential to optimization and assimilation performance (Pulliainen 2006), as subsequently this grain size and its variance are then fixed to determine SWE. The unaccounted scattering from the depth hoar contributes error to the initial effective grain size calculations, which in turn affects the weighting of the model components through less accurate variance, creating increased overall error and bias. The inclusion of a depth hoar layer in the assimilation could better account for scattering contributions resulting in a more accurate initial effective grain size. Additionally, the continued scattering exhibited by HUT simulations at 37 GHz to SWE above the observed signal saturation level may further complicate the grain optimization.

4.6 Conclusions

Accurate a priori information on snow characteristics, particularly microstructure, is necessary to accurately retrieve SWE over large scales (Takala et al. 2011; Lemmetyinen et al. 2015). Relating physical grain size observations to effective grain size would improve SWE inversion

with regard to regionally and temporally heterogeneous snow microstructure (Lemmetyinen et al. 2015). Additional error in SWE retrieval occurs as the snow transitions from a scattering to an emitting medium at a given frequency. We present results of plot-scale multi-layer observed and simulated TB at 19 and 37 GHz using a novel excavation process to examine the layered contributions to microwave emission and scattering for several types of snow in the Canadian sub-Arctic. We find the large-grained depth hoar is generally well modeled, and model performance below 130 mm saturation threshold is consistent with other work. We also show that the depth hoar layers contribute large changes to TB with relatively less SWE when compared to other smaller grained snow types. Above saturation, the observations and simulations diverge as the model remains sensitive to additional scattering that does not naturally occur. This is a source of error that will impact the initial effective grain size optimization process in the GlobSnow SWE assimilation process. This inaccuracy is carried forward in the assimilation process through variance calculations which weight the contributions of assimilation modules, both spatially and temporally, leading to less accurate SWE retrievals.

Based on the results of our work, priority issues for the use of the HUT model within satellite retrieval schemes such as GlobSnow include:

1) The addition of a depth hoar layer to more accurately account for the scattering of the 37V signal occurring due to large grains, which are generally underrepresented in single-layer HUT simulations. The GlobSnow assimilation method begins with an optimization to determine an effective grain size, so the inclusion of a depth hoar layer in the assimilation could better account for scattering contributions resulting in a more accurate initial effective grain size and more accurate characterization of the 37 GHz signal saturation. We acknowledge, however, the

challenges in implementing multi-layer snow inputs to operational SWE retrieval algorithms when only snow depth information is systematically available in near real time from weather stations. Future work should consider how to separate fine grained surface layers (such as recent snow and wind slab) from depth hoar for a two layer implementation of a GlobSnow-type retrieval.

2) The continued sensitivity of the multiple-layer HUT model to SWE above the approximate saturation threshold (~130 mm) must also be considered, as this could decrease the accuracy of snow depth and SWE inversion or assimilation techniques.

These are important considerations as studies have shown increased RMSE for Canadian Arctic SWE retrievals, attributed to snowpack layering, increased spatial heterogeneity, and fewer observational inputs (Lemmetyinen et al. 2010; Takala et al. 2011; Derksen et al. 2014).

Chapter Five: **Comparison of a coupled snow thermodynamic and radiative transfer model with in-situ active microwave signatures of snow covered smooth first-year sea ice.**

5.1 Abstract

Within the context of developing data inversion and assimilation techniques for C-band backscatter over sea ice, snow physical models may be used to drive backscatter models for comparison and optimization with satellite observations. Such modeling has potential to enhance understanding of snow on sea ice properties required for unambiguous interpretation of active microwave imagery. An end-to-end modeling suite is introduced, incorporating regional reanalysis data (NARR), a snow model (SNTHERM), and a multi-layer snow and ice active microwave backscatter model (MSIB). This modeling suite is assessed against measured geophysical properties of snow on sea ice, and observed active microwave backscatter. NARR data was input to the SNTHERM snow thermodynamic model, in order to drive the MISB model for comparison to detailed geophysical measurements and surface-based observations of C-band backscatter of snow on first-year sea ice. The NARR data was well correlated to available in-situ measurements, with the exception of long wave incoming radiation and relative humidity, which impacted SNTHERM simulations of snow temperature. SNTHERM reasonably represented snow grain size and density when compared to observations. The application of in-situ salinity profiles to one SNTHERM snow profile resulted in simulated backscatter close to that driven by in-situ snow properties. In other test cases, the simulated backscatter remained 4 to 6 dB below observed for higher incidence angles, and when compared to an average simulated backscatter of in-situ end-member snow covers. Development of C-band inversion and assimilation schemes

employing SNTHERM89.rev4 should consider sensitivity of the model to bias in incoming longwave radiation, the effects of brine, and the inability of SNTHERM89.Rev4 to simulate water accumulation and refreezing at the bottom and mid-layers of the snowpack with regard to thermodynamic response, brine wicking and volume processes, snow dielectrics, and microwave backscatter from snow on first-year sea-ice.

5.2 Introduction

Snow cover plays an important role in radiative transfer interactions due to its thermal capacity, conductivity, diffusivity, and albedo (Robok 1983). Snow cover governs the heat and energy exchange across the ocean-sea ice-atmosphere interface, and therefore, controls sea ice formation, ablation, extent and thickness processes (Maykut 1982; Curry et al 1995). This is important to the global climate system due to the significant amount of energy involved in sensible and latent heat exchanges (Serreze and Barry 2005). Snow albedo is controlled by grain size, which is both affected by, and effects, energy exchange. The distribution and character of snow cover is highly variable both spatially and temporally, and will undergo distinctly different melt and freeze cycles when forced by the same atmospheric event, based on the arrangement of snow mass (snow water equivalent, SWE). This difference in thermal response affects the basal snow layer brine volume and snow grain development, which may be used to discriminate snow thickness and water equivalent through use of remotely sensed microwave backscatter (Barber and Nghiem 1999; Yackel and Barber 2007; Langlois, Barber et al. 2007). Snow cover on sea ice is typically represented in physical and backscatter models as a two or three layer system of fine grained fresh snow or dense windslab, overlying more coarsely grained depth hoar of lower density, and brine covered basal snow (e.g. Crocker 1992; Barber et al. 1995; Geldsetzer et al.

2007). However, increases in the alternation of early spring rain, snow, and melt events (Trenberth et al. 2007) can result in a more complex layering of snow. This increase in the number of ice lenses, drainage channels, and inclusions, affects the thermodynamic response of various configurations of snow cover to subsequent forcing. This in turn affect snow grain development, drainage, brine distribution, and seasonal melt processes (Colbeck 1991) pertinent to C-band microwave backscatter over first-year sea ice (Fuller et al. 2014). Improvements in geophysical inversion from microwave imagery may in turn be used to improve snow modeling (Pulliainen 2006; Durand 2007; Geldsetzer et al. 2007).

Changes to the composition of sea ice in the Arctic system affect the accuracy of geophysical and thermodynamic properties, which are required for management strategies (Barber 2005; Warner et al. 2013). An expected increase in the rate of both early and late season precipitation and melt events in the Arctic will add complexity to both snow thermodynamic modeling, and to interpretation of microwave remote sensing data, as multiple snow and ice conditions can lead to similar backscatter results (Barber et al. 2009; Warner et al. 2013; Fuller et al. 2014; Gill and Yackel 2012; Gill et al. 2014). In such cases, a snow thermodynamic model may be used to for comparison and inversion of important snow properties (e.g. SWE, grain size) for a given backscatter response. Satellite-based remote sensing provides a larger scale of observation; however, error stems from relating backscatter values to snow and ice structure and dielectrics (Durand 2007). Potential solutions to these issues are being developed in state-of-the-art data assimilation techniques, which update snow physical and radiative models with available in-situ snow and meteorological observations (Sun et al. 2004; Andreadis and Lettenmaier 2006; Pulliainen 2006; Durand 2007). These are focused toward providing estimates for large areas

with few in-situ observations, such as the Canadian Arctic (Matcalfe and Goodison 1993; Langlois et al. 2009). Accurate representations of snow density, albedo, and storage and refreezing of liquid water in the snowpack, as inputs to snow models, are required for consistent results (Essery et al. 2013). Inversion or assimilation schemes that focus on C-band backscatter in the Canadian Arctic may encounter error, as in-situ conditions may not be as they appear in ice charts and satellite imagery (e.g. Barber et al. 2009; Warner et al. 2013).

The Canadian Ice Service (CIS) integrates, analyses, and interprets many data sources to produce weekly regional charts estimating properties such as ice type, thickness, and concentration (www.ec.gc.ca); however, these may contain inaccuracies (e.g. Barber et al. 2009; Warner et al. 2013). The simulation of snow physical properties pertinent to backscatter can lend insight to the actual cause of the microwave response, and is necessary given the vast scale of the Canadian Arctic, which has relatively few in-situ climate or snow-physical observations. This work represents the first assessment of the suitability of reanalysis data, a one-dimensional snow evolution model, and active microwave backscatter model in development of an operational end-to-end weather-snow-backscatter estimation technique. Within the scope of this study, the models used are North American Regional Reanalysis (NARR), the snow thermodynamic model (SNTHERM) of Jordan (1991), and a multi-layer snow and ice backscatter model (MSIB); each of these are described in detail below. These model analyses are necessary in part to evaluate the error in ice charts and satellite observations, particularly when considering the effects of more complexly-layered snow (e.g. Fuller et al. 2014). Previous work has considered the simulation of passive microwave emission from physical snow models over land (e.g. Wiesmann et al. 2000) and the use of NARR variables to drive SNTHERM (and other snow physical models) for

passive Microwave Emission Modeling of Layered (MEMLS) simulation over land (e.g. Langlois et al. 2009), for soil temperature estimation (e.g. Kohn and Royer 2010), and for downelling atmospheric emission estimation over land (e.g. Monpetit et al. 2013). Willmes et al. (2014) employed European Re-Analysis data to drive SNTHERM and subsequently MEMLS for simulation of passive microwave emission of snow and sea ice. To the authors' knowledge, this study represents the first assessment of an end-to-end modeling suite to estimate active microwave backscatter over sea ice. The use of NARR data to drive a snow thermodynamic model, which in turn drives an active microwave backscatter model at C-band provides a novel methodology to resolve snow and ice properties that produce ambiguity in active microwave image interpretation.

SNTHERM is a one-dimensional, multilayer thermodynamic model originally developed for snow temperature simulations (Jordan, 1991), and which was later adapted for sea ice (Jordan and Andreas 1999). SNTHERM uses hourly meteorological variables to simulate thermodynamic processes of air, soil, and liquid, solid, and vapour states of water. The simulated outputs include snow cover properties such as temperature, SWE, grain size, liquid water content, layer thickness, and depth, which are pertinent to microwave remote sensing. The model predicts grain growth from thermal and vapor gradients and albedo, and accounts for water percolation, which is artificially drained from the bottom of the snowpack-surface interface. It requires an initial state of snow and ice character including, the number of layers (nodes), grain size, density, temperature, mineral density, heat capacity, and thermal conductivity. Heat fluxes are transferred from snow to ice, which in turn updates snow temperatures at each time step. Operational concerns, and sparsely detailed in-situ meteorological data for large areas of the

Canadian Arctic, can require the use of reanalysis data. North American Regional Reanalysis (NARR) data is high-resolution (32 km grid) and computed in near-real time in 3 hour time steps (Mesinger et al. 2006). It provides detailed temperature, wind speed, relative humidity, radiation, and precipitation data, necessary to SNTHERM. NARR has shown good correlation with ground-based meteorological measurements and plot-scale in-situ observations for snow and soil thermodynamic and passive microwave radiometric modeling (e.g. Langlois et al. 2009; Kohn and Royer 2010).

The multilayer snow and ice backscatter (MSIB) model simulates the co-polarized backscattering coefficient (dB) for vertical and horizontal polarizations ($\sigma 0VV$, $\sigma 0HH$). The model expands upon methods developed by Kim et al. (1984) and Ulaby et al. (1984). It simulates both surface (Kirchoff physical optics method for smooth surfaces per Rees (2006)) and volume scattering (based on grain number-density and grain size, per Drinkwater (1989)), and employs a two-way loss factor for incoming and outgoing scattering power (Winebrenner et al. 1992; Kendra et al. 1998). The model accounts for transmission, scattering, absorption, and refraction contributions from each layer volume, and at layer interfaces. The model is described in Scharien et al. (2010) and Fuller et al. (2014). Key inputs for the MSIB model are temperature, density, layer thickness, salinity, and snow grain size.

5.2.1 Objectives

The overall focus of this work lies in the operational application of SNTHERM derived snow properties to MSIB simulated backscatter. As such, NARR meteorological data are used to drive the SNTHERM snow model for comparison with case-studies of observed snow properties, and with plot-scale modeled and observed backscatter for layered snow on first-year sea ice. The

overarching research question we address is: Can NARR-driven SNTHERM simulated snowpack layers, used in the MSIB backscatter model, reproduce observed backscatter for snow-covered first-year sea ice?

The specific questions addressed are:

1) How does NARR compare to in-situ meteorological data with regard to variables pertinent to SNTHERM89.rev4?

2) How does SNTHERM89.rev4 output compare to in-situ snow structure and geophysical properties pertinent to C-band microwave backscatter over first-year sea ice?

3) How do simulated backscatter signatures based on SNTHERM89.rev4 output compare to simulations from observed snow structure and properties, and observed backscatter for complexly-layered snow over first year sea ice?

4) What are the implications for the use of the SNTHERM89.rev4 thermodynamic model in an operational scenario for simulation of C-band backscatter over first-year sea ice?

5.3 Methods

5.3.1 Study area

The study area is located near Churchill, Manitoba and took place in 2009 from April 7th through May 15th, on landfast first-year sea ice in Bird Cove (N 58.812, W 093.895) Hudson Bay. This site is fully described in Fuller et al. (2014). Samples were acquired on a smooth 4 km by 1.5 km pan of first-year sea ice, and included detailed snow geophysical and surface-based C-band backscatter measurements.

5.3.2 Data collection

5.3.2.1 Meteorological data

Meteorological data was acquired by in-situ instruments (relative humidity (RH)), from Environment Canada's 'Churchill A' station (temperature), and from NOAA NCEP NARR data (temperature, RH, wind speed, long and shortwave incoming and outgoing radiation and precipitation amount). The in-situ meteorological instruments were located 500 m adjacent to the snow sample sites, the Churchill A station (N58.733, W 094.050) is approximately 20 km from the study site, and the NARR data was downloaded for the 32 km grid containing the sample site. This grid contains a roughly even split of land and bay. In-situ RH data was sampled every 10 minutes and then averaged to hourly, and NARR data was resampled from 3 hour to hourly data using a linear interpolation.

5.3.2.2 Snow geophysical data

Snow geophysical data were collected directly adjacent to the surface-based scatterometer. Measurements of temperature, density, snow microstructure, dielectrics, and salinity were acquired every 2 cm in vertical profile. Snow grain major and minor axis and morphology was determined visually from samples placed and photographed on a standard grid card. The geophysical data acquired are fully described in Fuller et al. (2014).

5.3.2.3 Scatterometer data

The surface-based C-band backscatter measurements (σ^0_{VV}, σ^0_{HH}) were acquired continuously throughout the day (May 15th, 2009) for a 20° to 70° elevation range (in 2° increments) and an 80° azimuthal range. The scatterometer was fixed in location and was mounted at a height of 2.2 m. The system specifications are in Table 5.1. The validation of the system is described in

Geldsetzer et al. (2007) and measurement techniques pertinent to this study are described further in Fuller et al. (2014).

Table 5.1. C-band scatterometer specifications.

RF output frequency	5.5 GHz ± 2.50MHz
Antenna type	0.61-m parabolic reflector, dual linear polarization
Antenna beamwidth	5.4°
Cross polarization isolation	>30 dB, measured at the peak of the beam
Transmit power	12 dBm
Bandwidth	5–500 MHz, user adjustable
Range resolution	0.30m
Polarization mode	Polarimetric (HH, VV, HV, VH)
Noise floor	Co ~ -36 dBm, cross ~ -42 dBm
External calibration	Trihedral corner reflector

5.3.3 SNTHERM and NARR

The latest publicly available SNTHERM89.rev4 was used in this work, and as such, does not treat sea ice specifically; however, sea ice parameters can be entered as layers in the model to account for the thermal capacity and conductivity. SNTHERM uses hourly meteorological variables including temperature (K), relative humidity (%), wind speed (m s^{-1}), incoming and outgoing shortwave radiation and incoming longwave radiation (W m^{-2}), precipitation amount (SWE, mm), and effective precipitation particle size (m). For each precipitation event, SNTHERM adds a new layer to the top of the snowpack; the layer is combined with the one below if and when the layer thickness reaches a prescribed minimum (Jordan 1991; Durand 2007). SNTHERM bases grain growth for dry snow on current grain size and vapor flux through the snowpack, with a set maximum flux and kinetic growth limit of 5 mm grain diameter. The model assumes no vapor flux between the bottom layer and that directly above it (Jordan 1991; Jordan and Andreas 1999), resulting in slowing grain growth for the layer above (Durand 2007).

Pertinent to MSIB, SNTHERM output provides layer thickness (m), density (kg m^{-3}), temperature (K), and grain size diameter (m) (Jordan 1991; Langlois et al. 2009). NARR meteorological data was used to drive SNTHERM in all cases. The outgoing shortwave radiation was recalculated to 85% of the incoming shortwave radiation as per Curry et al. (1995) (explored in Section 5.4.1). SNTHERM was run under two different geophysical initial conditions to test sensitivity to initial condition inputs, as the model run was for 38 continuous days from April 7th to May 15th (Table 5.2):

SNTHERM A) 2 cm fresh ice superimposed over first-year sea ice, representative of bare ice conditions observed on April 7th, before a snow event.

SNTHERM B) 10 cm of snow over a 2 cm fresh ice layer, superimposed over first-year sea ice, representative of in-situ observations taken April 8th, after a snow event.

Hourly meteorological state variables include 2 m air temperature, 2 m relative humidity, 10 m wind speed, incoming and outgoing shortwave radiation and incoming longwave radiation, precipitation amount. Initial condition input variables include the number of layers, layer thickness, associated density, associated grain size, average barometric pressure (1018 mb, averaged from Churchill A measurements concomitant to the 38 day SNTHERM run), snow albedo (0.85), and new snow density (100 kg m^{-3}). The sea ice initial state variables are proportion of brine (6 %), bulk density (915 kg m^{-3}) (Carsey 1992) heat capacity (2100 J kgK^{-1}), and emissivity (0.86) (Wadhams 2000), and thermal conductivity (1.96 W mK^{-1}) (Schwerdtfeger 1963).

Table 5.2. Initial conditions for Cases A and B. Note small artificial grain sizes input for sea ice. These values were also tested at 0.001 m and did not affect the results of the simulations.

Layer	Thickness (m)	Density kg m^-3	Grain Diameter (m)
SNTHERM Initial Condition (A)			
Fresh Ice	0.02	915	0.001
Sea Ice	1.52	915	0.0001
SNTHERM Initial Condition (B)			
Snow	0.02	202.8	0.001
Snow	0.02	221.5	0.001
Snow	0.02	221	0.001
Snow	0.02	210	0.001
Snow	0.02	248.7	0.001
Fresh Ice	0.02	915	0.001
Sea Ice	1.52	915	0.0001

5.3.4 Multilayer Snow and Ice Backscatter (MSIB) model

The MSIB model was run using the SNTHERM A1, A2 and B1, B2 results (see cases descriptions at the end of this paragraph) and from 3 samples of detailed in-situ geophysical parameters (Sample 1, Sample 2, Sample 3). The layered outputs from SNTHERM were amalgamated via weighted averaging into approximately 2 cm layers, to match the vertical resolution of the in-situ geophysical measurements. SNTHERM89.rev4 does not account for brine wicking in the snow and associated salinity values. This is an important consideration, as brine-wetted snow affects C-band backscatter through both increased loss and volume scattering (Barber et al. 1994; Geldsetzer et al. 2007). As such, (1) typical salinity values (Barber et al. 1995) and (2) in-situ observed salinity values (Figure 5.9) were applied to SNTHERM derived snow profiles for input to the MSIB:

1) Cases A1 and B1 were assigned typical salinity values for first year sea ice and overlying snow (Barber et al. 1995).

2) Cases A2 and B2 and were assigned average salinity values observed in-situ (Fuller et al. 2014).

5.4 Results and Discussion

5.4.1 NARR and in-situ meteorological comparison

A comparison of reanalysis data to in-situ measurements pertinent to SNTHERM inputs are presented in Figure 5.1 through Figure 5.7. The NARR data correlates reasonably well for 2 m air temperature (R^2 0.74, Figure 5.1) and 10 m wind speed (R^2 0.72, Figure 5.2). The reanalysis data overestimates air temperatures below the melting point and slightly underestimates air temperatures near the melting point. Temperature impacts the accuracy of simulations with regard to temperature gradients through the snowpack and associated vapor fluxes. This has implications for the simulated melt and freeze cycles, potentially affecting grain growth. NARR underestimates the moderate to high wind speed, which impacts simulated aeolian snow transport mechanisms, effective precipitation particle size, density through the snowpack, and convective processes. For these reasons, effective particle size of new precipitation (input to SNTHERM) was fixed at 1 mm, per in-situ measurements of very recent snow grains that created the initial conditions used in SNTHERM B simulations. The performance of NARR is poor for relative humidity (Figure 5.3), which may compound the effects of temperature inaccuracies. The relative humidity impacts energy and mass transfer in SNTHERM through melt, sublimation, and evaporation, and vapor flux is a driver of grain growth in the model.

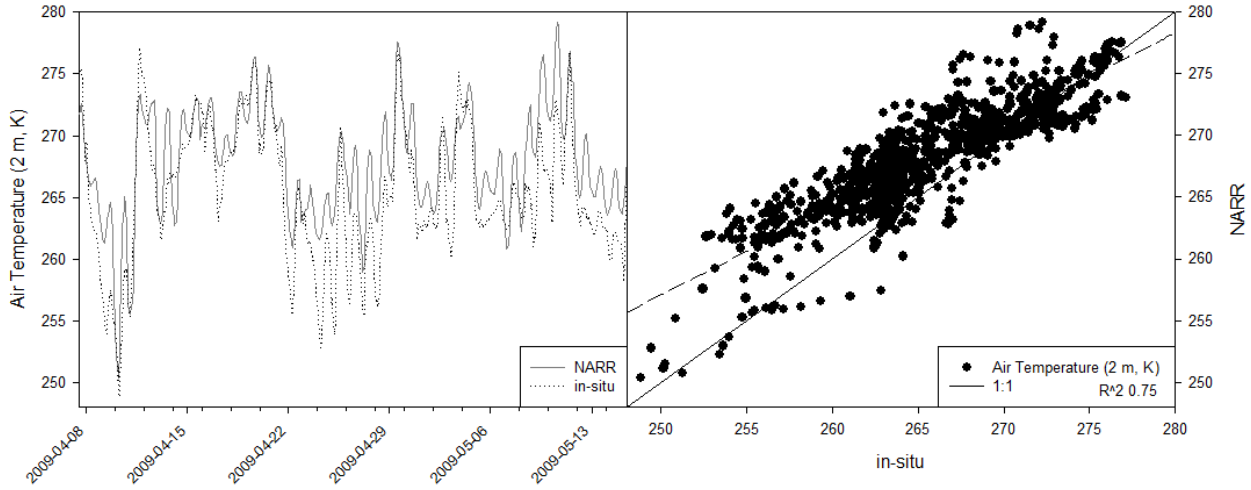

Figure 5.1. Air temperature (2 m, K) for the observation period, and the relationship between NARR and in-situ values.

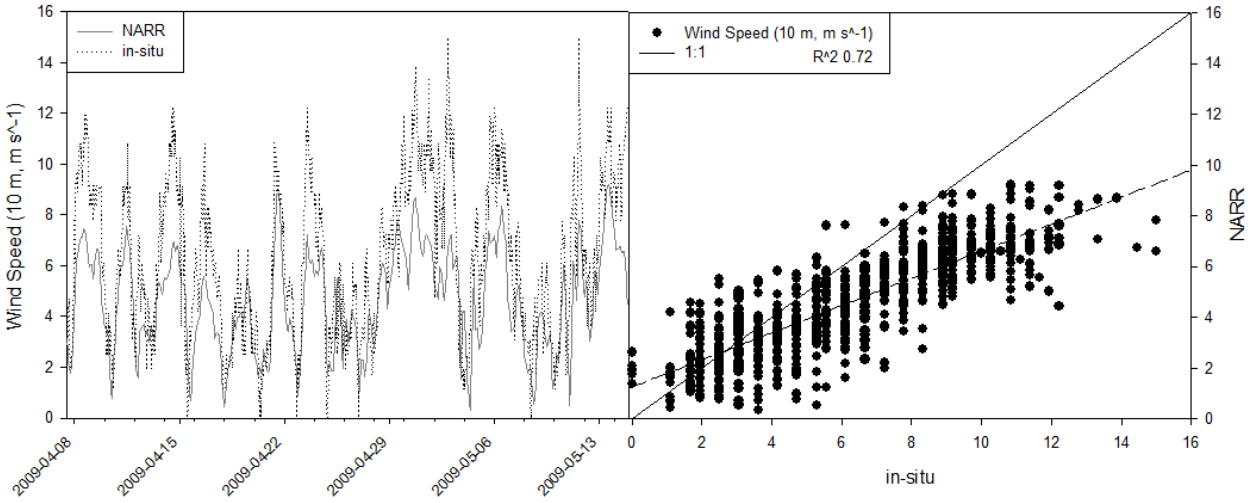

Figure 5.2. Wind speed (10m, m s^{-1}) for the observation period, and the relationship between NARR and in-situ values.

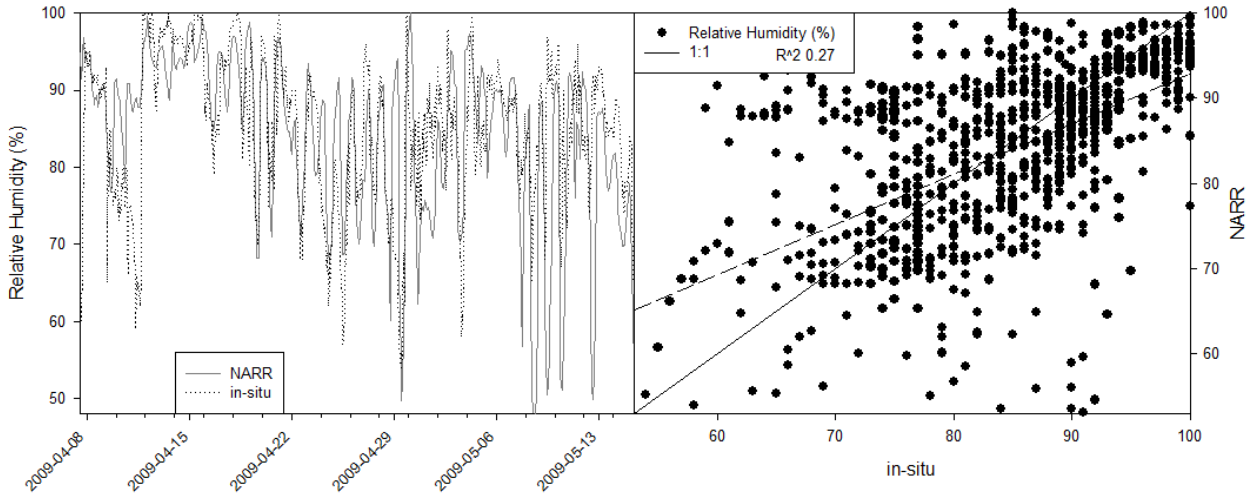

Figure 5.3. Relative humidity (%) for the observation period, and the relationship between NARR and in-situ values.

No in-situ radiation data were acquired for the sea ice sample location in 2009. As a proxy comparison for the effects of the mixed NARR grid on solar radiation reanalysis, short-wave radiation data acquired hourly from January 13th to March 23rd, 2010 is used (Figure 5.4). The 2010 site was situated at an ice covered lake within 12.25 km (N 58.719, W 093.794) of the 2009 sample location, and is located in the same NARR grid cell as the 2009 study site. While this situation is not ideal, it provides a basis for comparison, as it lends insight and corroboration into the lower correlations of the in-situ meteorological variables that we were able to more directly compare. The 2010 data is denoted with an asterisk in Figure 5.4 through Figure 5.6.

A comparison of 2010 in-situ and NARR data exhibit relatively good correlations for solar radiation (R^2 = 0.89 incoming, R^2 = 0.87 outgoing). The 2010 NARR shortwave incoming and outgoing values resulted in an albedo of approximately 0.65, which is lower than the in-situ measurements (0.81) (Figure 5.5). Initial model runs using the 2009 NARR solar radiation values entirely melted the SNTHERM-generated snowpack. As such, an albedo of 0.85 was chosen,

based on the results of the 2010 data comparison, and on values from literature (Curry et al. 1995; Marshall 2011; Perovich and Polashenski 2012).

The low correlation (R^2 0.35; Std. Err. Est. 32.5) for the incoming longwave NARR radiation value (Figure 5.6) impacts SNTHERM simulation accuracy of snowpack temperature (Lapo et al. 2015), as upward longwave flux moves heat from snow and ice to atmosphere, and is dependent upon air temperature and water vapor pressure (Maykut 1986). This may partially explain the low correlation of relative humidity, but is not related to the NARR predicted 2 m air temperature, 10 m wind speed, or precipitation, as these are assimilated from surface observations (Mesinger et al. 2006).

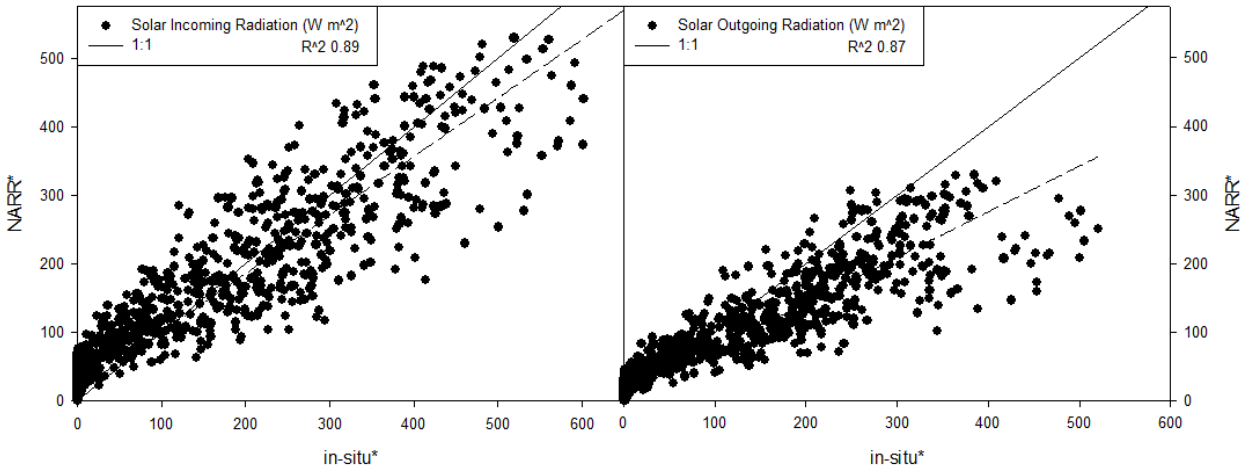

Figure 5.4. Incoming and outgoing shortwave radiation for the 2010 site for proxy comparison.

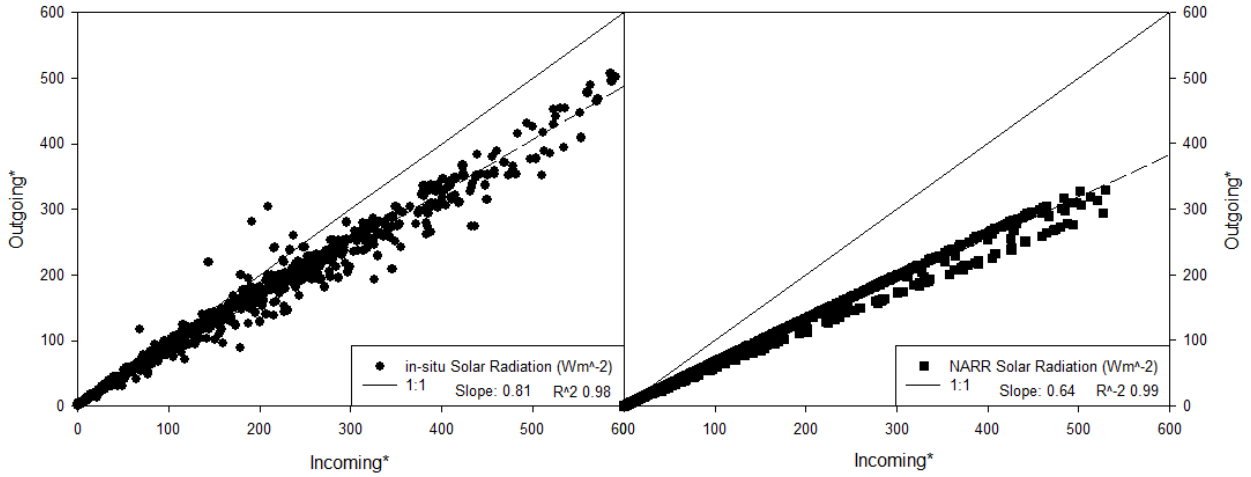

Figure 5.5. 2010 in-situ (Left) and NARR (Right) incoming and outgoing shortwave radiation. 2010 NARR data resulted in an unrepresentative albedo (slope) of 0.64 compared with 2010 in-situ measurements (0.81).

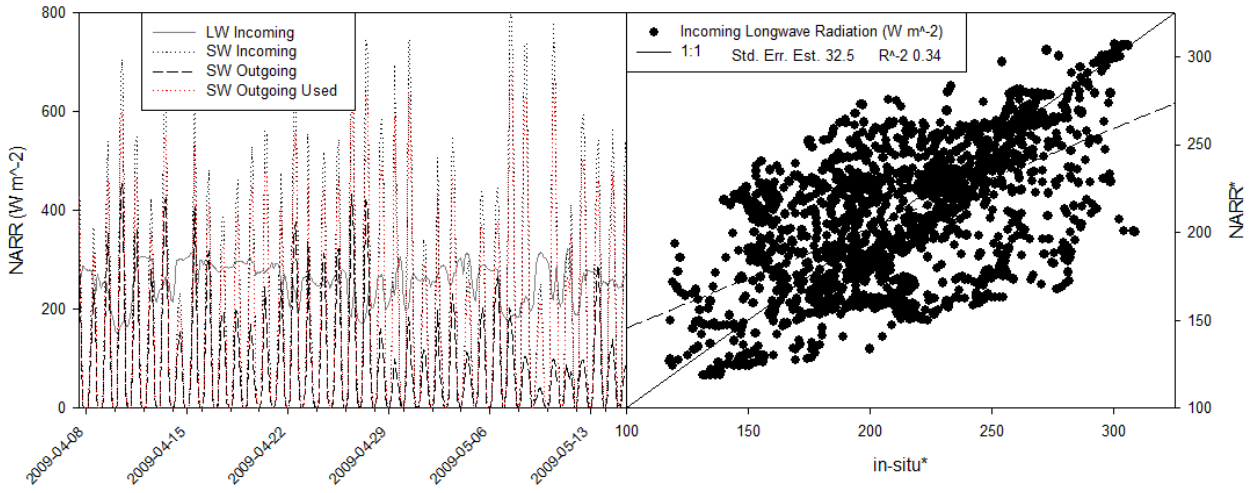

Figure 5.6. Left: NARR long and shortwave radiation for the 2009 study period. Right: incoming longwave radiation for the 2010 proxy comparison period.

In-situ precipitation data were acquired from unshielded Nipher snow gauge (2 m Height) measurements for the period April 30th to May 15th, 2009. The samples were acquired every three to five days and were extrapolated to equal daily values. These results show reasonable agreement for the May 10th to 15th precipitation event; however, the performance is poor for the

previous time periods. The total SWE accumulated by NARR for the observation period is 54 mm, with the 40 mm accumulation between April 30th and May 15th and compared with 35 mm observed SWE for the same time period. However, field notes indicate that water from the measurement was lost on May 3rd and May 10th, partially accounting for the discrepancy. The NARR grid sampled for this work exists in a transition zone covering approximately half sea ice and half land, which likely complicates the reanalysis and may partially account for the low correlation values, when compared with in-situ data. The precipitation amounts derived from NARR were initially input to SNTHERM at 0.1 mm resolution. These very low precipitation amounts resulted in the precipitation evaporating before it could accumulate and the model reaching the nodal (layer) limit, ending the model runs prematurely. Subsequently, NARR precipitation amount was aggregated to daily values and input to 0900h for each day. On days in which Environment Canada Churchill A station and in-situ field observations noted rain and snow in the same day (April 14th, 15th, and May 11th), the daily precipitation amount was aggregated to each precipitation type based on number of hours. This impacts liquid water inputs and drainage through the snowpack, and therefore latent and sensible heat transfers in SNTHERM simulations.

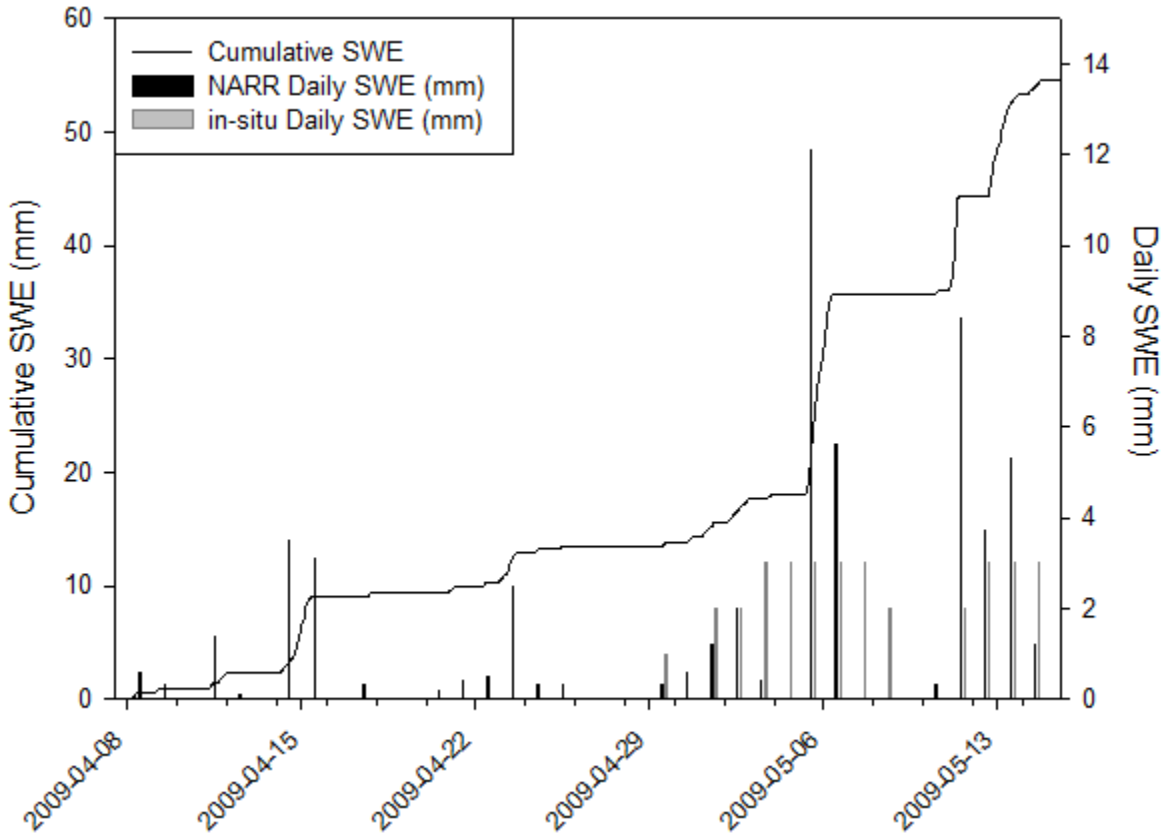

Figure 5.7. NARR precipitation events and SWE accumulation for the entire study period, with a comparison of in-situ Nipher gauge observations for the period April 30th to May 15th, 2009.

3.2 SNTHERM and in-situ snow properties comparison

The SNTHERM outputs are compared to in-situ snow geophysical observations, pertinent to C-band backscatter (Figure 5.8 through Figure 5.10). Three snow pits were sampled in-situ and represent the various snow thicknesses in the area directly adjacent to the scatterometer measurements. The snow density values show good agreement with in-situ measurements, with the exception of the uppermost layers of the snowpack (Figure 5.8). The density values for the lower snowpack are sensitive to initial condition (Willmes et al. 2014), as there is closer agreement between initial condition B and in-situ observations. Note that the mid pack ice-layer

found in Samples 2 and 3, are not replicated by SNTHERM. This non-replication of ice layers by SNTHERM, which was also noted by Langlois et al. (2009), substantially affects the snowpack stratigraphy and thereby impacts thermodynamic processes controlling grain morphology, melt-water drainage, brine wicking and volume, and other melt and refreeze processes (Colbeck 1991) of relevance to microwave scattering. The SNTHERM simulations overestimate temperature by up to 6°C in the upper snowpack, and by 2°C in the lower 8 cm of the snowpack (Figure 5.8), resulting in melt layers within the simulated snowpacks. This is to be expected as NARR longwave radiation was found to be poorly modeled with a standard error of 32.5 W m^{-2}, causing greater than expected longwave input to SNTHERM. This warmer than expected temperature profile increases dielectric permittivity (e′) and loss values (e″) (Figure 5.10) through increased liquid water content. (Figure 5.9). The 2°C difference found in the bottom 8 cm of the snowpack is important as it impacts brine volume, and allows for melting at temperatures below zero in the MSIB model. This is compared to the relatively drier and cooler snow conditions in MSIB simulations driven by observed snow parameters for Samples 1 through 3. The temperature difference is important as dielectric permittivity and loss, as a function of brine volume in the basal-snow and near-surface sea-ice, is the primary factor affecting C-band microwave backscatter signatures (Barber et al. 1994; Nghiem et al. 1995b; Geldsetzer et al. 2009).

The case A and B SNTHERM initial conditions predicted snow depths of 20 cm (A) and 27 cm (B), which compares reasonably well to the three in-situ observations of 24, 26 and 32 cm (respectively, Sample 1, Sample 2, Sample 3). The in-situ measured SWE was 58 mm, 96 mm, and 143 mm, for samples 1 through 3, respectively. This compares to 43 mm and 67 mm (the latter including 22 mm initial condition SWE) for SNTHERM A and B, respectively. There were

several rain on snow events during the observation period. These contributed SWE to the observed snowpack; however, SNTHERM artificially removes gravimetrically drained water from the bottom of the snowpack, removing up to 12 mm of SWE, when compared to NARR estimated precipitation inputs. However, melt events can be traced through the snowpack via SNTHERM outputs of snow layer conditions and temperatures. SNTHERM does take into account wind speed with regard to snow transport, density, and packing of windslab. The discrepancy between NARR and in-situ measured wind speeds may explain part of the SWE accumulation difference. Since SNTHERM is a 1-D model, advected snow supply from surrounding areas is not considered, but could be a source of error, given observed wind speed was consistently between 4 and 11 m s^{-1}, with periods of up to 15 m s^{-1} during this time period (Figure 5.2). This may compound SWE inaccuracies when added to the artificial removal of liquid water. The higher SWE values and greater densities in the in-situ observations will result in differences in thermal capacity and conductivity for a given layer, when compared to SNTHERM simulations. This, in addition to the poor longwave input and a lack of accounting for the thermodynamic effects of brine volume throughout the SNTHERM run, contribute to the snow temperature differences (Figure 5.9). Grain size agrees relatively well with observations (Figure 5.8), reinforcing the choices to assign a more representative albedo to the NARR data, and to fix precipitation effective particle size at 1 mm, as grain size controls albedo and is also of primary concern to microwave backscatter.

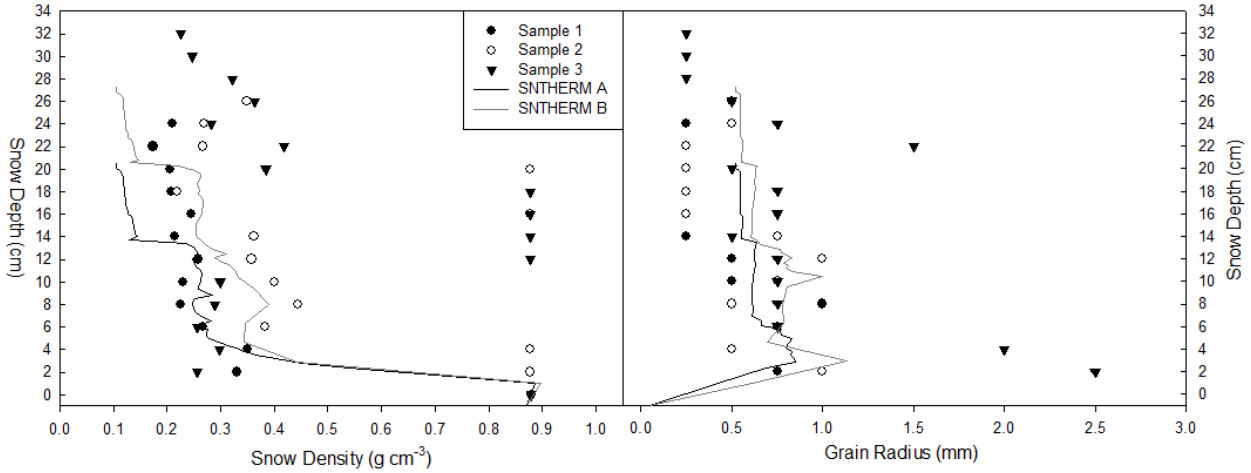

Figure 5.8. In-situ measured and SNTHERM simulated density and grain radius values. Note the high density ice layer observed in Samples 2 and 3, between 12 and 22 cm snow depth.

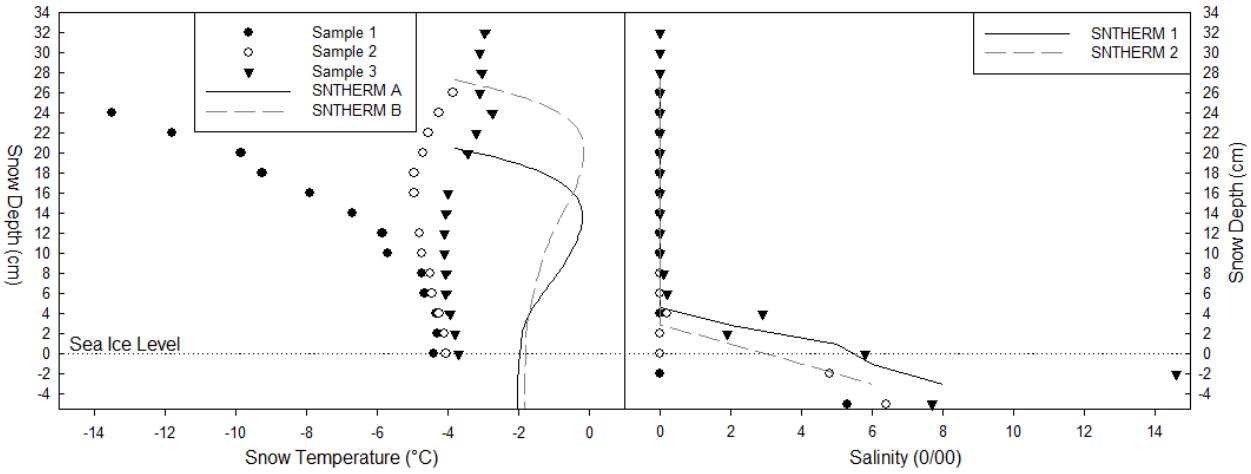

Figure 5.9. In-situ Sampled (1, 2, 3) and SNTHERM simulated snow temperature values. In-situ Sampled (1, 2, 3) salinity values, with the typical (SNTHERM 1) and low (SNTHERM 2) salinity values applied to the snow profiles input to the MSIB.

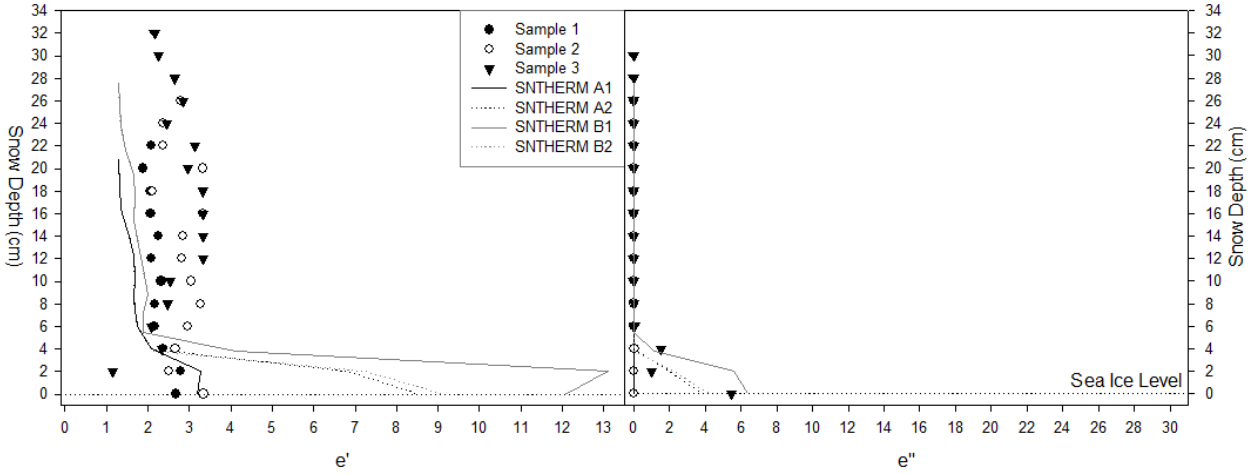

Figure 5.10. In-situ Sampled (1, 2, 3) dielectric permittivity (Left) and loss (Right), with the typical (SNTHERM 1) and low (SNTHERM 2) salinity values applied to the SNTHERM snow profiles input to the MSIB.

5.4.2 MSIB backscatter signature comparison

The MSIB simulations using SNTHERM snow simulations result in backscatter values in the range of first-year sea ice (Figure 5.11) (Carsey 1992; Nghiem et al. 1995b; Geldsetzer et al. 2007; Fuller et al. 2014). The relatively smaller grain sizes, lower densities, and greater dielectric permittivity and loss of SNTHERM A1 (bare ice initial condition, typical salinity profile) lead to low surface (incidence angles ~<30°) and volume scattering (incidence angles ~>30°). However when the salinity is reduced to profiled in-situ averages (SNTHERM A2), surface scattering increases by ~4 dB, while volume scattering remains low with a less than 1.5 dB increase for incidence angles greater than 45°. A similar trend is observed in the SNTHERM B (10 cm snow initial condition) for the two applied salinity profiles. Here the relatively larger simulated grain size and higher densities results in greater backscatter over all incidence angles, for each salinity profile, respectively. Although the salinity profile is the same as measured, the temperatures in the SNTHERM snowpack are higher, which results in higher dielectric permittivity and loss for

SNTHERM A and B cases, when compared with in-situ derived MSIB simulations (Figure 5.11). The SNTHERM B2 (10 cm initial snow condition, in-situ salinity profile) backscatter signature is within 1 dB of the Sample 1 MSIB simulated backscatter for all incident angles, and for both polarization configurations. This indicates that it is possible to find agreement in backscatter signatures between NARR driven SNTERHM snow outputs (B2), and those simulated from in-situ snow parameters (Sample 1). However, the lower correlations of NARR data relative humidity and longwave incoming radiation, results in inaccurate snow temperatures, thereby affecting dielectric properties. The inability of SNTHERM89.rev4 to simulate brine wicking in the snow cover also affects the simulated thermodynamic response, and requires the application of predetermined or in-situ salinity profiles.

The backscatter signatures simulated from NARR driven SNTHERM snow outputs (A2, B2) are within 2 dB of observed for incidence angles less than 30°. This indicates that surface scattering may be simulated from SNTHERM profiles, when the in-situ salinity profiles are applied. However, there is less agreement (4 to 6 dB difference) with regard to volume scattering, at incidence angles between 30° and 55° (Figure 5.11). The SNTHERM based simulations are less reliable, when compared to the relationship between the observed backscatter and the simulated backscatter for the average of Sample 1 and 3. Sample 1 and 3 represented in-situ snow end member conditions (Fuller et al. 2014). The averaged backscatter for Samples 1 and 3, show agreement within 2 dB for all incident angels for σ^0_{HH} observed backscatter, and the same for observed σ^0_{VV} backscatter for incident angle less than 55°. The observed and simulated backscatter for Samples 1 through 3 are in the backscatter region of first-year to multi-year sea ice. This was caused by a complexly-layered snowpack, with a superimposed fresh ice layer

overlying the first-year sea ice, and with several rough and discontinuous low and mid-pack ice layers, which suppressed brine wicking into the snow and is fully explored in Fuller et al. (2014).

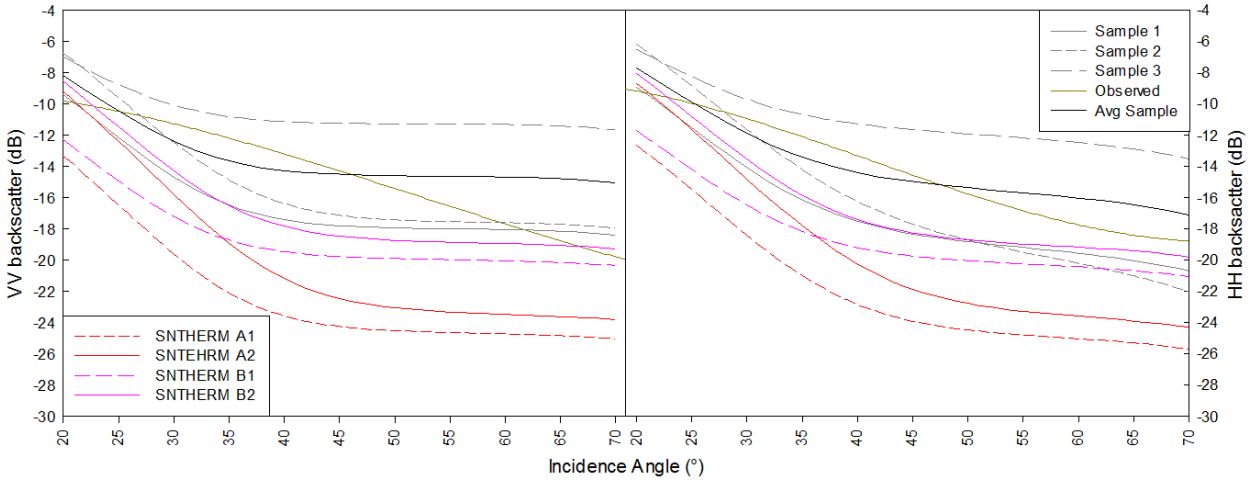

Figure 5.11. Comparison of simulated MSIB backscatter from Samples 1, 2, and 3, and SNTHERM snow outputs A (1, 2) and B(1, 2). The 'Avg Sample' is from Samples 1 and 3, representing end members of snow condition. Observed backscatter is a cubic fit, per (Fuller et al. 2014).

5.5 Summary and Conclusions

Within the context of state-of-the-art data assimilation techniques, snow physical models may be used to drive backscatter models for comparison and optimization with satellite observations, for extrapolation to large scales with sparse in-situ observation stations (Durand 2007). North American Regional Reanalysis (NARR) data was input to the SNTHERM snow thermodynamic model (Jordan 1991), in order to drive the multilayer snow and ice backscatter (MSIB) model (Scharien et al. 2010). Previous work with the MSIB model has shown that fresh ice layers superimposed over first-year sea ice are particularly relevant to C-band backscatter through the suppression of brine wicking and associated dielectric properties (Fuller et al. 2014). Therefore, a

snow thermodynamic model should be able to accurately capture these key snow properties, in order to drive backscatter models. The novel end-to-end assessment conducted here addresses our research questions:

1) How does NARR compare to in-situ meteorological data with regard to variables pertinent to SNTHERM89.rev4?

The NARR data shows reasonable agreement with in-situ air temperature and wind speed measurements, but poor correlation to relative humidity. There is good correlation via a proxy comparison to in-situ solar radiation, and poor correlation with longwave incoming radiation. A significant comparison between specific NARR and in-situ precipitation amounts was not possible; however, some general agreement can be observed. The NARR incoming and outgoing solar radiation resulted in an albedo that was not representative of snow on first-year sea ice. Therefore, this was adjusted to a higher and more representative value before input to SNTHERM.

2) How does SNTHERM89.rev4 output compare to in-situ snow structure and geophysical properties pertinent to C-band microwave backscatter over first-year sea ice?

SNTHERM89.rev4 reasonably captured grain size and lower snowpack density, but slightly underestimated snow density for uppermost layers of the snowpack. It did not accurately capture the snow temperature; however, this was likely due to the low correlation of NARR incoming longwave radiation, and relative humidity, which affect heat flux through the snowpack (Lapo et al. 2015). The simulations did not capture ice lenses formed due to rain events, which contribute SWE and can influence temperature, grain morphology, and brine profiles. SNTHERM

artificially removes gravimetrically drained water from the bottom of the snowpack, which removed up to 12 mm of SWE, when compared to NARR precipitation inputs. Additionally, the SNTHERM SWE values were low compared to in-situ observations, and are sensitive to initial condition (Willmes et al. 2014). The 1-dimensional nature of the model, likely also resulted in an inability to account for snow advection via wind transport from available nearby snow accumulation zones. The publicly available SNTHERM89.rev4 accounts for sea ice thermodynamic processes, with regard to the effects of salinity on conductivity, through layered inputs; however, it does not simulate brine wicking from sea ice to the basal snow layers, which is a key concern to microwave backscatter. The effective simulation of brine in the snow is important as brine suppresses both heating and cooling through brine solution and precipitation, which maintains a thermal equilibrium. Therefore, simulating the effects of brine on thermodynamic (such as temperature, albedo, longwave emission) and physical processes (such as effects of brine on basal snow grain development) is also important to accurate SNTHERM snow simulations, with regard to key physical and dielectric properties controlling microwave backscatter.

3) How do simulated backscatter signatures based on SNTHERM89.rev4 output compare to simulations from observed snow structure and properties, and observed backscatter for complexly-layered snow over first year sea ice?

The backscatter signatures simulated from NARR driven SNTHERM snow outputs (A2, B2) are within 2 dB of observed for incidence angles less than 30°, which indicates that surface scattering may be simulated from SNTHERM profiles, when the in-situ salinity profiles are applied. However, there is less agreement (4 to 6 dB difference) with regard to volume

scattering, at incidence angles between 30° and 55° (Figure 5.11). The SNTHERM B2 (10 cm initial snow condition, in-situ salinity profile) backscatter signature is with 1 dB of the Sample 1 (in-situ geophysical measurements) MSIB simulated backscatter for all incident angles for both polarization configurations. This result holds promise for simulating snow on sea ice with regard to backscatter signatures. The remainder of the cases were in the backscatter range of first-year sea ice; however, backscatter intensity was lower than that of comparative in-situ driven (Sample 1, 2, 3) MISB simulations. The most representative SNTHERM driven MSIB simulation was 4 to 6 dB lower when compared to observed backscatter, and when compared to the averaged in-situ Sample simulations (designed to account for in-situ snowpack end members, and which is within 1 dB of observed backscatter), particularly at incidence angles greater than 30°. The application of in-situ salinity profiles to the SNTHERM snow outputs resulted in improvements for both the bare ice and snow on sea ice initial conditions, with regard to in-situ simulated and observed backscatter comparisons.

5.5.1 Implications for use of NARR and SNTHERM for operational data assimilation in the Arctic.

This first assessment shows that although, there is the possibility of achieving comparable MSIB simulated backscatter from both SNTHERM derived and in-situ snow geophysical samples for complexly-layered snow on first-year sea ice, there are several constraints and considerations for improvement. 1) SNTHERM is sensitive to biases in incoming longwave radiation (Lapo et al. 2015). Lower correlations and bias in NARR longwave data, when compared to in-situ measurements, needs to be addressed by either employing in-situ measurements of longwave radiation, constraining the effects of longwave error with snow surface temperature data (Lapo et al. 2015), or allowing SNTHERM to calculate incoming longwave radiation based on

observations of low, mid, and upper layers of cloud fraction and type. 2) The NARR outgoing solar radiation should be made to more accurately reflect conditions of snow on first-year sea ice, with regard to albedo. 3) The publicly available SNTHERM89.rev4 does not simulate brine wicking into the basal snow layer, which is an important component with regard to thermodynamic response, basal layer snow dielectrics, and microwave backscatter of snow on first-year sea-ice. This also controls grain morphology and snow density, important to microwave backscatter interpretation. 4) The ability of SNTHERM to simulate water accumulation and refreezing at the bottom and mid-layers of the snowpack, and brine wicking, is necessary to accurately simulate the thermodynamic fluxes resulting in that snow conditions that lead to the MSIB signatures in this study. Therefore, the current utility in using NARR data to drive SNTHERM89.rev4, may be in that melt events can be traced through the snowpack via SNTHERM outputs, to infer superimposed and mid-pack ice layers that may suppress brine wicking, and influence thermodynamic processes. This is important in the context developing C-band snow inversion and assimilation schemes, particularly when considering expected increases in late and early season rain and melt events and associated additional complexity to snowpack stratigraphy, thermodynamics, and backscatter as a result of a warming Arctic.

Chapter Six: **Summary and Conclusions**

Within the context of a warming Arctic, an increase in melt and rain events through the winter is expected to create relatively more complexly-layered snow covers on both land and sea ice. The effect of this increased complexly on observed and simulated microwave emission and backscatter requires investigation, as snow has typically been represented as a relatively homogeneous media in models. The rationale for this work has been to contribute new understanding of the role of a more complex representation of snow properties and processes to passive and active microwave remote sensing observations and microwave and thermodynamic snow modeling, for hydrologic and climate applications.

6.1 Overview

Chapter 1 presented the rationale, overarching research questions, and specific research objectives for this thesis. Chapter 2 provided background information for snow and ice thermodynamics and modeling, and passive and active microwave remote sensing and modeling of brightness temperature and backscatter. These are employed in the research papers comprising Chapters 3, 4, and 5. Chapter 3 presented plot-scale, detailed snow geophysical properties representing relatively simple to relatively complexly-layered snow covers, and associated observed and modeled C-band microwave backscatter. A multilayer snow and ice backscatter (MISB) model was used to iteratively add and subtract layered components of the complex snow cover in order to assess their impacts on overall backscatter. Chapter 4 employed the systematic excavation of snow layers, to compare observed and modeled plot-scale brightness temperature (TB) at 19 and 37 GHz, with regard to potential snow water equivalent (SWE) retrieval, snow type, grain size, and layered structure, for forest, fen, and drifted snow sites. In-situ snow geophysical measurements were input to the Helsinki University of Technology (HUT) multi-

layer snow emission model and performance was characterized by RMSE and MBE. The contribution of snow type, SWE, and grain size to layers of simulated and observed TB was evaluated. Chapter 5 presented a simple operational application of North American Regional Reanalysis (NARR) meteorological data, to drive the publicly available and well validated SNTHERM89.rev4 thermodynamic snow model. Comparison with case-studies of observed snow properties and with plot-scale modeled and observed backscatter for layered snow on first-year sea ice. SNTHERM89.rev4 driven backscatter simulations were compared to that from in-situ snow geophysical properties, and to observed backscatter.

6.2 Summary of Chapters

The motivation for this thesis was generated by a number of overarching scientific research questions, namely;

a) How does a more complexly-layered representation of snow impact active and passive microwave remote sensing retrievals, with regard to snow type, structure, and microstructure?

b) What are the key snow layer types pertinent to a more complex representation of snow in passive and active remote sensing over land and sea ice, respectively?

c) How well are these represented in microwave emission and backscatter simulations?

d) What are the implications of employing a snow thermodynamic model, with regard to simulation of the layered components of snow physical and electrical properties, key to microwave simulations and observations, with regard to a simple operational assimilation technique?

These questions were investigated by the research focused questions addressed in the collection of papers that comprise this work:

6.2.1 Chapter 3

1. What are the observed geophysical characteristics and C-band backscatter signatures for a complexly-layered snow cover on first-year sea ice?

For complexly-layered snow, the brine and density characteristics, which affect dielectric and thermodynamic properties, differ from that of simple snow. The mid-snow pack ice layers, when present, increase density above typical values, and the superimposed ice layer serves to diminish the amount of brine in the depth hoar at the snow–ice interface by about half, when compared with that of a typical simple snow cover. For complexly-layered snow on smooth first-year sea ice, the observed magnitude of σ^0_{VV}, σ^0_{HH} and σ^0_{HV} is greater than for a simple snowpack of equal depth; more closely mimicking that of rough FYI, or even MYI.

2. How do observed and modeled C-band backscatter compare for a complexly-layered snow cover over first-year sea ice?

Model results show good agreement with the observed backscatter when spatial heterogeneity is accounted for through averaging. The averaged model results are within 2 dB for most incidence angles, but overestimate backscatter (more pronounced for $\sigma°_{VV}$) at incident angles greater than 55°.

3. How do the components of a complexly-layered snow contribute to C-band backscatter simulations over first-year sea ice?

The model runs indicate that with both the mid-snow pack and superimposed surface ice layer, the results agree well with observed backscatter for complexly-layered snow. When both of these layers are replaced with the properties of adjacent snow in the model, the simulated results agree well with that of a simple snow cover. Model results suggest that the superimposed ice layer contributes the most to the observed backscatter increase, and that even in the absence of a superimposed ice layer, the mid snowpack layer would cause a significant increase in backscatter at small incidence angles, when compared with a typical simple snow cover.

4. What are the implications to microwave backscatter classification of sea ice?

The snow pack layering and general lack of brine within the snowpack have implications for sea ice classification particularly with regard to FYI and MYI discrimination. It also has potential implications for melt timing and melt rate of first-year sea ice. The superimposition of rough, relatively fresh ice over first-year sea ice has implications for microwave backscatter response, as snow dielectrics are affected through hindrance of brine wicking from the ice surface to internal layers. The differences in backscatter signatures for complexly-layered and simple snow are likely due to dielectric permittivity and loss variations, associated with different brine and density profiles in the snow pack. This likely has implications for geophysical retrieval and classification strategies of first-year sea ice that are based on microwave backscatter.

6.2.2 Chapter 4

5. How are scattering contributions for key snow layers and properties represented in the multilayer Helsinki University of Technology (HUT) snow microwave emission simulations, when compared to 19 and 37 GHz dual polarization (V, H) observations?

The results in this work indicate that for all snow cover types, as the SWE increases above ~130 mm, the multi-layer HUT model produces T_B values that are less than observed, as HUT simulations show continued sensitivity to additional SWE. When considering model performance through the layers, the model closely simulates scattering due to large-grained depth hoar but does not capture that of windsalb located higher in the snowpack. The empirically derived extinction coefficient in the HUT model fails to capture the 37 GHz saturation and reversal. The greatest change in T_B occurs because of scattering generated by depth hoar at the bottom of the snowpack. Large SWE contributions from other snow types (windslab, recent snow) do not result in similar changes in observed T_B. This masking of SWE contribution for various snow types, by scattering from depth hoar that is disproportionate to its SWE contribution, complicates the linear relationship of 19V – 37V T_B for direct inversion of SWE. This leaves an average of 50% of SWE unaccounted for in this work. The addition of a depth hoar layer as input to the HUT radiative transfer model could more accurately account for the scattering of the 37V signal occurring due to depth hoar microstructure, which is generally underrepresented in single-layer HUT simulations. This may better capture the SWE held by the depth hoar, and better simulate the depth at which saturation occurs. In addition to the depth hoar layer, an upper snow or windslab layer consisting of smaller grained and higher density snow, may allow for development of a more representative extinction coefficient or saturation level, and more accurately account for SWE in the upper snowpack.

6. What are the implications for consideration of a multilayer HUT model in the GlobSnow SWE assimilation scheme?

The GlobSnow assimilation method (Pulliainen 2006) weights a single-layer HUT radiative transfer model estimation of SWE, optimized to remotely sensed microwave emission TB and available in-situ SD/SWE measurements, by their respective statistical uncertainties (Takala et al. 2011). The assimilation begins with an optimization to find an effective grain size. The single-layer HUT model is used with snow depth observations from weather stations and a fixed snow density, to fit modeled to observed T_B by varying grain size. The optimization of a single effective grain size integrates error from physical inputs (including vertical heterogeneity) and the T_B fitting processes, and is therefore not necessarily related to physical grain size. The initial accuracy of effective grain size, in the first stage of the assimilation, is essential to optimization and assimilation performance (Pulliainen 2006), as subsequently this grain size and its variance are then fixed to determine SWE. The unaccounted scattering from the depth hoar contributes error to the initial effective grain size calculations, which in turn affects the weighting of the model components through less accurate variance, creating increased overall error and bias. The inclusion of a depth hoar layer in the assimilation could better account for scattering contributions resulting in a more accurate initial effective grain size, which may be more closely related to physical grain size, and more accurate prediction of signal saturation associated with SWE. However, the continued sensitivity of the multiple-layer HUT model to SWE above saturation scattering must also be considered, so that the additional simulated T_B scattering is not incorporated when fitting the simulated T_B values to observations through effective grain size. This could increase the accuracy of snow depths and saturation scattering level, particularly later in the season and for greater snow depths. This is an important consideration for hydrological applications in sub-Arctic Canada as assimilation examples by both Takala (2011) and Pulliainen (2006) found increased RMSE for Canadian Arctic SWE retrievals. These increased RMSE

results were attributed to deeper snow cover and accompanying T_B saturation, increased spatial heterogeneity, and fewer observation stations.

6.2.3 Chapter 5

7) How does NARR compare to in-situ meteorological data with regard to variables pertinent to SNTHERM89.rev4?

The NARR data shows reasonable agreement with in-situ air temperature and wind speed measurements, but poor correlation to relative humidity. There is good correlation via a proxy comparison to in-situ solar radiation, and poor correlation with incoming longwave radiation. A significant comparison between specific NARR and in-situ precipitation amounts was not possible; however, some general agreement can be observed. The NARR incoming and outgoing solar radiation resulted in an albedo that was not representative of snow on first-year sea ice. Therefore, this was adjusted to a higher and more representative value before input to SNTHERM.

8) How does SNTHERM89.rev4 output compare to in-situ snow structure and geophysical properties pertinent to C-band microwave backscatter over first-year sea ice?

SNTHERM89.rev4 reasonably captured in situ measured grain size and lower snowpack density, but slightly underestimated snow density for uppermost layers of the snowpack. It did not accurately capture the snow temperature; however, this was likely due to the low correlation of NARR incoming longwave radiation, and relative humidity, which affect heat flux through the snowpack. The simulations did not capture ice lenses formed within the snowpack due to rain events, which contribute SWE and can influence temperature, grain morphology, and brine

profiles. SNTHERM artificially removes gravimetrically drained water from the bottom of the snowpack, which removed in up to 12 mm of SWE, when compared to NARR precipitation inputs. Additionally, the SNTHERM SWE values were low compared to in-situ observations, and are sensitive to initial condition. The 1-dimensional nature of the model, likely also resulted in an inability to account for snow advection via wind transport from available nearby snow accumulation zones. The publicly available SNTHERM89.rev4 accounts for sea ice thermodynamic processes, with regard to the effects of salinity on conductivity, through layered inputs. However, it does not simulate brine wicking from sea ice to the basal snow layers, which is a key concern to microwave backscatter contributions for first-year sea ice. The effective simulation of brine in the snow is important as brine suppresses both heating and cooling through brine solution and precipitation, which maintains a thermal equilibrium. Therefore, simulating the effects of brine on thermodynamic (such as temperature, albedo, longwave emission) and physical processes (such as effects of brine on basal snow grain development) is also important to accurate SNTHERM snow simulations, with regard to key physical and dielectric properties controlling microwave backscatter.

9) How do simulated backscatter signatures based on SNTHERM89.rev4 output compare to simulations from observed snow structure and properties, and observed backscatter for complexly-layered snow over first year sea ice?

The backscatter signatures simulated from NARR driven SNTHERM snow outputs (A2, B2) are within 2 dB of observed for incidence angles less than 30°, which indicates that surface scattering may be simulated from SNTHERM profiles, when the in-situ salinity profiles are applied. However, there is less agreement (4 to 6 dB difference) with regard to volume

scattering, at incidence angles between 30° and 55° (Figure 5.11). The SNTHERM B2 (10 cm initial snow condition, in-situ salinity profile) backscatter signature is with 1 dB of the Sample 1 (in-situ geophysical measurements) MSIB simulated backscatter for all incident angles for both polarization configurations. This result holds promise for simulating snow on sea ice with regard to backscatter signatures. The remainder of the cases were in the backscatter range of first-year sea ice; however, backscatter intensity was lower than that of comparative in-situ driven (Sample 1, 2, 3) MISB simulations. The most representative SNTHERM driven MSIB simulation was 4 to 6 dB lower than observed backscatter, and when compared to the averaged in-situ Sample simulations (designed to account for in-situ snowpack end members, and which is within 1 dB of observed backscatter), particularly at incidence angles greater than 30°. The application of in-situ salinity profiles to the SNTHERM snow outputs resulted in improvements for both the bare ice and snow on sea ice initial conditions, when compared to in-situ simulated and observed backscatter.

10) What are the implications for the use of the SNTHERM89.rev4 thermodynamic model in an operational scenario for simulation of C-band backscatter over first-year sea ice?

Although there is the possibility of achieving comparable MSIB simulated backscatter from both SNTHERM derived and in-situ snow geophysical samples, there are several constraints and considerations for improvement. 1) SNTHERM is sensitive to biases in incoming longwave radiation. Lower correlations and bias in NARR longwave data, when compared to in-situ measurements, needs to be addressed by either employing in-situ measurements of longwave radiation, constraining the effects of longwave error with snow surface temperature data, or allowing SNTHERM to calculate incoming longwave radiation based on observations of low,

mid, and upper layers of cloud fraction and type. 2) The NARR outgoing solar radiation should be made to more accurately reflect conditions of snow on first-year sea ice, with regard to corresponding surface albedo. 3) The publicly available SNTHERM89.rev4 does not simulate brine wicking into the basal snow layer, which is an important component with regard to thermodynamic response, basal layer snow dielectrics, and microwave backscatter of snow on first-year sea-ice. This also controls grain morphology and snow density, important to microwave backscatter interpretation. 4) The ability of SNTHERM to simulate water accumulation and refreezing at the bottom and mid-layers of the snowpack, and brine wicking, is necessary to accurately simulate the thermodynamic fluxes resulting in snow conditions that lead to the MSIB signatures in this study. Therefore, the current utility in using NARR data to drive SNTHERM89.rev4, may be in that melt events can be traced through the snowpack via SNTHERM outputs, to infer superimposed and mid-pack ice layers that may suppress brine wicking, and influence thermodynamic processes. This is important in the context developing C-band snow inversion and assimilation schemes, particularly when considering expected increases in late and early season rain and melt events and associated additional complexity to snowpack stratigraphy, thermodynamics, and backscatter as a result of a warming Arctic.

6.3 Limitations and Future Considerations

The results throughout this work are limited in that they present plot-scale case studies, which was necessary for comparison of observations and simulations when considering the high spatial and temporal variation in snow properties. These are considered a first-step and, therefore, the extrapolation of these specific results to larger spatial scales may not be valid. Additionally, the results are a product of a series of measurement techniques, decisions, and assumptions

regarding the physical character of snow, meteorological variables, thermodynamics, and microwave observations and simulations. Therefore, these results are indicative of those choices and these models, and may not be applicable to other modeling or measurement scenarios.

Recommendations for future work based on Chapter 3 include a broadening of observations and simulations to a seasonal scale and for larger areas of relatively complex snow layering, in order to achieve a fully detailed representation of the evolutionary characterization of snow physical, thermodynamic, dielectric, and microwave observations and simulations and for upscaling to fully polarimetric satellite based imagery. Recommendations for future research stemming from the results of Chapter 4 include addressing the apparent shortcoming of the extinction coefficient in the multilayered HUT model, and testing of the multilayered model in the GlobSnow SWE assimilation scheme. Work currently being conducted investigates the application of detailed in-situ seasonal meteorological data (best case scenario) collected near Churchill in the winter of 2010. This work is being conducted to assess the ability of SNTHERM to characterize the relative proportions of depth hoar and windslab to more accurately simulate emission using the multilayer HUT model. This is toward more accurate assimilation of SWE over land within the context of the GlobSnow assimilation scheme. Future work suggested from results presented in Chapter 5 should consider the operational application of higher resolution Global Environment Multiscale (GEM) model data to an updated version of the SNTHERM snow model which considers brine wicking into snow on first-year ice types. This should be considered at plot, seasonal, and regional scales.

6.4 Concluding Remarks and the Path Forward

An expected increase in the frequency and magnitude of both early and late and winter season rain and melt events in the Arctic is likely to cause further complexities in the interpretation and characterization of snow grain morphology, depth, density, SWE, and electrical properties, which are specifically of interest in the interpretation of microwave remote sensing data. The stratigraphy of snowpacks continuously influences snow cover characteristics through effects on geophysical, thermodynamic, and dielectric processes, affecting microwave emission and scattering as the snowpack matures over the course of a season. Changes in snowpack parameters associated with meteorological events and seasonal metamorphosis are detectable as changes in microwave backscatter and emission signatures with snow cover. The metamorphosis of snowpack layers, grain size, and morphology occur at different rates depending on the thickness and structure of the snow cover, due to differing thermal capacity, conductivity, diffusivity, and albedo. Current state-of-the art assimilations are focused toward providing estimates for large areas with few in-situ observations, as exemplified by the Canadian Arctic.

In answer of the overarching questions posed by this thesis (a through d), the results of this work demonstrate that a more realistic representation of snow (i.e. a more complexly-layered representation) is required to improve accuracy of microwave emission and backscatter simulations. The accounting for constituent snow properties, layering, and types over land and sea ice is necessary within the context of a warming Arctic. For both active and passive retrievals, the layers pertinent to a more complex-representation of snow are depth hoar, wind slab, and ice lenses. Although the position and thickness of ice lenses have been shown to impact passive microwave emission for simulations in models which consider coherent scattering, ice

lenses contribute less change in emission with regard to the multilayer HUT model, which does not consider coherent scattering. As such these may be of relatively less importance with regard to this specific emission model. The position and roughness of ice lenses, and brine content and distribution, are additional components affecting sea ice microwave observations and simulations for the frequencies and backscatter model chosen for this work. While individual, relatively homogeneous snow layers can be well represented by HUT emission and MSIB backscatter simulations, there are limitations to each when considering more complexly-layered model representations. The HUT simulations are capable of modeling of depth hoar and wind slab independently; however, issues with saturation, caused the scattering by larger depth hoar grains, result in a masking of observed scattering contribution by windslab. The HUT model does not currently capture this phenomena, and instead demonstrates continued scattering due to windslab. These compounding issues lead to inaccuracies in emission and may be multiplied through the GlobSnow assimilation technique. The MSIB simulations over sea ice agree with observed backscatter when spatial variability is taken into account. Sensitivity analysis conducted through simulations suggest that suppression of brine by ice lenses and the rough ice lenses themselves, contribute to backscatter intensity that is ignored in simple, homogenous representations of snow on first year sea ice. Finally, while snow thermodynamic models may be able to provide ancillary information with regard to the layered components of snow pertinent to simulations of backscatter over first-year sea ice, there are many constraints which must be considered in the development of a simple operational assimilation or classification technique.

The path forward with regard to the GlobSnow assimilation technique lies in the inclusion of depth hoar and windslab layers in the multilayer HUT model, and the implementation of a snow

thermodynamic model to estimate proportions and properties (e.g. grain size, density) of depth hoar and windslab. This should allow for more accurate estimations of emission scattering and extinction from each layered component of snow, and its associated geophysical characteristics. Currently, single layer HUT simulated emission is compared to observed satellite brightness temperatures in an optimization process which varies grain size alone. This grain optimization process currently integrates error in scattering simulations, physical snow properties, and atmospheric and landcover properties. This optimized grain value then becomes the basis for estimates of spatial variance of snow properties and statistical weighting of each component of the GlobSnow assimilation process. The more realistic and more complexly-layered representation of snow types, layering, properties, and proportions should allow for a more accurate accounting of emission contributions from each snow type and from their vertical organization. This in turn can reduce the error currently integrated into the optimized grain size, resulting in more accurate SWE estimates for use in hydrologic and climate applications.

The path forward with regard to the classification and estimation of snow cover on first-year sea ice involves development of a more robust coupled snow and sea ice classification technique to reduce uncertainty in sea ice charts caused by surface snow condition. This issue should be approached with the combination of several techniques. High resolution GEM atmospheric state variables can to force a snow thermodynamic model which should be capable of simulating the effects of sea ice and snow layering components. These components and processes should include depth hoar, wind slab, and ice lenses; their character, proportions, and positions; and the effects of these components on brine volume and brine wicking. This should be coupled with fully polarimetric, multi-frequency, microwave retrievals, which can provide further

backscattering information regarding snow structure and layering. The integration of these data can allow for the development of a classification and assimilation process to better predict the physical cause of polarimetric backscatter results, thereby increasing accuracy of sea ice classification and ice and snow quantification, which impacts hydrologic, transport, and climate applications.

More generally, this work provides a broad foundation toward more complex representations of snow cover, in order to eventually develop modeling processes for geophysical inversion of snow properties employing active and passive remote sensing, and snow observations and thermodynamic simulations. Ideally, future development of snow and ice assimilation techniques will result in a single assimilation technique which integrates multi-frequency, multi-polarization and polarimetric, passive and active microwave remote sensing acquisitions, with versatile snow thermodynamic simulations capable over both land and sea ice driven by high quality, high resolution atmospheric state variables. The overarching purpose of this effort is toward better quantification of the contributions of snow and ice in climate and hydrologic applications.

References

Ambach W. 1974. The influence of fractional cloud cover on the net radiation balance of a snow surface with high albedo. Journal of Glaciology. 67: 73-84

Ambach W and Denoth, A.1980. The dielectric behavior of snow: A study versus liquid water content. Ft. Collins, Colorado: NASA Workshop on the Microwave Remote Sensing Properties of Snowpack.

Andreas E. 1987. A theory for the scalar roughness and the scalar transfer coefficients over snow and sea ice. Boundary Layer Meteorology. 38: 159-184

Andreas E. 2002. Parameterizing scalar transfer over snow and ice: A review. Journal of Hydrometeorology. 3:417-432

Andreas E, Jordan R, Makshtas A. 2004. Simulations of snow, ice, and near surface atmospheric processes on Ice Station Weddell. Journal of Hydrometeorology. 5: 611-624

Andreadis K and Lettenmaier D. 2006. Assimilating remotely sensed snow observations into a macroscale hydrology model. Advances in Water Resources. 29(6): 872-886 doi:10.1016/j.advwatres.2005.08.004

Armstrong R. 1980. An analysis of compressive strain in adjacent temperature gradient and equi-temperature layers in a natural snow cover. Journal of Glaciology. 26(94): 283-289

Arons E and Colbeck S. 1995. Geometry of heat and mass transfer in dry snow: a review of theory and experiment. Reviews of Geophysics. 33(4): 463-493

Barber D, Galley R., Asplin M, De Abreu R, Warner K, Pucko M, Gupta M, Prinsenberg S, Julien S. 2009. Perennial pack ice in the southern Beaufort Sea was not as it appeared in the summer of 2009. Geophysical Research Letters: 36(L24501)

Barber D and LeDrew E. 1994. On the links between microwave and solar wavelength interactions with snow-covered first-year sea ice. Arctic. 47(3): 298-309

Barber D, Nghiem SV. 1999. The role of snow on the thermal dependence of microwave backscatter over sea ice. Journal of Geophysical Research 104(C11) : 25789-25803

Barber D, Papakyriakou T, LeDrew E. 1994. On the relationship between energy fluxes, dielectric properties, and microwave scattering over snow covered first-year sea ice during the spring transition period. Journal of Geophysical Research. 99(C11): 22401-22411

Barber D, Reddan S, LeDrew E. 1995. Statistical characterization of the geophysical and electrical properties of snow on landfast first-year sea ice. Journal of Geophysical Research. 100(C2): 2673-2686

Barber D and Thomas A. 1998. The influence of cloud cover on the radiation budget, physical properties, and microwave scattering coefficient (sigma naught) of first-year and multiyear sea ice. IEEE Transactions on Geoscience and Remote Sensing. 36(1): 38-50

Bean B and Dutton E. 1967. Dielectric behaviour of heterogeneous systems. In B. L. H, and J. B. Birks (Ed.), Progress in Dielectrics (Vol. 7, pp. 67 - 114). London: Dover Publishing, New York.

Behari J. 2005. Microwave Dielectric Behavior of Wet Soils. New York: Springer.

Berger R. 1979. Snowpack optical properties in the infrared. Hanover, NH: US Army Cold Region Research and Engineering Lab.

Bernier M and Fortin J. 1998. The potential of time series SAR to monitor dry and shallow snow cover. IEEE Transactions on Geoscience and Remote Sensing 36(1): 226-243

Bitz, C and Lipscomb W. 1999. An energy-conserving thermodynamic model of sea ice. Journal of Geophysical Research. 104(C7): 15669-15667

Bohren C and Barkstrom B. 1974. Theory of the optical properties of snow. Journal of Geophysical Research. 79(30): 4527-4535

Box J, Fettweis X, Stroeve J, Tedesco M, Hall D, Steffen K. 2012. Greenland ice sheet albedo feedback: thermodynamics and atmospheric drivers. The Cryosphere. 6: 821-839

Bradford J, Harper J, Brown J. 2009. Complex dielectric measurements from ground-penetrating radar data to estimate snow liquid water content in pendular regime. Water Resources Research. 45: 12

Brown R and Braaten R. 1998. Spatial and temporal variability of Canadian monthly snow depths, 1946-1995. Atmosphere-Ocean. 36(1): 37-54 doi:10.1080/07055900.1998.9649605

Brown R, Walker A, Goodison B. 2000. Seasonal snow cover monitoring in Canada: an assessment of Canadian contributions for global climate monitoring. The Proceedings of the 57th Eastern Snow Conference. Syracuse, NY.

Budyko M. 1969. The effect of solar radiation variations on the climate of the Earth. Tellus, XXI(5): 611-619

Campbell B. 2002. Radar Remote Sensing of Planetary Surfaces. Cambridge, UK: Cambridge University Press.

Chang A., Foster J, Hall D. 1987a. NIMBUS-7 SMMR derived global snow cover parameters. Annals of Glaciology. 9: 39-44

Chang A, Foster J, Hall D 1987b. Microwave snow signatures (1.5 mm to 3 cm) over Alaska. Cold Regions Science and Technology. 13: 153-160

Chang A, Foster J, Hall D. 1990. Satellite sensor estimates of Northern Hemisphere snow volume. International Journal of Remote Sensing. 11(1): 167-171 doi:10.1080/01431169008955009

Chang P, Mead J, Knapp E, Sadowy G, Davis R, McIntosh R. 1996. Polarimetric backscatter from fresh and metamorphic snow cover at millimeter wavelengths. IEEE Transactions on Antennas and Propagation. 40(1): 58-73

Carsey, F. (Ed.). 1992. Microwave remote sensing of sea ice (Vol. Geophysical Monograph Series). Washington D.C.: American Geophysical Union.

Chen C, Tsang L, Guo J, Chang A, Ding K. 2003. Frequency dependence of scattering and extinction of dense media based on three-dimensional simulations of Maxwell's equations with applications to snow. IEEE Transactions on Geoscience and Remote Sensing. 41(8): 1844-1852

Choudhury B and Chang A. 1979. Solar reflectance of a snow field. Cold Regions Science and Technology. 1: 121-128

Colbeck S. 1974. The capillary effects on water percolation in homogeneous snow. Journal of Glaciology. 85-97

Colbeck S. 1983. Theory of metamorphism of dry snow. Journal of Geophysical Research. 88(C9): 5475-5482.

Colbeck S. 1982. The geometry and permittivity of snow at high frequencies. Journal of Applied Physics. 53(6): 4495-4500

Colbeck S. 1991. The layered character of snow covers. Reviews of Geophysics. 29(1): 81-96 doi:10.1029/90RG02351

Colbeck S, Akitaya E, Armstrong, R, Gubler H, Lafeuille J, Lied K, McClung D, Morris, E. 1990. The International Classification for Seasonal Snow on the Ground. International

Commission on Snow and Ice (IAHS), World Data Center A for Glaciology, University of Colorado, Boulder, CO, USA.

Colbeck, S and Jamieson B. 2001. The formation of faceted layers above crusts. Cold Regions Science and Technology. 33(2-3): 247-252. doi:10.1016/S0165-232X(01)00045-3

Cox G and Weeks W. 1975. Brine drainage and initial salt entrapment in sodium chloride ice. U.S. Army Cold Regions Research and Engineering Laboratory. Research Report 345.

Cox G and Weeks W. 1988. Numerical simulation of the profile properties of undeformed first year sea ice during the growth season. Journal of Geophysical Research. 93: 12449-12460

Crocker G. 1984. A physical model for predicting the thermal conductivity of brine-wetted snow. Cold Regions Science and Technology. 10(1): 69-74

Crocker G. 1992. Observations of snow cover on sea ice in the Gulf of Bothnia. International Journal of Remote Sensing. 13(13): 2433-2445 doi:10.1080/01431169208904280

Curry J, Rossow W, Randall D, Schramm J. 1996. Overview of Arctic cloud radiation characteristics. Journal of Climate. 9(8): 1731-1764

Curry J, Schramm J, Ebert E. 1995. Sea ice-albedo climate feedback mechanism. Journal of Climate. 8: 240-247

De Seve D, Bernier M, Fortin J, Walker A. 1997. Preliminary analysis of snow microwave radiometry using the SSM/I passive-microwave data: the case of La Grande River watershed (Quebec). Annals of Glaciology. 25: 353-361

Denoth A. 1999. Wet snow pendular regime: the amount of water in ring-shaped configurations. Cold Regions Science and Technology. 30: 13-18

Denoth A. 1982. The pendular-funicular liquid transition and snow metamorphism. Journal of Glaciology. 28(99): 357-364

Derksen C. 2008. The contribution of AMSR-E 18.7 and 10.7 GHz measurements to improved boreal forest snow water equivalent retrievals. Remote Sensing of Environment. 112: 2701-2710

Derksen C, LeDrew E, Goodison B. 2000. Temporal and spatial variability of North American prairie snow cover (1988-1995) inferred from passive microwave derived snow water equivalent imagery. Water Resources Research. 36(1): 255-266 doi:10.1029/1999WR900208

Derksen C, LeDrew E, Walker A, Goodison B. 2000. Influence of overpass time on passive microwave-derived snow cover parameters. Remote Sensing of Environment. 71: 297-308

Derksen C, Lemmetyinen J, Toose P, Silis A, Pulliainen J, Sturm M. 2014. Physical properties of Arctic versus subarctic snow: Implications for high latitude passive microwave snow water equivalent retrievals. Journal of Geophysical Research. 119(12): 7254–7270

Derksen C, Toose P, Lemmetyinen J, Pulliainen J, Langlois A, Rutter N, Fuller M. 2012. Evaluation of passive microwave retrieval brightness temperature simulations and snow water equivalent retrievals through a winter season. Remote Sensing of Environment. 117: 236-248 doi:10.1016/j.rse.2011.09.021

Derksen C, Walker A, Goodison B. 2005. Evaluation of passive microwave snow water equivalent retrievals across the Boreal forest / tundra transition of western Canada. Remote Sensing of Environment. 96: 315-327

Derksen, C., J. Lemmetyinen, P. Toose, A. Silis, J. Pulliainen, and M. Sturm. (2014). Physical properties of Arctic versus subarctic snow: Implications for high latitude passive microwave snow water equivalent retrievals. Journal of Geophysical Research. 119(12): 7254–7270 DOI: 10.1002/2013JD021264.

Drinkwater M. 1989. LIMEX'87 ice surface characteristics: Implications for C-band SAR backscatter signatures. IEEE Transactions on Geoscience and Remote Sensing. 27: 501-513

Drinkwater M and Crocker G. 1988. Modeling changes in the dielectric and scattering properties of young snow-covered sea ice at GHz frequencies. Journal of Glaciology. 34(118): 274-282

Drobot S and Barber D. 1998. Towards development of a snow water equivalence (SWE) algorithm using microwave radiometry over snow covered first-year sea ice. Photogrammetric Engineering and Remote Sensing. 64: 415-423

Duguay C, Green J, Derksen C, English M, Rees A, Sturm M, Walker A. 2005. Preliminary assessment of the impact of lakes on passive microwave snow retrieval algorithms in the Arctic. 62nd Eastern Snow Conference. 223-228. Waterloo, Ontario.

Dunkle R and Bevans J. 1956. An approximate analysis of the solar reflectance and transmittance of a snow cover. Journal of Meteorology. 13(2): 212-216

Durand M. 2007. Feasibility of snowpack characterization using a multi-frequency data assimilation scheme. Doctor of Philosophy Thesis. Los Angeles, CA: UMI Microform, Proquest LLC.

Durand M and Margulis S. 2006. Feasibility test of multifrequency radiometric data assimilation to estimate snow water equivalent. Journal of Hydrometeorology. 7: 443-457

Durand M and Margulis S. 2007. Correcting first-order errors in snow water equivalent estimates using a multifrequency, multiscale radiometric data assimilation scheme. Journal of Geophysical Research. 112(D13121): 1-15

Durand M, Kim E, Margulis S. 2008. Quantifying uncertainty in modeling snow microwave radiance for a mountain snowpack at the point-scale, including stratigraphic effects. IEEE Transactions on Geoscience and Remote Sensing. 46(6): 1753-1767

Durand M, Kim E, Margulis S, Molotch N. 2011. A first-order characterization of errors from neglecting stratigraphy in forward and inverse passive microwave modeling of snow. IEEE Transactions on Geoscience and Remote Sensing Letters. 8(4): 730-734

Ebert E and Curry J. 1992. A parameterization of ice cloud optical properties for climate models. Journal of Geophysical Research. 97: 3831-3836

Ebert E and Curry J. 1993. An intermediate one-dimensional thermodynamic sea ice model for investigating ice-atmosphere interactions. Journal of Geophysical Research. 98: 10085-10109

Escorihuela M, deRosnay P, Kerr Y, Calvet, J. 2007. Influence of bound-water relaxation frequency on soil moisture measurements. IEEE Transactions on Geoscience and Remote Sensing. 45(12): 4067-4076

Essery R, Morin S, Lejune Y, Menard C. 2013. A comparison of 1701 snow models using observations from an alpine site. Advances in Water Resources. 55: 131-148

Essery R and Pomeroy J. 2004. Vegetation and topography control of wind-blown snow distributions in distributed and aggregated simulations for an Arctic tundra basin. Journal of Hydrometeorology. 5: 735-744

Fierz C, Armstrong R, Durand Y, Etchevers P, Greene E, McClung D, NishimuraK, Satyawali P, Sokratov S. 2009. The International Classification for Seasonal Snow on the Ground. IHP-

VII Technical Documents in Hydrology N°83, IACS Contribution N°1, UNESCO-IHP, Paris.

Foster J, Sun C, Walker J, Kelly R, Chang A, Dong J, Powell H. 2005. Quantifying the uncertainty in passive microwave snow water equivalent observations. Remote Sensing of Environment. 94: 187-203

Foster J, Chang A, Hall D. 1997. Comparison of snow mass estimates from a prototype passive microwave snow algorithm, a revised algorithm and a snow depth climatology. Remote Sensing of Environment. 62(2): 132-142 doi:10.1016/S0034-4257(97)00085-0

Francis J and Vavrus S. 2012. Evidence linking Arctic Amplification to extreme weather in mid-lattitudes. Geophysical Research Letters. 39: L06801

Fuller M. 2008. Monitoring snowcover in a discontinuous snow-covered region using active polarimetric C-band remote sensing. Master of Science Thesis. The University of Calgary.

Fuller M, Geldsetzer T, Yackel J. 2009. Surface-based polarimetric C-band microwave scatterometer measurements of snow during a Chinook event. IEEE Transactions on Geoscience and Remote Sensing. 47(6): 1766-1776.

Fuller M, Geldsetzer T, Gill J, Yackel J, Derksen C. 2014. C-band backscatter from a complexly-layered snow cover on first-year sea ice. Hydrological Processes. 28: 4641-4625 doi:10.1002/hyp.10255

Fung A. Microwave Scattering and Emission Models and Their Applications. Norwood: Artech House, Inc., 1994.

Gallet J, Domine F, Zender C, Picard G. 2009. Measurement of the specific surface area of snow using infrared reflectance in an integrating sphere at 1310 and 1550 nm. The Cryosphere. 3: 167-182

Geldsetzer T, Langlois A, Yackel J. 2009. Dielectric properties of brine-wetted snow on first-year sea ice. Cold Regions Science and Technology. 58: 47-56

Geldsetzer T, Mead J, Yackel J, Scharien R, Howell S. 2007. Surface-based polarimetric C-band scatterometer for field measurements of sea ice. IEEE Transactions on Geoscience and Remote Sensing. 45(11): 3405-3416

Giddings J and LaChapelle E. 1961. Diffusion theory applied to radiant energy distribution and albedo of snow. Journal of Geophysical Research. 66: 181-189

Gill J and Yackel J. 2012. Evaluation of C-band SAR polarimetric parameters for discrimination of first-year sea ice types. Canadian Journal of Remote Sensing. 38(3): 306-323

Gill J, Yackel J, Geldsetzer T. 2014. Analysis of consistency in first-year sea ice classification potential of C-band SAR polarimetric parameters. Canadian Journal of Remote Sensing. 39(2): 101-117

Golding M, Broup D, Cheney M, Cherkaeva E, Dawson M, Ding K-H, Fung A, Isaacson D, Johnson S, Jordan A, Kong J, Kwok R, Nghiem S, Onsott R, Winebrenner D, Zabel I. 1998. Inverse electromagnetic scattering models for sea ice. IEEE Transactions on Geoscience and Remote Sensing. 36(5): 1675-1704

Goodison B. and Louie P. 1986. Canadian methods for precipitation measurement and correction. Workshop on the correction of Precipitation Measurements. Zurich, Switzerland. April 1-3. pp. 141-145

Gunn G, Duguay C, Derksen C, Lemmetyinen J, Toose P. 2011. Evaluation of the HUT modified snow emission model over lake ice using airborne passive microwave measurements. Remote Sensing of Environment. 15: 233-244

Hall D. 1987. Influence of depth hoar on microwave emission from snow in northern Alaska. Cold Regions Science and Technology. 13: 225-231

Hallikainen M. 1989. Microwave radiometry of snow. Advances in Space Research. 9(1): (1)267-(1)275

Hallikainen M and Jolma P. 1992. Comparison of algorithms for retrieval of snow water equivalent from Nimbus-7 SMMR data in Finland. IEEE Transactions on Geoscience and Remote Sensing. 30(1): 124-131 doi:10.1109/36.124222

Hallikainen M and Winebrenner D. 1992. The Physical Basis for Sea Ice Remote Sensing. In F. Carsey (Ed.), Microwave Remote Sensing of Sea Ice. American Geophysical Union, Geophysical Monograph.

Hallikainen M, Ulaby F, Abdelrazik M. 1986. Dielectric properties of snow in the 3 to 37 GHz range. IEEE Transactions on Antennas and Propagation. AP-34 (11): 1329-1340

Hallikainen M, Ulaby F, Abdel-Razik M. 1982. Measurements of the dielectric properties of snow in the 4-18GHz frequency range. 12th European Microwave Conference Proceedings

151-156. Kent, England: Microwave Exhibitions and Publishers Ltd. doi: 10.1109/EUMA.1982.333155

Hallikainen M, Ulaby F, Van Deventer T. 1987. Extinction behavior of dry snow in the 18- to 90-GHz range. IEEE Transactions on Geoscience and Remote Sensing. GE-25(6): 737-745

Hanesiak J. 2001. Development of a one-dimensional electro-thermophysical model of the snow sea-ice system: Arctic climate processes and microwave remote sensing applications. PhD Thesis. Winnipeg, Manitoba, Canada.

Hanesiak J and Wang X. 2005. Adverse-weather trends in the Canadian Arctic. Journal of Climate. 18: 3140-3156

Hanson K. 1961. Some Aspects of the thermal energy exchange on the South Polar snow field and Arctic ice pack. Monthly Weather Review. 89: 173-177

Harper J and Bradford J. 2003. Snow stratigraphy over a uniform depositional surface: spatial variability and measurement tools. Cold Regions Science and Technology. 37(3): 289-298 doi:10.1016/S0165-232X(03)00071-5

Holland M, Finnis J, Serreze M. 2006. Simulated Arctic Ocean freshwater budgets in the twentieth and twentyfirst centuries. Journal of Climate. 19: 6221-6242

Holland M, Finnis J, Barrett A, Serreze M. 2007. Projected changes in Arctic Ocean freshwater budgets. Journal of Geophysical Research. 112: 2156-2202

Holloway G and Sou T. 2002. Has Arctic sea ice rapidly thinned? Journal of Climate. 15: 1691-1701

Hood E, Williams M, Cline D. 1999. Sublimation from a seasonal snowpack at a continental, mid-latitude alpine site. Hydrological Processes. 13: 1781-1797

Iacozza J, Barber D. 2001. Ablation patterns of snow cover over smooth first-year sea ice in the Canadian Arctic. Hydrological Processes 15: 3559-3569

Jensen J. 2000. Remote Sensing of the Environment: An Earth Resource Perspective. Upper Saddle River, NJ: Prentice Hall.

Jiang J and Wu D. 2004. Ice and water permittivities for millimeter and sub millimeter remote sensing applications. Atmospheric Science Letters. 5: 146-151

Jin Y-Q. 1984. Wave approach to brightness temperature from a bounded layer of random discrete scatterers. Electromagnetics. 4(2-3): 323-341

Jonas T, Marty C, Magnusson J. 2009. Estimating the snow water equivalent from snow depth measurements in the Swiss Alps. Journal of Hydrology. 378: 161-167

Jordan R. 1991. A one-dimensional temperature model for a snow cover: Technical documentation for SNTHERM.89. U.S. Army Corps of Engineers.

Jordan R and Andreas E. 1999. Heat budget of snow-covered sea ice at North Pole 4. Journal of Geophysical Research. 104(C4): 7785-7806

Kaatsov V, Walsh J, Chapman W, Govorkova V, Pavlova T, Zhang X. 2007. Simulation and projection of Arctic freshwater budget components by the IPCC AR4 global climate models. Journal of Hydrometeorology. 8: 571-589

Kelly R, Chang A, Tsang L, Foster J. 2003. A prototype AMSR-E global snow area and snow depth algorithm. IEEE Transactions on Geoscience and Remote Sensing. 41(2): 230-242 doi:10.1109/TGRS.2003.809118

Kendra J, Sarabandi K, Ulaby F. 1998. Radar measurements of snow: Experiments and analysis. IEEE Transactions on Geoscience and Remote Sensing. 36: 864-879

Kiehl J and Trenberth K. 1997. Earth's annual global mean energy budget. Bulletin of the American Meteorological Association. 78: 197-208

Kim Y, Onsott R, Moore R. 1984. The effect of a snow cover on microwave backscatter from sea ice. IEEE Journal of Oceanic Engineering. 9: 383-388

Kohn J and Royer A. 2010. AMSER-E data inversion for soil temperature estimation under snow cover. Remote Sensing of Environment. 114: 2951-2961

Kohn V, Mokhov I, Roeckner E, Semenov V. 2007. Regional changes of precipitation characteristics in northern Eurasia from simulations with global climate model. Global and Planetary Change. 57: 118–123

Kontu A and Pulliainen J. 2010. Simulation of spaceborne microwave radiometer measurements of snow cover using in situ data and brightness temperature modeling. IEEE Transactions on Geoscience and Remote Sensing. 48(3): 1031-1044

Kurvonen L and Hallikainen M. 1997. Influence of land-cover category on brightness temperature of snow. IEEE Transactions on Geoscience and Remote Sensing. 35(2): 367-377 doi:10.1109/36.563276

Langlois A and Barber D. 2007. Passive microwave remote sensing of seasonal snow covered sea ice. Progress in Physical Geography. 31(6): 539-573

Langlois A, Barber D, Hwang B. 2007. Development of a winter snow water equivalent algorithm using in-situ passive microwave radiometry over snow covered first-year sea ice. Remote Sensing of Environment. 106(1): 75-88

Langlois A, Brucker L, Kohn J, Royer A, Derksen C, Cliche P, Picard G, Willamet J, Fily M. 2009. Simulation for snow water equivalent (SWE) using thermodynamic snow models in Quebec, Canada. Journal of Hydrometeorology. 10(6): 1447-1463

Langlois A, Mundy C, Barber D. 2007. On the winter evolution of snow thermophysical properties over landfast first-year sea ice. Hydrological Processes. 21: 705-716

Langlois A, Royer A, Monpetit B, Picard G, Brucker L, Arnaud L. 2010. On the relationship between snow grain morphology and in-situ near infrared calibrated reflectance photographs. Cold Regions Science and Technology. 61(1): 34-42 doi:10.1016/j.coldregions.2010.01.004

Lapo K, Hinkelman L, Raleigh M, Lundquist J. 2015. Impact of errors in the downwelling irradiances on simulations of snow water equivalent, snow surface temperature, and the snow energy balance. Water Resources Research. doi:10.1002/2014WR016259

Lecomte O, Fichefet T, Vancoppenolle M, Nicolaus M. 2011. A new snow thermodynamic scheme for large-scale sea-ice models. Annals of Glaciology. 52(57): 337-346

Ledley T. 1991. Snow on sea ice: competing effects in shaping climate. Journal of Geophysical Research. 96(D9): 17195-17208

Lemmetyinen J, Derksen C, Toose P, Proksch M, Pulliainen J, Kontu A, Rautiainen K, Seppanen J, Hallikainen, M. 2015. Simulating seasonally and spatially varying snow cover brightness temperature using HUT snow emission model and retrieval of a microwave effective grain size. Remote Sensing of Environment. 156: 71-95

Lemmetyinen J, Pulliainen J, Rees A, Kontu A, Qiu Y, Derksen C. 2010. Multiple-layer adaptation of HUT snow emission model: comparison with experimental data. IEEE Transactions on Geoscience and Remote Sensing. 48(7): 2781-2794 doi:10.1109/TGRS.2010.2041357

Leppanen L, Kontu A, Vehvilainen J, Lemmetyinen J, Pulliainen J. 2015. Comparison of traditional and optical grain-size field measurements with SNOWPACK simulations in a taiga snowpack. Journal of Glaciology. 61(225): 151-162 doi: 10.3189/2015JoG14J026

Levine I. 2001. Physical Chemistry (5th ed.). New York: McGraw-Hill.

Liang D, Xu X, Tsang L, Andreadis K, Josberger E. 2008. The effects of layers in dry snow on its passive microwave emissions using dense media radiative transfer theory based on the quasicrystalline approximation (QCA/DMRT). IEEE Transactions on Geoscience and Remote Sensing. 46(11): 3663-3671

Linor W. 1980. Permittivity and attenuation of wet snow between 4 and 12 GHz. Journal of Applied Physics. 51: 2188-2816

Makynen MP, Manninen AT, Simila MH, Karvonen JA, Hallikainen MT. 2002. Incidence angle dependence of the statistical properties of C-band HH-polarization backscattering signatures of the Baltic Sea ice. IEEE Transactions on Geoscience and Remote Sensing 40(12): 2593-2605

Makynen M, Hallikainen M. 2004. Investigation of C- and X-band backscattering signatures of Baltic Sea ice. International Journal of Remote Sensing 25(11): 2061–2086.

Marsh P. 1999. Snow cover formation and melt: recent advances and future prospects. Hydrological Processes. 13: 2119-2134

Marsh P and Woo M. 1984. Wetting front advance and freezing of meltwater within a snow cover 1. Observations in the Canadian Arctic. Water Resources Research. 20(12): 1853-1864 doi:10.1029/WR020i012p01853

Marshall S. 2011. The Cryosphere. Princeton, NJ, USA: Princeton University Press.

Marshall S and Warren S. 1987. Parameterization of snow albedo for climate models. Large Scale Effects of Snow cover Conference: Vancouver. 43-50. The International Association of Hydrological Sciences.

Martin S. 1979. A field study of brine drainage and oil entrainment in first-year sea ice. Journal of Glaciology. 22(88): 473-502

Matcalfe J and Goodison B. 1993. Correction of Canadian winter precipitation data. Eighth symposium on meteorological observations and instrumentations. 338-343. Anaheim, CA: American Meteorological Society.

Matzler C. 1987. Applications of the interactions of microwaves with the natural snow cover. Remote Sensing Reviews. 2(2): 259-387

Matzler C. 1994. Passive microwave signatures of landscapes in winter. Meteorology and Atmospheric Physics. 54(1-4): 241-160 doi:10.1007/BF01030063

Matzler C. 1996. Microwave permittivity of dry snow. IEEE Transactions on Geoscience and Remote Sensing. 34(2): 573-581

Matzler C. 1998. Improved Born approximation for scattering radiation in a granular medium. Journal of Applied Physics. 83(11): 6111-6117

Matzler C. 2002. Relation between grain-size and correlation length of snow. Journal of Glaciology. 48(162): 461-466

Matzler C and Wegmuller U. 1987. Dielectric properties of fresh-water ice at microwave frequencies. Journal of Physics D: Applied Physics. 20: 1623-1630

Matzler C and Wiesmann A. 1999. Extension of the microwave emission model of layered snowpacks to coarse grained snow. Remote Sensing of Environment. 70(3): 317-325 doi: 10.1016/S0034-4257(99)00047-4

Maykut G. 1982. Large-scale heat exchange and ice production in the Central Arctic. Journal of Geophysical Research. 87(C10): 7971-7984

Maykut G. 1986. The Surface Heat and Mass Balance. In N. Untersteiner, The Geophysics of Sea Ice (Vol. Series B: Physics Volume 146, pp. 395 - 464). NY, NY, USA: Plenum Press.

Maykut G and Untersteiner N. 1971. Some results from a time-dependent thermodynamic model of sea ice. Journal of Geophysical Research. 76(6): 1550-1575

Mellor M. 1977. Engineering properties of snow. Journal of Glaciology. 19: 15-66

Mesinger F, DiMego G, Kalnay E, Mitchel K, Shafran P, Ebisuzaki W, Jovic D, Wollen J, Rogers E, Berbery E, Ek M, Fan Y, Grumbine R, Higgins W, Li H, Lin Y, Mankin G, Parrish D, Shi W. 2006. North American Regional Reanalysis. Bulletin of the American Meteorological Society. 87(3): 343-360

Monpetit B, Royer A, Langlois A, Cliche P, Roy A, Champollion N, Picard G, Domine F, Obbard R. 2012. New short wave infrared albedo measurements for specific surface area retrieval. Journal of Glaciology. 58(211): 941-952

Montpetit, B., Royer, A., Langlois, A., Derksen, C. 2013. Snow microwave emission modeling of ice lenses within a snowpack using the Microwave Emission Model for Layered Snowpacks. IEEE Transactions on Geoscience and Remote Sensing, 51(9), 4705-4717.

Moorman B. 2001. Ground-penetrating radar applications in paleolimnology. In W. M. Last, and J. P. Smol (Eds.), Tracking Environmental Change Using Lake Sediments: Physical and Chemical Techniques (pp. 23-47). Boston, MA: Kluwer Academic Publishers.

Musil J and Zacek F. 1986. Microwave Measurements of Complex Permittivity by Free Space Methods and their Applications. NY, NY: Elsevier.

Nakawo M and Sinha N. 1981. Growth rate and salinity profile of first-year sea ice in the high Arctic. Journal of Glaciology. 27: 315-330

Nghiem S, Kwok R, Yueh S, Drinkwater M. 1995a. Polarimetric signatures of sea ice 1. Theoretical model. Journal of Geophysical Research 100(C7): 13665-13679

Nghiem S, Kwok R, Yueh S, Drinkwater M. 1995b. Polarimetric signatures of sea ice 2. Experimental observations. Journal of Geophysical Research 100(C7): 13681-13698

Nolen A and Liang S. 2000. Progress in bidirectional reflectance modeling and applications for surface particulate. Remote Sensing Review. 18: 307-342

Oke T. 1987. Boundary Layer Climates (2nd. ed.). Cambridge, UK: Routledge.

Ono, N., 1968. Thermal properties of sea ice. IV. Thermal constants of sea ice. Low Temperature Science, A26:329-349.

Overland J and Wang M. 2010. Large-scale atmospheric circulation changes are associated with the recent loss of Arctic sea ice. Tellus: Series A: Dynamic Meteorology and Oceanography. 62: 1-9

Park H, Fedorov A, Zheleznyak M, Konstantinov P, Walsh J. 2015. Effect of snow cover on pan-Arctic permafrost thermal regimes. Climate Dynamics. 44: 2873-2895

Parkinson C and Washington W. 1979. A large scale numerical model of sea ice. Journal of Geophysical Research. 84: 311-337

Peixoto J and Oort A. 1992. Physics of Climate. New York, USA: Springer-Verlag New York, Inc.

Perovich D and Polashenski C. 2012. Albedo evolution of seasonal Arctic sea ice. Geophysical Research Letters. 39: L08501

Pivot F, Kergomard C, Duguay C. 2002. Use of passive-microwave data to monitor spatial and temporal variations of snow cover at tree line near Churchill, Manitoba, Canada. Annals of Glaciology. 34(1): 58-64 doi:10.3189/172756402781817590

Pulliainen, J. 2006. Mapping of snow water equivalent and snow depth in boreal and sub-arctic zones by assimilating space-borne microwave radiometer data and ground-based observations. Remote Sensing of Environment. 101(2): 257-269 doi:10.1016/j.rse.2006.01.002

Pulliainen, J, Grandell J, Hallikainen M. 1999. HUT snow emission model and its applicability to snow water equivalent retrieval. IEEE Transactions on Geoscience and Remote Sensing. 37(3): 1378-1390

Pulliainen J and Hallikainen M. 1998. Estimation of snow water equivalent from SSM/I data by using a physical model-based inversion algorithm. IGARSS. 1541-1543. Seattle, WA: IEEE International.

Pullianinen J and Hallikainen M. 2001. Retrieval of regional snow water equivalent from space-borne passive microwave observations. Remote Sensing of Environment. 75: 76-85

Rawlins M, Steele M, Holland M, Adam J, Cherry J, Francis J, Groisman P, Hinzman L, Huntington T, Kane D, Kimball J, Kwok R, Lammers R, Lee C, Lettenmaier D, McDonald K, Podest E, Wensnahan M, Wood E, Woodgate R, Yang D, Zhang K, Zhang T. 2010. Analysis of the Arctic system for freshwater cycle intensification: Observation and expectation. Journal of Climate. 23(21): 5715-5737

Rees W. 2006. Remote Sensing of Snow and Ice. Cambridge Press/Taylor and Francis Group.

Rees A, Lemmetyinen J, Derksen C, Pulliainen J, English M. 2010. Observed and modeled effects of ice lens formation on passive microwave brightness temperature over snow covered tundra. Remote Sensing of Environment. 114: 116-126

Robinson D, Serreze M, Barry R, Scharfen G, Kukla G. 1992. Large-scale patterns and variability of snowmelt and parameterized surface albedo in the Arctic Basin. Journal of Climate. 5: 1109-1119

Robok A. 1983. Ice and snow feedbacks and the latitudinal and seasonal distribution of climate sensitivity Journal of Atmospheric Science. 40(4): 986-997 doi:10.1175/1520-0469(1983)040<0986:IASFAT>2.0.CO;2

Rosenfeld, S., and Grody, N. (2000). Metamorphic signature of snow revealed in SSM/I measurements. IEEE Transactions on Geoscience and Remote Sensing, 38, 53–63

Roy V, Goita K., Royer A, Walker A, Goodison B. 2004. Snow water equivalent retrieval in a Canadian boreal environment from microwave measurements using the HUT snow emission model. IEEE Transactions on Geoscience and Remote Sensing. 42(9): 1850-1859

Rutter N, Sandells M, Derksen C, Toose P, Royer A, Montpetit, B, Langlois A, Lemmetyinen J, Pulliainen, J. 2014. Snow stratigraphic heterogeneity within ground-based passive microwave radiometer footprints: Implications for emission modeling. Journal of Geophysical Research: Earth Surface. 119: 550-565 doi:10.1002/2013JF003017

Schanda E, Matzler C, Kunzi K. 1983. Microwave remote sensing of snow cover International Journal of Remote Sensing. 4(1): 149-158

Scharien R. 2004. Analysis of surface roughness and morphology of first-year sea ice melt ponds: Implications for microwave scattering. M.Sc.Thesis. Calgary, Alberta, Canada: University of Calgary, Department of Geography.

Scharien R, Geldsetzer T, Barber D, Yackel J, Langlois A. 2010. Physical, dielectric, and C-band microwave scattering properties of first-year sea ice during advanced melt. Journal of Geophysical Research: Oceans. 115(C12): C12026

Schneebeli M and Sokratov S. 2004. Tomography of temperature gradient in metamorphism of snow and associated changes in heat conductivity. Hydrological Processes. 18: 3655-3665

Schwerdtfeger, P. 1963. The thermal properties of sea ice. Journal of Glaciology. 789-807

Shea J, Anslow F, Marshall S. 2005. Hydrometeorological relationships on Haig Glacier, Alberta, Canada. Annals of Glaciology. 40(1): 52-60

Serreze M and Barry R. 2005. The Arctic climate system. Cambridge, UK: Cambridge University Press.

Serreze M and Francis J. 2006. The Arctic amplification debate. Climatic Change. 76: 241-264

Sing V. 1992. Elementary Hydrology. Upper Saddle River, New Jersey, U.S.A.: Prentice Hall, Inc.

Spiridonov V. 1982. A relaxation model for the dielectric properties of water in heterogeneous mixtures. Measurement Techniques. 25(5): 448-451

Stiles W and Ulaby F. 1981. Dielectric properties of snow. Lawrence, Kansas: The University of Kansas Center for Research, Inc.

Sturm M, Holmgren J, Konig M, Morris K. 1997. The thermal conductivity of seasonal snow. Journal of Glaciology. 43(143): 26-41

Sturm M, Holmgren J, Perovich D. 2002. Winter snow cover on the sea ice of the Arctic Ocean at the Surface Heat Budget of the Arctic Ocean (SHEBA): temporal evolution and spatial variability. Journal of Geophysical Research. 107(C10): SHE 23-1 - 23-17

Sturm M, Maslanik J, Perovich D, Sroeve J, Richter-Menge J, Markus T, Holmgren J, Heinrichs J, Tape K. 2006. Snow depth and ice thickness measurements from the Beaufort and Chukchi Seas collected during the AMSR-Ice03 campaign. IEEE Transactions on Geoscience and Remote Sensing. 44(11): 3009-3019

Sun C, Walker J, Houser P. 2004. A simple snow-atmosphere-soil transfer model. Journal of Geophysical Research. 104: 19587-19594

Takala M., Luojus K, Pulliainen J, Derksen C, Lemmetyinen J, Karna J, Koskinen J, Bojkov B. 2011. Estimating northern hemisphere snow water equivalent for climate research through assimilation of space-borne radiometer data and ground-based measurements. Remote Sensing of Environment. 115(12): 3517-3529

Tedesco M and Kim E. 2006. Intercomparison of electromagnetic models for passive microwave remote sensing of snow. IEEE Transactions on Geoscience and Remote Sensing. 44(10): 2654-2666

Tiuri M and Shivola A. 1986. Snow for field determination of the density and wetness profiles of a snowpack. Hydrologic Application of Space Technology. 160: 225-230. Cocoa Beach, FL: IAHS.

Tiuri M, Sihvola A, Nyfors E, Hallikainen M. 1984. The complex dielectric constant of snow at microwave frequencies. IEEE Journal of Oceanic Engineering. OE-9(5): 377-382

Toure A, Goita K, Royer A, Kim E, Durand M, Margulis S, Lu H. 2011. A case study of using a multilayered thermodynamical snow model for radiance assimilation. IEEE Transactions on Geoscience and Remote Sensing. 49(8): 2828-2837

Trenberth K, Jones P, Ambenje P, Bojariu R, Easterling D, Klein A, Tank D, Parker D, Renwick J, Rahimzadeh F, Rusticucci M, Soden B, Zhai P, 2007: Observations: Surface and

Atmospheric Climate Change. In: Climate Change 2007: The Physical Science Basis. Contribution of Working Group I to the Fourth Assessment Report of the Intergovernmental Panel on Climate Change [Solomon S, Qin D, Manning M, Chen Z, Marquis M, Averyt K, Tignor M, Miller H (eds.)]. Cambridge University Press, Cambridge, United Kingdom and New York, NY, USA.

Trevett J. 1986. Imaging Radar for Resource Surveys. NY, NY: Chapman and Hall.

Tsang L. 1987. Passive remote sensing of dense nontenuous media. Journal of Electromagnetic Waves and Applications, 1(2), 159-173.

Tsang L, Chen C, Chang A, Guo J, Ding K. 2000. Dense media radiative transfer theory based on quasicrystalline approximation with applications to passive microwave remote sensing. Radio Science. 35(3): 731-749

Tsang L, Kong J, Shin R. 1985. Theory of microwave remote sensing. New York, NY: Wiley.

Ulaby F, Moore R, Fung A. 1981. Microwave Remote Sensing: Active and Passive (Vol. I: Microwave Remote Sensing Fundamentals and Radiometry). Norwood, MA: Artech House.

Ulaby F, Moore R, Fung A. 1982. Microwave Remote Sensing: Active and Passive (Vol. II: Radar Remote Sensing and Surface Scattering and Emission Theory). Norwood, MA: Artech House.

Ulaby F, Moore R, Fung A. 1986. Microwave Remote Sensing: Active and Passive (Vol. III: From Theory to Applications). Norwood, MA: Artech House.

Ulaby F, Stiles W. 1980. The active and passive microwave response to snow parameters 2. water equivalent of dry snow. Journal of Geophysical Research. 85(C2): 1045-1049

Ulaby F, Stiles W, Abdelrazik M. 1984. Snow cover influence on backscattering from terrain. IEEE Transactions on Geoscience and Remote Sensing. GE-22(2): 126-133

Wadhams P. 2000. Ice in the ocean. Amsterdam, The Netherlands: Gordon and Breach Science Publishers.

Wakahama G. 1968. The metamorphism of wet snow. International Association of Hydrological Sciences. 79: 370-379

Warner K, Iacozza J, Scharien R, Barber D. 2013. On the classification of melt season first-year and multi-year sea ice in the Beaufort Sea using Radarsat-2 data. International Journal of Remote Sensing. 34(11): 3760-3744

Warren S, Rigor I, Untersteiner N, Radionov V, Bryazgin N, Aleksandrov Y. 1999. Snow depth on Arctic Sea ice. Journal of Climate. 12: 1814-1829

Weeks W, Ackley S. 1986. The growth, structure and properties of sea ice. The Geophysics of Sea Ice, edited by N. Untersteiner, pp. 9-164, NATO ASI Series B: Physics vol. 146, Plenum Press, New York.

Wen B, Tsang L, Winebrenner D, Ishimaru A. 1990. Dense medium radiative transfer theory: Comparison with experiment and application to microwave remote sensing and polarimetry. IEEE Transactions on Geoscience and Remote Sensing. 28(1): 46-59

Willmes S, Nicolaus M, Haas C. 2014. The microwave emissivity variability of snow covered first-year sea ice from late winter to early summer: a model study. The Cryosphere. 8: 891-904

Winebrenner D, Bredow J, Fung A, Drinkwater M, Nghiem S, Gow A, Perovich D, Grenfell T, Han H, Kong J, Lee J, Mudaliar S, Onstott R, Tsang L, West, R. 1992. Microwave sea ice signature modeling. In F. Carsey (Ed.), Microwave Remote Sensing of Sea Ice (Vol. Geophysical Monograph Series, pp. 137 - 171). Washington, D.C.: AGU.

Wiscombe W and Warren S. 1980. A Model for Spectral Albedo of Snow. I: Pure Snow. Journal of Atmospheric Science. 37(12): 2712-2733

Wiesmann A, Fierz C, Matzler C. 2000. Simulation of microwave emission from physically modeled snowpacks. Annals of Glaciology. 31: 397-405

Wiesmann A and Matzler C. 1999. Microwave emission model of layered snowpacks. Remote Sensing of Environment. 70(3): 307-316 doi:10.1016/S0034-4257(99)00046-2

Wiesmann A, Matzler C, Weise T. 1998. Radiometric and structural measurements of snow samples. Radio Science. 33(2): 273-289

Woodhouse I. 2006. Introduction to Microwave Remote Sensing. Boca Raton, FL: CRC Press, Taylor and Francis Group.

Yackel J and Barber D. 2007. Observations of snow water equivalent change on landfast first-year sea ice using synthetic aperture radar data. IEEE Transactions on Geoscience and Remote Sensing. 45(4): 1005-1015

Zhang T, Stamnes K, Bowling S. 1996. Impact of clouds on surface radiative fluxes and snowmelt in the Arctic and Subarctic. Journal of Climate. 9: 2110-2123

Web

Canadian Ice Service Website. Retrieved 05 15, 2015 www.ec.gc.ca

Chaplin M. 2011 (July 26). Water Structure and Science. Retrieved 11 26, 2011, from Water and Microwaves: http://www.lsbu.ac.uk/water/microwave.html

Integra. (2010). Volume Scattering Definition. Retrieved 11 26, 2011, from Integra: http://www.integra.jp/en/specter/features/volume_scattering/index.html

GlobSnow. Retrieved 11 26, 2011, from Finnish Meteorological Institute: http://www.globsnow.info/

Nezlin N. (2004, 4 28). Oceanographic Applications: Radar Altimeters. Retrieved 03 17, 2008, from University of California, Los Angeles - Department of Ecology and Evolutionary Biology: http://www.eeb.ucla.edu/test/faculty/nezlin/Altimetry.htm

SNTHERM Website. (S. B. University of California, Producer) Retrieved 03 15, 2015, from Institute for Computational Earth System Science: http://www.icess.ucsb.edu/~mtc/sntherm_docs/sntherm.html

Appendix A: Contributions

Chapter 1, 2, and 6: Dr. John Yackel*, Dr. Chris Derksen (Univeristy of Waterloo and Environment Canada), Dr. Torsten Geldsetzer* provided important advice and review of these chapters.

Chapter 3: Dr. John Yackel, Dr. Chris Derksen, Dr. Torsten Geldsetzer, and Dr. JV Gill* provided important advice and review. Dr. Geldsetzer provided the MSIB Backscattering Program, and processed the RADARSAT-2 images and data for comparison.

Chapter 4: Dr. Yackel, Dr. Derksen, and Dr. Geldsetzer provided important advice and review. Dr. Derksen provided the multiple-layer HUT model, contributed to geophysical and emission data collection, and provided calibrated radiometer emission data. Dr. Alex Langlois (University of Sherbrooke) provided IRIS and 3D data, and drove that data collection while I assisted.

Chapter 5: Dr. Yackel, Dr. Derksen, Dr. Geldsetzer, and Dr. Gill* provided important advice and review. Dr. Geldsetzer provided the MSIB Backscattering Program. Dr. Gill set up the SNTHERM program on local servers, and provided valuable advice in SNTHERM operation with stock training data sets. Jean-Benoit Madore (University of Sherbrooke) provided the NARR data, and Alex Beaudoin aided in the linear interpolation of the 3 hour NARR data to 1 hour data.

*Dr. Yackel, Dr. Geldsetzer, Dr. Gill are from the University of Calgary Cryosphere Climate Research Group.